

Effective Models of Beyond the Standard Model Scalars Coupled to Vector-like Fermions and their Phenomenology

By

Tuhin Subhra Mukherjee

PHYS10201004004

The Institute of Mathematical Sciences, Chennai

A thesis submitted to the

Board of Studies in Physical Sciences

In partial fulfillment of requirements

For the Degree of

DOCTOR OF PHILOSOPHY

of

HOMI BHABHA NATIONAL INSTITUTE



September, 2017

Homi Bhabha National Institute

Recommendations of the Viva Voce Committee

As members of the Viva Voce Committee, we certify that we have read the dissertation prepared by Tuhin Subhra Mukherjee entitled "Effective Models of Beyond the Standard Model Scalars Coupled to Vector-like Fermions and their Phenomenology" and recommend that it may be accepted as fulfilling the thesis requirement for the award of Degree of Doctor of Philosophy.

Chairman – Prof. Rahul Sinha

Date:

Guide / Convener – Prof. Shrihari Gopalakrishna

Date:

Examiner – Prof. Partha Konar

Date:

Member 1- Prof. Nita Sinha

Date:

Member 2- Prof. V. Ravindran

Date:

Final approval and acceptance of this thesis is contingent upon the candidate's submission of the final copies of the thesis to HBNI.

I hereby certify that I have read this thesis prepared under my direction and recommend that it may be accepted as fulfilling the thesis requirement.

Date:

Place:

Prof. Shrihari Gopalakrishna
(Guide)

STATEMENT BY AUTHOR

This dissertation has been submitted in partial fulfillment of requirements for an advanced degree at Homi Bhabha National Institute (HBNI) and is deposited in the Library to be made available to borrowers under rules of the HBNI.

Brief quotations from this dissertation are allowable without special permission, provided that accurate acknowledgment of source is made. Requests for permission for extended quotation from or reproduction of this manuscript in whole or in part may be granted by the Competent Authority of HBNI when in his or her judgment the proposed use of the material is in the interests of scholarship. In all other instances, however, permission must be obtained from the author.

Tuhin Subhra Mukherjee

DECLARATION

I, hereby declare that the investigation presented in the thesis has been carried out by me. The work is original and has not been submitted earlier as a whole or in part for a degree / diploma at this or any other Institution / University.

Tuhin Subhra Mukherjee

List of Publications arising from the thesis

The thesis is based on the papers marked by stars (*).

- **Published**

1. *Shrihari Gopalakrishna, Tuhin Subhra Mukherjee, Soumya Sadhukhan, "Extra Neutral scalars with Vector-like fermions at the LHC", Phys.Rev. D93 (2016) no.5, 055004, arXiv:1504.01074 [hep-ph].
2. Shrihari Gopalakrishna, Tuhin Subhra Mukherjee, Soumya Sadhukhan, "Status and Prospects of the Two-Higgs-Doublet SU(6)/Sp(6) little-Higgs Model and the Alignment Limit", Phys.Rev. D94 (2016) no.1, 015034, arXiv:1512.05731.

- **Conference proceedings**

1. Kaustubh Agashe et al, "Warped Extra Dimensional Benchmarks for Snowmass 2013", C13-07-29.2 Proceedings, arXiv:1309.7847 [hep-ph].

- **On arXiv**

1. *Shrihari Gopalakrishna, Tuhin Subhra Mukherjee, "The 750 GeV diphoton excess in a two Higgs doublet model and a singlet scalar model, with vector-like fermions, unitarity constraints, and dark matter implications", arXiv:1604.05774 .

Tuhin Subhra Mukherjee

ACKNOWLEDGMENTS

First of all I would like to thank my supervisor Shrihari Gopalakrishna for his constant supervision and inspiration. Without his efforts this thesis would not have been possible. I would like to thank my parents for their constant encouragements. I would like to thank Soumya for his efforts in the works we have done together. I would like to thank all of my friends in IMSc for making my stay in IMSc enjoyable.

Contents

Synopsis	xi
List of Figures	xv
List of Tables	xvii
1 Introduction	1
1.1 The Standard Model	1
1.1.1 The Higgs mechanism	3
1.1.2 The Higgs boson	6
1.2 Drawbacks of the standard model	7
2 Beyond the Standard Model	13
2.1 Extended scalar sector	13
2.2 Supersymmetry	14
2.3 Extra-dimensional models:	16
2.3.1 Flat extra dimension	16
2.3.2 Warped extra dimension	17
2.4 Little-Higgs models:	19
2.5 Strongly coupled theories	21
2.6 Vector-like fermions	22
3 Model independent analysis of BSM neutral scalars	25
3.1 8 TeV LHC constraints and 14 TeV LHC cross section	27

4	Phenomenology of a singlet CP-odd scalar model with vector-like fermions	32
4.1	SVU model	32
4.2	SVQ model	35
5	Two Higgs doublet Model type-I, II, X	36
5.1	The Yukawa couplings	41
6	Phenomenology of neutral scalars in Two Higgs doublet model with vector-like fermions	45
6.1	2HDM with SMF only	46
6.1.1	2HDM-II	47
6.1.2	2HDM type-X	49
6.2	2HDM with vectorlike fermions	50
6.2.1	2HDM with VLQ-SM Yukawa coupling	51
6.2.2	2HDM-II with VLQ-VLQ Yukawa coupling	58
6.3	2HDM-X with VLQ-VLQ Yukawa coupling	67
6.4	2HDM-II with VLL-VLL Yukawa couplings	70
7	Diphoton rates in 2HDM and a singlet scalar model	73
7.1	Model Independent analysis	74
7.1.1	13 TeV LHC $\sigma(gg \rightarrow \gamma\gamma)$	74
7.1.2	8 TeV LHC constraints	76
7.1.3	Unitarity constraints	77
7.2	Diphoton rates in the 2HDM and a singlet scalar model	79
7.2.1	Two Higgs doublet model	79
7.2.2	Singlet scalar model	88
7.3	750 GeV diphoton excess	94
8	WIMP dark Matter	100
8.1	Relic density	100
8.2	Dark matter direct detection	103

9	Singlet scalar model and dark matter	105
9.1	Relic density	105
9.2	Dark matter direct detection cross section	108
10	Summary and conclusions	112
A	The effective ϕgg and $\phi\gamma\gamma$ couplings	117
B	Effective couplings in SVU and MVU models	120

Synopsis

After the discovery of the Higgs boson at the LHC, the standard model (SM) is put on firm ground. Despite its experimental verifications some theoretical issues such as the gauge-hierarchy problem, flavor hierarchy problem etc. still remain unanswered in the SM. Moreover the SM can not explain the observed dark matter, neutrino mass and the baryon asymmetry of the universe. These considerations naturally calls for some new physics beyond the SM (BSM). Recently, quite unexpectedly, both ATLAS and CMS have reported an excess in the diphoton channel at around 750 GeV [1, 2]. If this excess persists in the future run of the LHC, this will be a clear signal for some new physics at the TeV scale.

Over the years many BSM theories have been proposed. Some of these, for example, composite Higgs models, little-Higgs models and some extra-dimensional models predict that the standard model (SM) Higgs is a pseudo goldstone boson (pNGB) of some spontaneously broken approximate global symmetry. In some of these models, the SM Higgs is accompanied by other extra neutral scalars (collectively called ϕ), either CP-even (H) or CP-odd (A). These extra scalars can be SU(2) singlets or can come as a part of an SU(2) scalar doublet. Some of these models have a two-Higgs doublet model (2HDM) structure [3, 4, 5]. To make the theory invariant under the bigger symmetry group, the SM fermions have vector like fermion (VLF) partners that together complete the group multiplet. The main focus of the thesis will be to study the phenomenology of BSM neutral scalars with VLFs also present. We also touch upon briefly its possible dark matter implications.

The outline of the thesis is as follows. In the introductory chapter we give a brief review of the standard model of particle physics, discuss the drawbacks of the SM and the motivations for going beyond the SM. In the next chapter we perform a model independent

analysis of a general scalar ϕ , either scalar or pseudoscalar, with Yukawa couplings to the SM fermions. The interactions of the ϕ with the gauge bosons $gg, \gamma\gamma, Z\gamma, ZZ, WW$ (collectively called VV) are incorporated by effective five dimensional operators. In a specific model these operators will be generated by heavy particles in the loop. We focus on such a scalar produced by the $gg \rightarrow \phi$ process as this is usually the dominant process. We present the 8 TeV and 14 TeV LHC $\sigma(gg \rightarrow \phi)$ cross section as a function of effective ϕgg coupling ($\kappa_{\phi gg}$). Using this, we obtain constraints on $BR(\phi \rightarrow tt, \tau\tau, \gamma\gamma)$ and $\kappa_{\phi gg}$, from the 8 TeV LHC $tt, \tau\tau, \gamma\gamma$ channel results [6, 7, 8]. These results are detailed in Ref. [9].

In the next chapter we consider two models with an SU(2) singlet pseudoscalar (A) coupled to either an SU(2) singlet or a doublet VLQ. We present the effective $A gg$ coupling and $BR(A \rightarrow \gamma\gamma, Z\gamma, ZZ)$ for each of these models. For the doublet VLQ case we additionally present $BR(A \rightarrow WW)$. For $M_A < m_h/2$, we present $BR(h \rightarrow AA)$ also and the $h \rightarrow \gamma\gamma$ signal strength. These results are detailed in Ref. [9].

In the next chapter we briefly discuss the two-Higgs doublet models (2HDM) which will be relevant in the subsequent chapters. The 2HDM contains two scalar $SU(2)$ doublets Φ_1 and Φ_2 . We choose a 2HDM potential such that electroweak symmetry is broken via expectation values of Φ_1 and Φ_2 . We have five physical states, two neutral CP-even scalars h, H , a neutral CP-odd scalar A and the charged scalars H^\pm . The lightest scalar h is identified as the SM Higgs. We will specialize to the so called “2HDM alignment limit” in which the Yukawa couplings and the gauge couplings of the h become identical to those of the SM Higgs. Different kinds of Yukawa structures have been proposed and we consider those that are safe from tree level flavor changing neutral currents. The usual types of couplings well known in the literature that we study here are the so called 2HDM type-II, type-X and type-I which we denote as 2HDM-II, 2HDM-X and 2HDM-I.

In the next chapter we discuss the phenomenology of 2HDM-II and 2HDM-X with SM fermions only, and few models with VLFs also introduced. In the loop level $\phi \rightarrow VV$ processes, these VLFs will interfere either constructively or destructively with the SM fermions in the loop thereby modifying both $\sigma(gg \rightarrow \phi)$ and $BR(\phi \rightarrow VV)$. We separately consider two kinds of models, one in which the VLFs mix with the SM third generation quarks and

one in which these mixings are shut off. We present the $\kappa_{\phi gg}$ for each each of these models. For the model where the VLF mix with the SM top quark, we analyze the deviation of the top Yukawa coupling from its SM value. We present $\text{BR}(\phi \rightarrow tt, bb, gg, t_2t, b_2b)$, where t_2, b_2 are EM charge $2/3$ and $-1/3$ heavy VLQ states present in these models. For the models where VLFs and SM quarks do not mix, we present $\text{BR}(\phi \rightarrow tt, bb, \tau\tau, Z\gamma, \gamma\gamma)$. We find that in some regions of parameter space the VLFs can modify $\kappa_{\phi gg}$ and $\text{BR}(\phi \rightarrow VV)$ significantly compared to the 2HDM with SM fermions only. We also find that in one of these models, the addition of VLFs can open up regions of parameter space which are excluded in 2HDM with SM fermions only. These results are detailed in Ref. [9]. As pointed out in the introduction, there are many UV complete models that have a 2HDM structure and VLFs. The phenomenology of one such model namely the $SU(6)/Sp(6)$ little-Higgs model [5] has been studied in Ref. [10].

In the next chapter we give a brief review of dark matter which will be relevant in later chapters. We give the details of the relic density and dark matter direct detection cross section (σ_{DD}) and discuss the constraints coming from dark matter experiments. In the next chapter we present few models explaining the recent diphoton excess at the LHC at 750 GeV [1, 2]. We assume that the resonance is a scalar and produced through the gluon fusion process. We consider a general scalar ϕ coupled to the SM fermions and VLFs (collectively called ψ). We present the values of effective ϕgg and $\phi\gamma\gamma$ couplings required to explain the excess for various ϕ widths. We present a model independent analysis of the constraints coming from the 8 TeV LHC $tt, \tau\tau, hh$ results [6, 7, 11]. We determine the constraints on the $\phi\psi\psi$ Yukawa couplings from the perturbative unitarity of $\phi\phi \rightarrow \phi\phi$ and $\psi\psi \rightarrow \psi\psi$ processes. These results are detailed in Ref. [12]. We consider few specific models where ϕ is either a 2HDM scalar or an $SU(2)$ singlet. We analyze the 2HDM-II with SM fermions only and few models where we add VLLs and/or VLQs to 2HDM of type-II, X and I. We analyze a model where a singlet scalar is coupled to an $SU(2)$ singlet VLQ, an $SU(2)$ singlet VLL and the SM Higgs. For each of these models we present the $\sigma(\phi) * \text{BR}(\gamma\gamma)$. For the singlet scalar model, if the VLL has zero hypercharge, it cannot decay to any SM particles and can be a dark matter candidate. In the next chapter we investigate this scenario. The important dark matter self annihilation

channels are $\psi\psi \rightarrow tt, WW, ZZ, hh, gg$ through ϕ and h exchange. We present the values the model parameters should take for obtaining the correct relic density. We present the constraints on the parameter space from the dark matter direct detection experiments. We find that there are regions of parameter space that is consistent with the experimental bound on σ_{DD} . There are also some regions of parameter space for which direct detection is possible in the near future. These results are detailed in Ref. [12]. In the last chapter we summarize the thesis and offer our conclusions.

List of Figures

1.2.1 Higgs mass corrections	8
3.1.1 $\sigma(gg \rightarrow \phi)$ in the 8 TeV and 14 TeV LHC	29
3.1.2 8 TeV LHC constraints from $\gamma\gamma, \tau\tau, tt$ channels	29
3.1.3 14 TeV LHC $\sigma(gg \rightarrow \phi)$ and 8 TeV LHC constraints from $\gamma\gamma, \tau\tau, tt$ channels	30
4.1.1 $\text{BR}(A \rightarrow VV)$ in the SVU model	33
4.1.2 $\kappa_{A_{gg}}$ in the $SVU\psi$ model	34
4.1.3 $\mu_{\gamma\gamma}$ in SVU model	34
6.1.1 $\text{BR}(A)$ in 2HDM-II	48
6.1.2 $\kappa_{A_{gg}}$ in 2HDM-II	48
6.1.3 Constraint on $m_A - \tan\beta$ plane in 2HDM-II	49
6.1.4 $\text{BR}(A)$ in 2HDM-X	49
6.1.5 $\kappa_{\phi_{gg}}$ in 2HDM-X	50
6.2.1 κ_{htt} in MVU model	53
6.2.2 $\kappa_{A_{gg}}$ in MVU model	54
6.2.3 $\text{BR}(A)$ in MVU model	54
6.2.4 $\kappa_{A_{gg}}$ in MVD model	56
6.2.5 $\text{BR}(A \rightarrow VV)$ in $MVQD_{11}$ model	61
6.2.6 $\kappa_{\phi_{gg}}$ in $MVQD_{11}$ model	62
6.2.7 $\kappa_{A_{gg}}$ vs. $\tan\beta$ in $MVQD_{11}$ model	63
6.2.8 $\kappa_{\phi_{gg}}$ in $MVQU_{22}$ model	64
6.2.9 $\text{BR}(A \rightarrow VV)$ in $MVQU_{12}$ model	67

6.2.10 $\kappa_{\phi gg}$ in $MVQU_{12}$ model	68
6.2.11 $\kappa_{A_{gg}}$ vs. $\tan\beta$ in $MVQU_{12}$ model	68
6.2.12 Constraint on $m_A - \tan\beta$ in $MVQU_{12}$ model	69
6.3.1 $\text{BR}(A \rightarrow \gamma\gamma, Z\gamma)$ in $MVQDX_{11}$ model	70
6.3.2 $\kappa_{\phi gg}$ in $MVQDX_{11}$ model	71
6.3.3 $\kappa_{A_{gg}}$ vs. $\tan\beta$ in $MVQD_{11}$ model	71
6.4.1 $\text{BR}(A \rightarrow \gamma\gamma)$ in $MVLE_{11}$ model	72
7.1.1 13 TeV LHC $\sigma(gg \rightarrow \phi \rightarrow \gamma\gamma)$ with M_ϕ	75
7.1.2 13 TeV LHC $\sigma(gg \rightarrow \phi \rightarrow \gamma\gamma)$ vs. $\kappa_{\phi gg}$	75
7.1.3 Feynman diagrams contributing to $\psi\psi \rightarrow \psi\psi$ and $\phi\phi \rightarrow \phi\phi$ processes.	77
7.1.4 Feynman diagram for the $\psi\psi \rightarrow \phi\phi$ process.	79
7.2.1 13 TeV LHC $\sigma(gg \rightarrow \phi \rightarrow \gamma\gamma)$ vs. κ_{Γ}^2 in 2HDM-II + SMF	81
7.2.2 13 TeV LHC $\sigma(gg \rightarrow \phi \rightarrow \gamma\gamma)$ in the 2HDM-II+VLL model	82
7.2.3 13 TeV LHC $\sigma(gg \rightarrow \phi \rightarrow \gamma\gamma)$ in the 2HDM-II + VLL+ VLQ model	83
7.2.4 13 TeV LHC $\sigma(gg \rightarrow \phi \rightarrow \gamma\gamma)$ in the 2HDM-II +VLL+VLQ model	84
7.2.5 13 TeV LHC $\sigma(gg \rightarrow \phi \rightarrow \gamma\gamma)$ in the 2HDM-II +VLL+VLQ model	85
7.2.6 13 TeV LHC $\sigma(gg \rightarrow \phi \rightarrow \gamma\gamma)$ in the 2HDM-X +VLL+VLQ model	86
7.2.7 13 TeV LHC $\sigma(gg \rightarrow \phi \rightarrow \gamma\gamma)$	86
7.2.8 13 TeV LHC $\sigma(gg \rightarrow \phi \rightarrow \gamma\gamma)$ in the 2HDM-X +VLL+VLQ model in the $M_\phi - y_U$ plane.	87
7.2.9 13 TeV LHC $\sigma(gg \rightarrow \phi \rightarrow \gamma\gamma)$ in 2HDM-I +VLL model	88
7.2.10 13 TeV LHC $\sigma(gg \rightarrow \phi \rightarrow \gamma\gamma)$ in the 2HDM-I + VLL +VLQ model	89
7.2.11 13 TeV LHC $\sigma(gg \rightarrow \phi \rightarrow \gamma\gamma)$ in the 2HDM-I +VLL+VLQ model in the $M_\phi - y_U$ plane.	89
7.2.12 13 TeV LHC $\sigma(gg \rightarrow \phi \rightarrow \gamma\gamma)$ vs. κ_{γ}^2 for the $SVU\psi$ model	92
7.2.13 13 TeV LHC $\sigma(gg \rightarrow \phi \rightarrow \gamma\gamma)$ as functions of model parameters in the $SVU\psi$ model	93
7.2.14 13 TeV LHC $\sigma(gg \rightarrow \phi \rightarrow \gamma\gamma)$ in the $M_\phi - y_U$ plane for the SVU_ψ model	94

7.2.15	13 TeV LHC $\sigma(gg \rightarrow \phi \rightarrow \gamma\gamma)$ in the $SVU\psi$ model with $Y_\psi = -1$	95
7.2.16	13 TeV LHC $\sigma(gg \rightarrow \phi \rightarrow \gamma\gamma)$ in the $M_\phi - y_U$ plane for the $SVU\psi$ model	95
7.3.1	Values of $\kappa_{\phi gg}$ and $\kappa_{\phi\gamma\gamma}$ compatible with the 750 GeV excess	96
7.3.2	Regions of parameter space compatible with the 750 GeV excess in 2HDM-II+VLL+VLQ model	97
7.3.3	Regions of parameter space compatible with the 750 GeV excess in 2HDM-X+VLL+VLQ model	98
7.3.4	Regions of parameter space compatible with the 750 GeV excess in 2HDM-I+VLL+VLQ model	99
9.1.1	Feynman diagrams for dark matter self annihilation channels	106
9.2.1	Feynman diagrams for dark matter direct detection processes	108
9.2.2	Relic density and direct detection cross section in $SVU\psi$ model	110
9.2.3	Relic density and direct detection cross section in the $M_\phi - y_U$ plane for the $SVU\psi$ model	111
A.0.18	TeV LHC constraints from $\gamma\gamma, \tau\tau, tt$ channels	117
A.0.2	$\sigma(gg \rightarrow \phi)$ in the 8 TeV and 14 TeV LHC	119

List of Tables

1.1	Representations of the fermions under the SM gauge group	2
-----	--------------------------------------------------------------------	---

Chapter 1

Introduction

The standard model (SM) of particle physics has been extremely successful in describing nature at energy scales up to about ~ 100 GeV. All the particles predicted by the SM have been discovered by experiments, with the Higgs boson discovery announced recently on 4th July 2012 at the LHC [13, 14]. The interaction strengths among the SM particles are measured and are in good agreement with SM predictions. These indicate that the SM is the correct description of nature, at least up to about a few 100 GeV. Below we briefly review the standard model.

1.1 The Standard Model

The standard model of particle physics is a description of the fundamental particles in terms of the $SU(3)_c \times SU(2)_L \times U(1)_Y$ gauge theory. The strong interactions among the fundamental particles are described in terms of the $SU(3)_c$ group [15, 16, 17]. The weak and the electromagnetic interactions are described in terms of the $SU(2)_L \times U(1)_Y$ group [18, 19, 20]. The particle spectrum of SM contains three generations of fermions. Each generation furnishes a representation of the SM gauge group as shown in Table 1.1. The Lagrangian

Fermions	$SU(3)_c$	$SU(2)_L$	$U(1)_Y$
$q_L = \begin{pmatrix} u \\ d \end{pmatrix}_L, \begin{pmatrix} c \\ s \end{pmatrix}_L, \begin{pmatrix} t \\ b \end{pmatrix}_L$	3	2	1/6
$l_L = \begin{pmatrix} \nu_e \\ e \end{pmatrix}_L, \begin{pmatrix} \nu_\mu \\ \mu \end{pmatrix}_L, \begin{pmatrix} \nu_\tau \\ \tau \end{pmatrix}_L$	0	2	-1/2
$u_R = u_R, c_R, t_R$	3	0	2/3
$d_R = d_R, s_R, b_R$	3	0	-1/3
$l_R = e_R, \mu_R, \tau_R$	0	0	-1

Table 1.1: The representations of the fermionic particles under the SM gauge group where the subscripts L and R refers to the left handed or right handed components of the fields.

describing the interactions between the SM fermions and the gauge bosons is given by

$$\begin{aligned}
\mathcal{L} = & \bar{l}_L \gamma^\mu (i\partial_\mu - \frac{g}{2} \sigma^a W_\mu^a + \frac{g'}{2} B_\mu) l_L + \bar{l}_R \gamma^\mu (i\partial_\mu + g' B_\mu) l_R \\
& + \bar{q}_L \gamma^\mu (i\partial_\mu - \frac{g}{2} \sigma^a W_\mu^a - \frac{g'}{6} B_\mu - \frac{g_s}{2} \lambda^a G_\mu^a) q_L \\
& + \bar{u}_R \gamma^\mu (i\partial_\mu - \frac{2g'}{3} B_\mu - \frac{g_s}{2} \lambda^a G_\mu^a) u_R \\
& + \bar{d}_R \gamma^\mu (i\partial_\mu + \frac{g'}{3} B_\mu - \frac{g_s}{2} \lambda^a G_\mu^a) d_R
\end{aligned} \tag{1.1.1}$$

where σ^a are the Pauli matrices, λ^a are the Gell-Mann matrices and W_μ^a , B_μ , G_μ^a are the gauge fields for the $SU(2)$, $U(1)$ and $SU(3)$ gauge groups respectively. The kinetic energy terms for the gauge fields are given by

$$\mathcal{L} = -\frac{1}{4} W^{a\mu\nu} W_{\mu\nu}^a - \frac{1}{4} B^{\mu\nu} B_{\mu\nu} - \frac{1}{4} G^{a\mu\nu} G_{\mu\nu}^a \tag{1.1.2}$$

with $W_{\mu\nu}^a = \partial_\mu W_\nu^a - \partial_\nu W_\mu^a - g\epsilon^{abc} W_\mu^b W_\nu^c$, $B_{\mu\nu} = \partial_\mu B_\nu - \partial_\nu B_\mu$, $G^{a\mu\nu} = \partial_\mu G_\nu^a - \partial_\nu G_\mu^a - g_s f^{abc} G_\mu^b G_\nu^c$ where f^{abc} is the structure constant for the $SU(3)$ group. As can be seen from Table 1.1, the SM fermions are ‘‘chiral’’ i.e. one cannot write down a gauge invariant mass term for them. In general, chiral fermions render the gauge symmetry anomalous through the Adler-Bell-Jackiw (ABJ) anomaly [21, 22]. The divergence of the symmetry current $J_\mu^{g_i, a}$

corresponding to the gauge group g_i is given as

$$\begin{aligned} \partial^\mu J_\mu^{g_i, a} &= -\frac{1}{64\pi^2} D_{a,b,c} \epsilon^{\mu\nu\alpha\beta} F_{\mu\nu}^{g_j, b} F_{\alpha\beta}^{g_k, c} \text{ with} \\ D_{a,b,c} &= \text{tr} \left[\{t_{g_i, a}^L, t_{g_j, b}^L\} t_{g_k, c}^L \right] - \text{tr} \left[\{t_{g_i, a}^R, t_{g_j, b}^R\} t_{g_k, c}^R \right] \end{aligned} \quad (1.1.3)$$

where $F_{\mu\nu}^{g_r, b, c}$ are the field strengths for the gauge fields corresponding to the gauge group g_r (generated by the $t_{g_r, a}$'s) under which the fermions transform as $\psi^{L,R} \rightarrow \exp[i t_{g_i, a}^{L,R} \theta_{g_i, a}^{L,R}] \psi^{L,R}$ and the trace (tr) is to be taken over all the fermionic species. It is remarkable that in the SM, the quantum numbers of the quarks and the leptons are such that, the anomaly is precisely canceled once the trace is taken over a complete generation. For example, let us consider the case when $g_i = g_j = g_k = U(1)_Y$. Then using Table 1.1 we have from Eq. (1.1.3)

$$\begin{aligned} \partial^\mu J_\mu^Y &= 3 \times 2 \times \left(-\frac{1}{6}\right)^3 + 3 \times \left(\frac{2}{3}\right)^3 + 3 \times \left(-\frac{1}{3}\right)^3 + 2 \times \left(\frac{1}{2}\right)^3 + (-1)^3 \\ &= 0 \end{aligned} \quad (1.1.4)$$

1.1.1 The Higgs mechanism

The mass terms for the fermions and the gauge fields are generated through the Higgs mechanism [23]. One introduces a complex scalar H known as the Higgs field, which is an $SU(2)$ doublet and has hypercharge $Y = 1/2$. The Lagrangian for the Higgs field is given by

$$\mathcal{L} = (D_\mu H)^\dagger (D^\mu H) + \mu^2 H^\dagger H - \lambda (H^\dagger H)^2 \quad (1.1.5)$$

with $\mu^2 > 0$, and $D_\mu H$ is the co variant derivative of H given by

$$D_\mu H = \left(\partial_\mu - i \frac{g}{2} \sigma^a W_\mu^a - i \frac{g'}{2} B_\mu \right) H. \quad (1.1.6)$$

The H can be parametrized as $H = (H_1 + iH_2, H_3 + iH_4)^T$. The potential term in Eq. (1.1.5) is minimized for $H^\dagger H = v^2 = \mu^2/\lambda$ which is identified with the vacuum expectation value (VEV) $\langle H^\dagger H \rangle$ of $H^\dagger H$. The observed value of v is 246 GeV [24]. The VEV of H can be

chosen as¹

$$\langle H \rangle = \frac{1}{\sqrt{2}} \begin{pmatrix} 0 \\ v \end{pmatrix} \quad (1.1.7)$$

which breaks the global part of the $SU(2)_L \times U(1)_Y$ symmetry down to the $U(1)_Q$ subgroup generated by $Q = T_3 + Y$: $\langle H \rangle \rightarrow \exp[i\alpha Q]\langle H \rangle = \langle H \rangle$, where $T^3 = \sigma_3/2$. This $U(1)_Q$ subgroup is identified with the electromagnetic gauge group and the corresponding gauge field A_μ is identified with the photon. In this way the SM unifies the weak and the electromagnetic interactions. Evaluating \mathcal{L} on the minima we have

$$\mathcal{L} = \frac{1}{4}g^2v^2W^{+\mu}W_\mu^- + \frac{1}{8}v^2(-gW^{3\mu} + g'B^\mu)(-gW_\mu^3 + g'B_\mu) \quad (1.1.8)$$

which yields three massive gauge bosons. To see this, we diagonalize the quadratic terms in Eq. (1.1.8) by introducing the new fields

$$\begin{aligned} W^{\pm\mu} &= (1/\sqrt{2})(W_1^\mu \pm iW_2^\mu) \\ Z^\mu &= (\cos\theta_W W^{3\mu} - \sin\theta_W B^\mu) \\ A^\mu &= (\sin\theta_W W^{3\mu} + \cos\theta_W B^\mu) \end{aligned} \quad (1.1.9)$$

with $\tan\theta_W = g'/g$. In terms of these new fields, the \mathcal{L} is given by

$$\mathcal{L} = \frac{1}{4}g^2v^2W^{+\mu}W_\mu^- + \frac{1}{8}(g^2 + g'^2)v^2Z^\mu Z_\mu \quad (1.1.10)$$

from which we identify the mass terms for the W and Z bosons as $m_W = gv/2$ and $m_Z = \sqrt{g^2 + g'^2}v/2$. The A_μ boson remains massless as expected.

The potential term in Eq. (1.1.5) has an accidental global $SO(4)$ symmetry, acting on $(\phi_1, \phi_2, \phi_3, \phi_4)^T$. Because of the gauging, the $SO(4)$ symmetry is only an approximate sym-

¹In terms of component fields, the minimization condition can be written as $H_1^2 + H_2^2 + H_3^2 + H_4^2 = v^2$ which describes a three sphere. The points on this sphere are related to one another by $SU(2)$ rotations. The VEV of H can be chosen to be any point on this sphere. Physical observables do not depend on which point we choose.

metry which becomes exact in the limit $g' \rightarrow 0$. After the electroweak symmetry breaking, the $SO(4)$ is spontaneously broken down to an $SU(2)_V$ subgroup. The would be Goldstone bosons of the symmetry breaking transform as a triplet under the $SU(2)_V$. This approximate $SU(2)_V$ global symmetry, known as the ‘‘custodial symmetry’’ [25] is responsible for the protection of the tree level relation $m_W^2 = m_Z^2 \cos^2 \theta_W$.

The Higgs mechanism also gives masses to the SM fermions through the Yukawa couplings. The Lagrangian involving the Yukawa couplings is given by

$$-\mathcal{L}^{Yuk} = y_{ij}^d \bar{q}_L^i H d_R^j + y_{ij}^u \bar{q}_L^i \tilde{H} u_R^j + y_{ij}^l \bar{l}_L^i H l_R^j + h.c. \quad (1.1.11)$$

where i, j are generation indices and $\tilde{H} = i\sigma_2 H^*$. The y matrices are complex and off-diagonal in general. The mass matrix for the fermions is obtained by plugging in the VEV of H in Eq. (1.1.11) as

$$-\mathcal{L}^{mass} = \frac{v}{\sqrt{2}} \left(y_{ij}^d \bar{d}_L^i d_R^j + y_{ij}^u \bar{u}_L^i u_R^j + y_{ij}^l \bar{l}_L^i l_R^j + h.c. \right). \quad (1.1.12)$$

We can diagonalize the mass matrices by bi-unitary transformations as $d_L \rightarrow U_{d_L} d_L$, $d_R \rightarrow U_{d_R} d_R$, $u_L \rightarrow U_{u_L} u_L$, $u_R \rightarrow U_{u_R} u_R$, $l_L \rightarrow U_{l_L} l_L$, $l_R \rightarrow U_{l_R} l_R$. These transformations does not change the neutral currents, since $\bar{u}_{L,R}^i \gamma^\mu u_{L,R}^i$, $\bar{d}_{L,R}^i \gamma^\mu d_{L,R}^i$ remains invariant. However, the charge currents are transformed as $\bar{u}_L^i \gamma^\mu d_L^j \rightarrow \bar{u}_L^i \gamma^\mu (U_{u_L}^\dagger U_{d_L})_{ij} d_L^j$. The matrix $V_{CKM} = U_{u_L}^\dagger U_{d_L}$ is called the Cabibbo–Kobayashi–Maskawa (CKM) matrix [26, 27]. V_{CKM} has four independent parameters, three mixing angles and one complex phase. The complex phase is responsible for the CP-violation in the quark sector. The corresponding transformations in the lepton sector leaves the lepton charge currents $\bar{l}_L^i \gamma^\mu \nu_L^i$ invariant. Therefore, the lepton sector of the SM conserves CP exactly and also conserves the lepton number separately for each generation. In the rotated basis the mass terms of the fermions are simply given as

$$\mathcal{L}^m = \sum_f m_f \bar{f} f = \sum_f \frac{y_f}{\sqrt{2}} v \bar{f} f \quad (1.1.13)$$

where y_f are the diagonal Yukawa couplings.

1.1.2 The Higgs boson

The fluctuations of the H around its VEV can be parametrized as

$$H = U(x) \begin{pmatrix} 0 \\ (v+h)/\sqrt{2} \end{pmatrix} \quad (1.1.14)$$

where $U(x)$ is an element of the group $SU(2) \equiv [SU(2)_L \times U(1)_Y]/U(1)_Q$. We can choose the unitary gauge in which $U(x) = 1$ and the only remaining degree of freedom h is identified with the Higgs boson. Putting Eq. (1.1.14) in Eq. (1.1.5) we have the Higgs mass given by $m_h = \sqrt{2\lambda}v$. The couplings of the h with the SM gauge bosons are given as

$$\mathcal{L}^{hVV} = \frac{m_W^2}{v^2} h^2 W^{+\mu} W_\mu^- + \frac{m_Z^2}{2v^2} h^2 Z^\mu Z_\mu + \frac{2m_W^2}{v} h W^{+\mu} W_\mu^- + \frac{m_Z^2}{v} h Z^\mu Z_\mu. \quad (1.1.15)$$

The h plays an important role in unitarizing the theory. Without the hWW coupling the scattering amplitude $W_L W_L \rightarrow W_L W_L$ diverges at high energy [28, 29], where W_L refers to the longitudinal polarization of W . The h cancels the divergence as a result of the special structure of the hWW coupling dictated by the underlying gauge invariance. The couplings of the h with the SM fermions are given as

$$\mathcal{L}^{hff} = - \sum_f \frac{m_f}{v} h \bar{f} f. \quad (1.1.16)$$

We can see that the Yukawa couplings of the SM fermions are proportional to their masses which is due to the fact that the fermion masses arise from the Higgs VEV. With the knowledge of the Higgs couplings, we can study the Higgs phenomenology which we briefly discuss below.

Higgs phenomenology:

We start by summarizing the Higgs decay processes [30]. For $m_h \lesssim 130$ GeV, the dominant decay channel is the $h \rightarrow bb$ mode with branching ratio (BR) $\sim 80\%$ followed by $h \rightarrow \tau\tau$ with BR $\sim 7\%$. The loop level process $h \rightarrow gg$ mediated by the top loop and $\gamma\gamma$ mediated by

the top and W loop has $\text{BR} \sim 9\%$ and 0.2% respectively around $m_h \sim 120$ GeV. The main production processes for the h at the LHC are $gg \rightarrow h$ [31, 32], $q\bar{q} \rightarrow h + V$ [33, 34] and $qq \rightarrow V^*V^* \rightarrow qq + h$ [35, 36, 37] where V denotes the vector bosons Z, W . For $m_h < 130$ GeV, a very promising discovery channel for the Higgs is the $h \rightarrow \gamma\gamma$ [13, 14, 38, 39]. The excellent mass resolution in the di-photon channel enables the signal to stand out above the background in spite of the very small branching ratio. It was the di-photon channel in which the discovery of the 125 GeV Higgs was first reported [13, 14]. Other than the di-photon channel, the Higgs boson is also observed in the $h \rightarrow ZZ^* \rightarrow 4l$ [13, 14, 40, 41], $h \rightarrow WW^* \rightarrow l\nu l\nu$ [13, 14, 42, 43], $h \rightarrow \tau\tau$ [44, 45, 46, 47], $h \rightarrow bb$ [45, 48, 49] channels. To confirm the SM Higgs sector, the Higgs couplings to the SM particles should match their measured SM values. It turns out that the Higgs couplings, as inferred from the measurements of the Higgs production rates and the branching ratios at the LHC agree with their corresponding SM values [50] within the error bars.

1.2 Drawbacks of the standard model

Despite its enormous success, the SM has several shortcomings, both on the theoretical and observational sides. One of the main theoretical drawbacks of the SM is that the Higgs mass is not radiatively stable. When quantum corrections are included, the bare Higgs mass receives corrections that are quadratic in the cut-off scale (Λ). For example, the top one-loop contribution (Fig. 1.2.1) to the Higgs mass squared is given by $m_h^2 = m_{h0}^2 + 3y_t^2\Lambda^2/(8\pi^2)$ where m_{h0} is the bare Higgs mass and y_t is the top Yukawa coupling. If there is no new physics up to the Planck scale then $\Lambda \approx 10^{19}$ TeV and therefore the m_{h0} has to be fine-tuned to achieve a light Higgs mass of 125 GeV. This is referred to as the ‘‘Higgs fine-tuning problem’’. Any parameter which has the property that its quantum corrections are less than or of the order of the parameter itself, is called a ‘‘natural’’ parameter. According to ’t Hooft’s ‘‘naturalness’’ argument [51], a given parameter κ in any theory can be ‘‘natural’’ only if there is an enhanced symmetry in the limit of $\kappa \rightarrow 0$. The Higgs mass fine-tuning will be small if

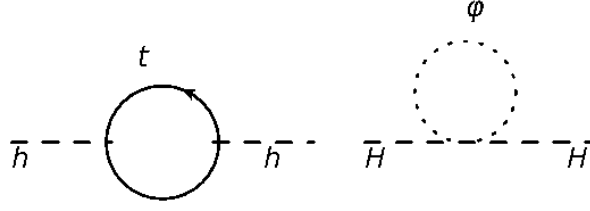


Figure 1.2.1: Top loop contribution to the Higgs mass correction (left) and the ϕ loop correction to μ^2 (right).

$\delta m_h^2 \sim m_h^2$ that is

$$m_h^2 = \frac{3y_t^2 \Lambda^2}{8\pi^2}. \quad (1.2.1)$$

So the Higgs fine-tuning will be small only if the quantum corrections are cut off at the scale Λ with $\Lambda^2 \lesssim 8\pi^2(125)^2/3y_t^2 \text{GeV}^2 \lesssim (1\text{TeV})^2$. The quadratic sensitivity to the high scale physics can also be seen in dimensional regularization. Let us consider a real SM singlet heavy scalar ϕ of mass M_ϕ interacting with the Higgs field as described by the Lagrangian

$$\mathcal{L} = \mathcal{L}_{SM} - \lambda_\phi \phi^2 H^\dagger H - \frac{1}{2} M_\phi^2 \phi^2. \quad (1.2.2)$$

The one loop correction to the μ^2 term in Eq. (1.1.5) due to the ϕ loop (Fig. 1.2.1) is given by [52, 53]

$$\delta\mu^2 = -\frac{\lambda_\phi M_\phi^2}{16\pi^2} \left(\frac{2}{\epsilon} - \log M_\phi^2 \right) \quad (1.2.3)$$

which in the minimal subtraction scheme (\overline{MS}) becomes

$$\delta\mu^2 = \frac{\lambda_\phi M_\phi^2}{16\pi^2} \log \frac{M_\phi^2}{M^2} \quad (1.2.4)$$

where M is an arbitrary renormalization scale. From Eq. (1.2.4) we again see that the μ^2 and hence m_h^2 is quadratically sensitive to the ϕ mass. The considerations above suggest that if the Higgs sector is to be rendered natural, there should be some new physics at an energy scale of $\lesssim 1$ TeV that cancels the quadratic divergences.

Apart from the fine tuning problem, the SM also cannot explain some of the experimental observations like dark matter, baryon asymmetry of the universe and neutrino mass. Here we briefly discuss these issues.

Dark matter:

The observation of the rotation curves of galaxies and clusters of galaxies strongly indicate that our universe contains dark matter. This cannot be accounted for in the SM. The existence of dark matter is further supported by the gravitational lensing studies of the bullet cluster. Several BSM theories have been proposed to explain dark matter. Most of them assume that dark matter is a weakly interacting massive particle (WIMP). WIMPs have ~ 100 GeV to 1 TeV masses and have electroweak interactions with the SM particles.

Baryon asymmetry:

It is observed that our observable universe is almost entirely composed of baryonic matter and no anti-baryonic matter. If the big bang produced equal amount of matter and anti-matter as is reasonable to assume, there must exist some processes which leads to the baryon anti-baryon asymmetry during the evolution of the universe. One proposal to address this asymmetry is “baryogenesis” which requires a large CP-violation. The required amount of CP-violation is not present in the SM.

Neutrino mass:

In the SM as constructed earlier, the neutrinos are massless. However, neutrino oscillation experiments suggest that the neutrinos should have a tiny mass of order 10^{-2} eV. One can generate the mass terms for the neutrinos in the same way as for the other SM fermions by adding Yukawa terms. But in order to get 10^{-2} eV size mass, the Yukawa couplings has to be extremely small which is an unattractive feature of this proposal.

Beyond the standard model:

To address the shortcomings of the SM, several theories beyond the standard model (BSM) have been proposed. Examples of these BSM theories are, supersymmetric theories (SUSY), extra-dimensional models, little-Higgs models, composite Higgs models, two Higgs doublet models etc. In the following chapter we will briefly describe some of these theories.

As we shall see in the next chapter, many BSM theories such as little-Higgs models, extra-dimensional models and strong coupling theories have additional neutral scalars and vector-like fermions as important ingredients. To capture the phenomenology of such models, our main focus in this thesis is to study some effective models of BSM neutral scalars (collectively called ϕ) with vector-like fermions also present. The study of such effective models captures many features present in realistic BSM theories. We present a model independent analysis of a scalar coupled to the SM particles and VLFs. We consider few effective models of BSM neutral scalars with VLFs also present. We focus on the singlet scalar models and the two Higgs doublet model, with VLFs also added. We assume that the scalar is produced by the loop level gluon fusion process ($gg \rightarrow \phi$), as it is usually the dominant production channel. Both the SM fermions and the colored VLFs contribute to the $gg \rightarrow \phi$ process. We present the production cross sections and branching ratios of the neutral scalars for each of these models, highlighting the effects of the VLFs. We also explore the dark matter implications of a singlet scalar model namely the hidden sector dark matter model. Below we briefly summarize few references that are relevant to our work.

An effective Lagrangian analysis of new heavy scalar particles is presented in Ref. [54]. The LHC phenomenology of singlet scalars is studied for example in Refs. [55, 56]. The phenomenology of the abelian hidden sector model is studied in Ref. [57]. The phenomenology of the abelian hidden sector model with VLFs added is studied in Ref. [58]. Ref. [59] studies the dark matter implications of the abelian hidden sector model with fermions added.

Refs. [60, 61] consider the possibility that the observed 125 GeV state at the LHC is a CP-odd scalar, and the former shows that this possibility is disfavored by the LHC data. Refs. [62, 63] analyze 2HDM Types I and II taking into account the 125 GeV LHC

data, all pre-LHC constraints and results of the heavy-Higgs searches in various channels. Ref. [64] performs a global fit of general 2HDMs using ATLAS, CMS and Tevatron results. Refs. [65, 66, 67, 68, 69] shows the allowed parameter space of the 2HDM-II, applying theoretical (perturbativity, unitarity and vacuum stability) and experimental (LEP, Tevatron and LHC 125 GeV Higgs data, precision observables and B -physics and electric dipole moment measurements) constraints. Ref. [70] also includes the heavy Higgs exclusion limits to constrain the 2HDM. LHC 8 TeV constraints on the 2HDM parameter-space are also discussed in Refs. [71, 72, 73, 74, 75]. The heavy neutral scalars of the 2HDM, namely A and H , are studied in Ref. [76], where the LHC 8 TeV exclusion and 14 TeV reach from the processes $gg \rightarrow H \rightarrow AZ$ and $gg \rightarrow A \rightarrow HZ$ are presented. Ref. [77] constructed an $SO(5)$ symmetric 2HDM which naturally realizes the "alignment limit" and puts constraints on its parameter space from the 8 TeV LHC data. Ref. [78] puts limits on the triple Higgs couplings and presents a set of benchmark points for probing SM-Higgs pair production and the search of heavy Higgs bosons through non-standard decay channels (i.e decays of A, H that involves at least one Higgs boson in the final state). Ref. [79] calculates the loop factors for the AVV couplings in the MSSM and the 2HDM with a heavy chiral fourth generation. Ref. [80] studies $A \rightarrow WW, ZZ$ decays and compares this with the corresponding CP-even scalar decays in 2HDM-II, and also with a chiral fourth generation or additional heavy vector-like quarks (VLQ) added. In addition to these, here we also include the effects of VLFs on $A \rightarrow \gamma\gamma, Z\gamma$ decays. The outline of the thesis goes as follows.

In Chapter 2 we discuss some of the BSM theories. Specifically, we describe the supersymmetric extensions of the SM, extra-dimensional models, little-Higgs models, composite Higgs models and models with extended scalar sector. Chapter 3 we present a model independent study of neutral scalars (ϕ) coupled to the SM fermions and new VLFs. We obtain the 8 TeV and 14 TeV LHC $\sigma(gg \rightarrow \phi)$. We also discuss the constraints on the effective couplings from the 8 TeV LHC results. In Chapter 4 we study an $SU(2)$ singlet CP-odd scalar (A) coupled to the VLFs which are either an $SU(2)$ singlet or an $SU(2)$ doublet. We present the branching ratios of A and the effective Agg coupling in each of these models. In Chapter 5 we briefly review the two Higgs doublet model. In Chapter 6 we briefly dis-

discuss the phenomenology of neutral scalars (A, H) in the 2HDM type II and X where we present the branching ratios of A, H and the effective Hgg, Agg couplings. We subsequently introduce the VLFs to the 2HDM type-II and X. We separately consider two cases, one in which the VLFs mix with the SM third generation fermions and one in which the VLF mixing with the SM fermions are shut off. We present the branching ratios of A, H and the effective Agg, Hgg couplings for each of this model. We also obtain the constraint on the parameter space from the 8 TeV LHC $\tau\tau$ channel results. In Chapter 7 we specialize to the diphoton channel $\phi \rightarrow \gamma\gamma$. We present a model independent analysis of the 13 TeV LHC $\sigma(gg \rightarrow \phi \rightarrow \gamma\gamma)$ and discuss the constraints from the 8 TeV LHC results and from perturbative unitarity. We then consider the 2HDM and a singlet scalar model with VLFs also present. In the 2HDM we consider the types-II, X and I. We obtain the 13 TeV LHC $\sigma(gg \rightarrow \phi \rightarrow \gamma\gamma)$ for each of these models. We also present the constraints on the parameter space from the 8 TeV LHC results and the perturbative unitarity. The singlet scalar model can also provide a dark matter candidate. In Chapter 8 we present a brief review of WIMP dark matter. We discuss the dark matter implications of the singlet scalar model in Chapter 9 where we present the regions of the parameter space which gives the correct dark matter relic density. We also present in Chapter 9 the constraints on the parameter space from the dark matter direct detection limits. In Chapter 10 we present the summary and conclusions of the thesis.

Chapter 2

Beyond the Standard Model

As mentioned in the introduction, the SM has a few drawbacks. To address these, various theories beyond the standard model (BSM) have been proposed. In this chapter we briefly discuss some of the BSM theories, namely theories with extended scalar sector, supersymmetric theories, extra-dimensional theories, little-Higgs theories and composite Higgs theories. We also discuss some properties of the vector-like fermions that are present in many of the BSM theories.

2.1 Extended scalar sector

One of the simplest extensions of the SM is obtained by simply extending its scalar sector. There are several possible ways to extend the SM scalar sector. One option is to add an extra SU(2) singlet neutral scalar ϕ which is charged under a $U(1)$ gauge symmetry. This model is called the abelian hidden sector model. One can introduce new fermions (ψ) in this model along with a Z_2 symmetry under which ψ is odd and the SM fermions are even. In this case, the lightest Z_2 odd fermion can be a dark matter candidate.

Another option is to introduce new SU(2) doublet scalars. One important example of such models is the two Higgs doublet model (2HDM) which has two SU(2) scalar doublets Φ_1, Φ_2 . Electroweak symmetry breaking (EWSB) is achieved by minimizing the 2HDM potential $V(\Phi_1, \Phi_2)$ with respect to Φ_1 and Φ_2 . The 2HDM has two CP-even scalars h, H

one CP-odd scalar A and a charged scalar H^\pm . Commonly, the lightest CP-even scalar is identified with the 125 GeV Higgs boson. In general, the SM fermions will have Yukawa couplings with both Φ_1 and Φ_2 and there will be flavor changing neutral currents (FCNC). In the 2HDM these FCNCs are usually forbidden by a Z_2 symmetry. Depending on the Z_2 transformation properties of the SM fermions several types of 2HDM have been proposed. The commonly studied types are so called 2HDM type-I, II and X. The measurements of the Higgs observables at the 8 TeV and 13 TeV LHC [81, 82] requires that the Higgs couplings to the SM particles are close to their SM values. In the 2HDM this can be ensured by considering the so called “alignment limit” where the Higgs coupling to the SM particles become identical to those in the SM. The details of the 2HDM is presented in Chapter 5.

2.2 Supersymmetry

An elegant solution of the Higgs sector fine-tuning problem is provided by supersymmetry (SUSY) [83, 84, 85, 86, 87, 88, 89]. SUSY is generated by extending the Poincare algebra to include N set of fermionic generators ($Q^i, \bar{Q}^i, i = 1, \dots, N$) which transforms as two component spinors $[(1/2, 0), (0, 1/2)]$ respectively] under the Lorentz transformation. Therefore, SUSY transformations takes bosonic degree of freedom into fermionic ones and vice versa. The SUSY algebra is invariant under the $U(N)$ rotations: $Q^i \rightarrow U_{ij}Q^j, U \in U(N)$. This symmetry is known as the “R-symmetry” which acts as a global symmetry on the physical states. Each irreducible representation of the SUSY algebra is called a supermultiplet. Each supermultiplet contains equal number of degenerate bosonic and fermionic degree of freedoms. A simple example of a supermultiplet is the chiral supermultiplet which contains a two component Weyl fermion and a complex scalar. In any supersymmetric theory all the particles inside a supermultiplet must transform identically under the underlying gauge (local or global) symmetry of the theory. In SUSY theories there is no quadratic divergence of the scalar mass, since for every bosonic (fermionic) loop contributing to the scalar mass correction, there is a fermionic (bosonic) loop that contributes with an opposite sign and equal magnitude [90, 91]. The solution to the Higgs fine tuning problem is thus obtained by

a suitable supersymmetric extension of the SM. The simplest of such extensions, known as the minimal supersymmetric standard model (MSSM) is a $N = 1$ supersymmetric extension of the SM. In MSSM, each of the SM particles have a single supersymmetric partner. For example, the quark doublet (t_L, b_L) is accompanied by the (complex) scalar doublet $(\tilde{t}_L, \tilde{b}_L)$ and so on. Similarly, each massless gauge boson in the SM has a (Weyl) fermionic partner. Supersymmetrising the Higgs, however requires introduction of two chiral supermultiplets which consists of two scalar doublets H_u, H_d with $Y = \pm 1/2$ and their corresponding superpartners \tilde{H}_u, \tilde{H}_d . The second multiplet is required to cancel the gauge anomaly from the first one.

SUSY cannot be an exact symmetry of nature all the way down to the lowest possible scale. If it were, we would have observed the superpartners of all the SM particles, since in an exact SUSY all the particles in a given super multiplet are degenerate. In the MSSM, SUSY breaking is introduced in the Lagrangian through terms of positive mass dimensions. Such terms, known as the soft breaking terms, are irrelevant at the ultra-violet (UV) scale where SUSY becomes exact. The soft breaking terms introduces a mass splitting among the particles within a given supermultiplet. Therefore, when we compute the Higgs mass loop corrections, contributions from different particles in the supermultiplet no longer cancel each other and introduces a quadratic sensitivity to the mass splitting. If the mass splittings are not larger than $\mathcal{O}(TeV)$ then the Higgs mass remains natural. For the MSSM, the R-symmetry is simply $U(1)_R$. The R -charges of the SM particles differ from their super partners by ± 1 ¹. Therefore, the lightest supersymmetric particle (LSP) cannot decay to only SM particles and become absolutely stable. Hence the LSP can be a good dark matter candidate. The MSSM also successfully unifies [92, 93, 94] the gauge couplings g, g', g_s .

¹Since $[R, Q] = Q, RQ|\psi\rangle = (QR + Q)|\psi\rangle = (R_\psi + 1)Q|\psi\rangle$ where $R|\psi\rangle = R_\psi|\psi\rangle$, R being the generator of $U(1)_R$.

2.3 Extra-dimensional models:

In extra-dimensional models one conjectures the existence of extra spatial dimensions so that locally the space-time looks like $M^4 \times E^d$, where M^4 is the Minkowski space and E^d is a d dimensional space representing the extra dimensions. There are many varieties of such models which can be broadly divided into two classes; one in which the extra dimension is flat and one in which the extra dimension is “warped”. Below we briefly describe these two types of models.

2.3.1 Flat extra dimension

In the flat extra dimensional models, the metric on M^4 does not depend on the extra-dimensional co-ordinates. Let us consider a simple example where the space-time is globally $M^4 \times T^n$ with the metric

$$ds^2(x) = g_{\mu\nu}(x)dx^\mu dx^\nu - \delta_{ab}dy^a dy^b. \quad (2.3.1)$$

where x^μ are the coordinates on M^4 and y^a are extradimensional coordinates. The SM fields are assumed to be localized on an M^4 subspace and only gravity can leak into the extra-dimensions. This leads to an effective reduction of the gravitational force as viewed by a 4-dimensional observer. To see this, let’s consider the Eienstein-Hilbert action

$$\mathcal{S}^{4+n} = \frac{1}{16\pi G_{4+n}} \int d^4x dy_1 \cdots dy_n \sqrt{-g_{4+n}} \mathcal{R}_{4+n} \quad (2.3.2)$$

where G_{4+n} is the $4+n$ dimensional Newton’s constant and \mathcal{R}_{4+n} is the Ricci scalar for the metric in Eq. (2.3.1). Putting the metric of Eq. (2.3.1) in Eq. (2.3.2) and integrating over the extra-dimensions, the effective 4-d action is given as

$$\mathcal{S}^{4d} = \frac{V^n}{16\pi G_{4+n}} \int d^4x \sqrt{-g_4} \mathcal{R}_4 \quad (2.3.3)$$

where \mathcal{R}_4 is the 4-d Ricci scalar for the 4-d metric $g_{\mu\nu}$ and V^n is the volume of the extra-dimension. As can be seen from Eq. (2.3.3), the 4-d Newton's constant is given by $G_N = G_{4+n}/V^n$. So, in this scenario the smallness of G_N is explained by the volumetric suppression of the fundamental Newton's constant G_{4+n} . A realistic version of this model is the ADD model [95].

2.3.2 Warped extra dimension

In warped extra-dimensional models, one adds one extra compact spatial dimension and the metric on the 4-d Minkowski space depends on the fifth dimension. An explicit example of this scenario is provided by the Randall-Sundrum (RS) model [96]. The RS model uses the metric

$$ds^2 = e^{-k\phi R} g_{\mu\nu}(x) dx^\mu dx^\nu - R^2 d\phi^2 \quad (2.3.4)$$

where $-\pi < \phi \leq \pi$ and k, R are constants with mass dimensions 1, -1 respectively. We can see that the distance scales (or equivalently the energy scales) depend on the fifth dimensional coordinate. In the original proposal of Randall and Sundrum, all the SM particles are localized on a 4-dimensional brane at $\phi = \pi$. To see how the RS scenario solve the hierarchy problem, let us consider the following Lagrangian for a brane localized scalar field ϕ which has a bare VEV v_0 :

$$\mathcal{L} = \int d^4x \sqrt{-g_{ind}} \left[g_{ind}^{\mu\nu} (\partial_\mu \phi)^\dagger (\partial_\nu \phi) - \lambda (\phi^\dagger \phi - v_0^2) \right] \quad (2.3.5)$$

where $g_{ind}^{\mu\nu}$ is the induced metric on the brane. From Eq. (2.3.5) we have $g_{ind}^{\mu\nu} = e^{-k\pi R} \eta^{\mu\nu}$, where $\eta^{\mu\nu}$ is the usual Minkowski metric. Then the Lagrangian in Eq. (2.3.5) becomes

$$\mathcal{L} = \int d^4x \left[e^{-2\pi k R} \eta_{\mu\nu} (\partial^\mu \phi)^\dagger (\partial^\nu \phi) - \lambda e^{-4\pi k R} (\phi^\dagger \phi - v_0^2)^2 \right]. \quad (2.3.6)$$

To canonically normalize the kinetic term, we rescale ϕ as $\phi \rightarrow e^{-k\pi R}\phi$. Then Eq. (2.3.6) becomes

$$\mathcal{L} = \int d^4x \left[\eta_{\mu\nu} (\partial^\mu \phi)^\dagger (\partial^\nu \phi) - \lambda (\phi^\dagger \phi - e^{-2\pi k R} v_0^2)^2 \right]. \quad (2.3.7)$$

We can see that the bare value of the scalar VEV is warped down to a smaller value $v = v_0 e^{-k\pi R}$. As a result, although $v_0 \sim \mathcal{O}(M_{pl})$, if we chose $kR \sim \mathcal{O}(10)$, v can be of the order of the electroweak scale 246 GeV. In subsequent years, many papers [97, 98, 99] considered the possibility of SM fields also living in the bulk of the space-time. One consequence of the SM fields propagating in the bulk is the existence of the discrete Kaluza-Klein (KK) modes for each bulk field. For any given bulk field, the mode with the lowest energy (zero mode that has no nodes along the 5-th dimension) is identified with the corresponding SM field. The KK modes are separated from the zero modes by a mass gap of about $\sim k e^{-k\pi R} \sim \mathcal{O}(1)$ TeV. A difficulty arises when we consider fermionic fields in the bulk. In 4-d we can label the fermionic states by their γ_5 eigenvalues, as γ_5 commutes with all the Lorentz generators. But in 5-d, the γ_5 is used up in constructing the 5-d Clifford algebra $[\Gamma^M, \Gamma^N] = 2\eta^{MN}$ where $\Gamma^\mu = \gamma^\mu, \mu = 0, 1, 2, 3$ and $\Gamma^4 = i\gamma^5$. Therefore, if a 5-d fermion ψ transforms under some gauge group (G), then the $\psi_L = (1/2)(1 - \gamma_5)\psi$ and $\psi_R = (1/2)(1 + \gamma_5)\psi$ must transform exactly the same way under G . This leads to vector-like fermions as opposed to the chiral fermions of the SM. This problem is solved when the extra dimension, a circle, is orbifolded by identifying the points ϕ and $-\phi$. We can define a parity operator P_5 such that $P_5(\phi) = -\phi$ and label the fermionic states by their P_5 eigenvalues ± 1 (since $P_5^2 = 1$). We can define the fields ψ_+ and ψ_- as $P_5(\psi_+) = \psi_+, P_5(\psi_-) = -\psi_-$. When we KK decompose, only the ψ_+ will have a zero mode since ψ_- , being P_5 -odd, must have a node along the 5-th dimension. The chiral fermions of the SM are identified with the zero modes of some fermionic fields. For example, if we want the quark doublet q_L , we introduce the 5-d $SU(2)$ doublet quark field $\psi = (\psi_L, \psi_R)$, impose the condition $P_5(\psi_L) = \psi_L, P_5(\psi_R) = -\psi_R$ and identify the zero mode of ψ_L (ψ_{0L}) with the q_L . The massive modes remains vector-like under the SM gauge group.

2.4 Little-Higgs models:

In little-Higgs (LH) constructions, the Higgs is identified as a pseudo Nambu Goldstone boson (pNGB) of a spontaneously broken global symmetry. LH models necessarily have a bigger symmetry group G which is broken down to one of its subgroups, say \mathcal{H} , by the vacuum expectation value of a scalar field. The SM gauge group is contained within \mathcal{H} . The Goldstone bosons of the symmetry breaking correspond to the generators of the coset space G/\mathcal{H} . A subgroup \mathcal{H}' of G is gauged and as a consequence some of the Goldstone bosons cease to be exact Goldstone bosons and become pNGBs. The 125 GeV Higgs (h) is identified as one of the pNGBs. At the tree level there is no potential for the pNGBs. EWSB occurs by loop level processes. Because of the special structure of LH models the symmetry is broken “collectively” and there are no quadratic divergences in the Higgs mass at one loop. The bigger symmetry group in the LH models requires new vector-like fermions which together with the SM fermions complete the symmetry group representations. As an example we consider the “simplest little-Higgs” model[100, 101] where $G = SU(3)_1 \times SU(3)_2$ which is broken down to the subgroup $\mathcal{H} = SU(2)_1 \times SU(2)_2$ by VEVs of two $SU(3)$ triplet scalars ϕ_1 and ϕ_2 : $\langle \phi_1 \rangle = (0, 0, f_1)^T, \langle \phi_2 \rangle = (0, 0, f_2)^T$. We get 10 goldstone bosons which can be parametrized as

$$\phi_1 = e^{i\pi_1/f_1} \begin{pmatrix} 0 \\ 0 \\ f_1 \end{pmatrix}, \phi_2 = e^{i\pi_2/f_2} \begin{pmatrix} 0 \\ 0 \\ f_2 \end{pmatrix} \quad (2.4.1)$$

where

$$\pi_{1,2} = \begin{pmatrix} -\eta/2 & 0 & h_1 - ih_2 \\ 0 & -\eta/2 & h_3 - ih_4 \\ h_1 + ih_2 & h_3 + ih_4 & \eta \end{pmatrix}_{1,2}.$$

We can see that the fields $H_{1,2} = (h_1 + ih_2, h_3 + ih_4)_{1,2}^T$ transforms as $SU(2)_{1,2}$ doublets and $\eta_{1,2}$ are $SU(2)$ scalars. We now gauge the diagonal part ($SU(3)_V$) of the $SU(3) \times SU(3)$

global symmetry. The SM gauge group $SU(2)_L \in SU(3)_V$. The Lagrangian describing the interactions of the $SU(3)$ gauge fields and the Goldstone boson is given as

$$\mathcal{L} \supset (D_\mu \phi_1)^\dagger (D^\mu \phi_1) + (D_\mu \phi_2)^\dagger (D^\mu \phi_2) \quad (2.4.2)$$

where $D_\mu \phi_i = \partial_\mu \phi_i - ig_i A_\mu^a T^a \phi_i$. As a result of the gauging, only the $SU(3)_V$ remains as an exact global symmetry of the theory. Hence there are only 5 exact NGBs which come from the breaking of the $SU(3)_V$ down to the $SU(2)_V$ (the diagonal part of the $SU(2)_1 \times SU(2)_2$). The other 5 NGBs become pNGB which are massless at the tree level. A combination of H_1 and H_2 is identified with the Higgs field. A potential term for the pNGBs is generated at one loop. The absence of quadratic divergence (at one-loop) is ensured by the fact that the one-loop diagrams contributing to the potential must involve both the gauge couplings, g_1 and g_2 , because if we set any of the g_i to be zero, the original $SU(3) \times SU(3)$ symmetry is restored and all the NGBs are exact NGBs. The one-loop diagrams involving both the g_1 and g_2 are at most logarithmically divergent. In the fermionic sector of this model one introduces new fermions which together with the SM fermions furnish a representation of $SU(3)$. For example, along with the third generation quarks, an $SU(2)$ singlet vector-like top partner (T_L, T_R) is introduced to form the $SU(3)$ triplet $(t_L, b_L, T_L)^T$. The Yukawa Lagrangian is given as

$$\mathcal{L} = \lambda_1 \bar{\psi} \phi_1 T_R + \lambda_2 \bar{\psi} \phi_2 t_R + h.c. \quad (2.4.3)$$

This Lagrangian breaks the $SU(3) \times SU(3)$ to the diagonal $SU(3)$. If we set any of the λ_i to be zero, the $SU(3) \times SU(3)$ is restored which makes the quadratic divergence absent in the Yukawa sector also. Several versions of the little-Higgs model exist in the literature [3, 4, 100, 102, 103, 104, 105]. Interestingly, many of the LH theories [3, 4, 100, 105] have a 2HDM structure.

2.5 Strongly coupled theories

There exists another class of theories that relies on new strong interactions which dynamically breaks the electroweak symmetry. As we have discussed in the introduction, the fine-tuning problem arises in the SM because of the SM Higgs being a fundamental scalar. Theories based on strong dynamics assume that the Higgs is a composite of new fermions and therefore free from the problems associated with fundamental scalars. The new dynamics is assumed to originate from a non-abelian gauge theory, similar to QCD. A concrete realization, amongst many others [106, 107, 108, 109] of this scenario is the minimal composite Higgs model [110] which is based on a global $G_{MCH} = SU(3)_c \times SO(5) \times U(1)$ invariance. The G_{MCH} is spontaneously broken down to $\mathcal{H}_{MCH} = SU(3)_c \times SU(2)_L \times SU(2)_R \times U(1)$ at some scale $f > v$ by some strong dynamics, delivering 4 NGBs that transforms like a doublet under the $SU(2)_L$. This $SU(2)_L$ doublet scalar field is to be identified with the Higgs doublet. The SM gauge bosons are coupled to the conserved currents of the global symmetry G_{MCH} of the strong dynamics thereby gauging a subgroup $G_{SM} = SU(3)_c \times SU(2)_L \times U(1)_Y \subset \mathcal{H}_{MCH}$ of G_{MCH} . The $SU(2)_L \times U(1)_Y$ gauge generators do not coincide with the broken symmetry generators (corresponding to the coset space $G_{MCH}/\mathcal{H}_{MCH}$) and hence they cannot “eat” the NGBs which therefore become pNGBs. To represent $SO(5)$, the fermion content of the SM is enlarged to include extra fermions which together with the SM fermions, furnish a representation of $SO(5)$. One possible fermion representation is a 4 of $SO(5)$. In the quark sector for example one introduces the new quark fields $Q_L, q_R^u, q_R^d, d'_R, u'_R$ and form the $SO(5)$ spinor (4 of $SO(5)$) as

$$\psi_q = \begin{bmatrix} q_L \\ Q_L \end{bmatrix}, \psi_u = \begin{bmatrix} q_R^u \\ u_R \\ d'_R \end{bmatrix}, \psi_d = \begin{bmatrix} q_R^d \\ u'_R \\ d_R \end{bmatrix}. \quad (2.5.1)$$

The electroweak symmetry is broken by the one loop effective potential generated for the H , by the SM top, SM gauge bosons and the new fermion fields. Since $v \rightarrow 0$ as $f \rightarrow 0$, the v is proportional to f and therefore free from the naturalness problem for $f \sim \mathcal{O}(TeV)$.

2.6 Vector-like fermions

As we have discussed above, many BSM theories have vector-like fermions as an important ingredient. Here we briefly discuss some properties of the vector-like fermions (VLF). As mentioned in the introduction, the SM fermions are chiral, that is, the left handed and right handed fermions transform differently under the gauge group. Vector-like fermions have the property that under the gauge group, its right handed component transforms as the conjugate representation of the left handed ones. This allows for a gauge invariant mass term for the VLFs, and therefore the Yukawa couplings of the VLFs to the Higgs boson are not proportional to their masses (M_{VL}). As a direct consequence, the VLFs decouple in the loop level processes in the limit of $M_{VL} \rightarrow \infty$. Therefore, the limits on the VLFs from the Higgs observables are looser. The current direct search limit on the mass of the vector-like top partner is about 920 GeV [111]. The precision electroweak constraints on the VLF mass are discussed for example in Ref. [112]. The LHC signatures of vector-like quarks are studied for example in Refs. [113, 114, 115, 116, 117, 118].

As an example of how the VLFs arise in a concrete model we take the example of the custodially protected RS model [99] based on the $SU(3)_c \times SU(2)_L \times SU(2)_R \times U(1)_X$. To represent the symmetry group, we must add new bulk fermions. For example, the third generation quarks is embedded into a representation of $SU(2)_L \times SU(2)_R \times U(1)_X$ as

$$Q_L \equiv (2, 1)_{1/6} \equiv \begin{pmatrix} t_L^{(+)} \\ b_L^{(+)} \end{pmatrix}, Q_{t_R} \equiv (1, 2)_{1/6} \equiv \begin{pmatrix} t_R^{(+)} \\ b'^{-} \end{pmatrix}, Q_{b_R} \equiv (1, 2)_{1/6} \equiv \begin{pmatrix} t'^{-} \\ b_R^{(+)} \end{pmatrix} \quad (2.6.1)$$

where + and – denotes whether they are P_5 even or odd respectively. We recall from Section 2.3.2 that only the P_5 even fields have zero modes. The Higgs field is taken to be a bi-doublet under $SU(2)_L \times SU(2)_R$ and can be parametrized as

$$\Sigma = \begin{pmatrix} \phi_0^* & \phi^+ \\ -\phi^- & \phi^0 \end{pmatrix}. \quad (2.6.2)$$

The electroweak symmetry is broken by the VEV $\langle \Sigma \rangle = \text{diag}(v, v)/\sqrt{2}$. The gauge interac-

tions for the fermions is given as

$$\mathcal{L}^{gauge} = \bar{Q}_L i\gamma^\mu D_\mu Q_L + \bar{Q}_{t_R} i\gamma^\mu D_\mu Q_{t_R} + \bar{Q}_{b_R} i\gamma^\mu D_\mu Q_{b_R} \quad (2.6.3)$$

where

$$D_\mu = \partial_\mu - i\frac{g_s}{2}G_\mu^a\lambda^a - ieQA_\mu - i\frac{g}{\sqrt{2}}(T^+W_\mu^+ + T^-W_\mu^-) - ig_Z(T^3 - s_W^2Q)Z_\mu. \quad (2.6.4)$$

The 5-d Yukawa Lagrangian is given as

$$-\mathcal{L}^{Yukawa} = \tilde{\lambda}_t \bar{Q}_L \Sigma Q_{t_R} + \tilde{\lambda}_b \bar{Q}_L \Sigma Q_{b_R} + h.c. \quad (2.6.5)$$

Putting in the Σ VEV in Eq. (2.6.5) we get the mass terms for the down type fermions as

$$-\mathcal{L}^{mass} = \frac{\tilde{\lambda}_t v}{\sqrt{2}} \bar{b}_L b'_R + \frac{\tilde{\lambda}_b v}{\sqrt{2}} \bar{b}_L b_R. \quad (2.6.6)$$

The fields b, b' are KK decomposed as

$$\begin{aligned} b_{L,R}(x, \phi) &= \sum_n f_n^{L,R}(\phi) b_{L,R}^{(n)}(x) \\ b'_R(x, \phi) &= \sum_{n \neq 0} f_n'^R(\phi) b_R'^{(n)}(x). \end{aligned} \quad (2.6.7)$$

The 5-d profiles $f_n(\phi), f_n'(\phi)$ are given for example in Ref. [97]. We call $b_{L,R}^0$ as $b_{L,R}, b_L^{(1)}$ as b'_L and $b_R^{(1)}$ as b'_R . Since the modes with $n > 1$ are heavier than the $n = 1$ mode by at least $\mathcal{O}(\text{TeV})$, their contributions to the processes at the electroweak scale are suppressed (compared to the $n = 1$ mode). Therefore we ignore the $n > 1$ modes from now on. Integrating over ϕ the 4-d mass terms for the fermions can be written as

$$-\mathcal{L}^{mass} \supset M_b \bar{b}_L b_R + M_{bb'} \bar{b}_L b'_R + M_{b'} \bar{b}'_L b'_R \quad (2.6.8)$$

where $M_b = \tilde{\lambda}_b \frac{v}{\sqrt{2}k\pi R} e^{k\pi R} f_0^L(\pi) f_0^R(\pi)$, $M_{bb'} = \tilde{\lambda}_t \frac{v}{\sqrt{2}k\pi R} e^{k\pi R} f_0^L(\pi) f_1'^R(\pi)$ and $M_{b'}$ is the

vector-like mass term for b' which is of order $ke^{-k\pi R}$. The $M_{bb'}$ term introduces $b \leftrightarrow b'$ mixing. We can define the new fields b_1, b_2 which diagonalizes the mass term and identify the lighter mass eigenstate (b_1) with the SM bottom. Because of the mixing, the charged current interactions will lead to $b_2 \rightarrow tW$ decays. The mixing also induces the decay processes $b_2 \rightarrow b_1 Z, b_1 h$ processes. Similar analysis can be done for the top sector. The LHC signatures of the VLFs in this model are studied in Refs. [116, 118].

As we see, many BSM theories introduce additional neutral scalars and VLFs. In order to test such theories, one needs to study the phenomenology of these new particles in detail. In the next chapter we will present a model independent study of general BSM neutral scalars. In Chapters 4, 6, 7 and 8 we will study the phenomenology of several effective models of BSM neutral scalars with VLFs also present.

Chapter 3

Model independent analysis of BSM neutral scalars

This chapter is based on the work done in Ref. [9]. As mentioned in the introduction, several BSM theories have additional neutral scalars. In this chapter we consider BSM neutral scalars, either CP-even or CP-odd, coupled to the SM fermions and SM gauge bosons. Our goal is to determine the 8 TeV and 14 TeV LHC production cross-sections of these scalars and the possible constraints from the 8 TeV LHC in terms of few effective parameters. We focus on these scalars produced by the gluon fusion process as it is usually the dominant production channel. Our analysis goes as follows.

We define an effective Lagrangian with couplings of the neutral scalars to SM gauge bosons and fermions (f). We denote the 125 GeV SM Higgs boson by h as usual, CP-even scalars by H , CP-odd scalars by A and collectively call them the ϕ . In models that contain two CP-even scalars, we identify the lighter one (h) as the 125 GeV scalar observed at the LHC. For the heavier states (ϕ), we show the constraints from the 8 TeV LHC, signal c.s. $\sigma \times \text{BR}$ into various SM two body final states at the 8 and 14 TeV LHC, as a function of the effective couplings and the ϕ mass (M_ϕ). Because of CP invariance, CP odd scalars couple to the gauge bosons only through higher dimensional ($d > 4$) operators. The CP-even scalars can couple to the massive gauge bosons at tree level. Showing only the new physics terms, the effective Lagrangian for any neutral scalar ϕ is

$$\begin{aligned}
\mathcal{L}_{eff} = & \frac{1}{2} \partial_\mu \phi \partial^\mu \phi - \frac{1}{2} M_\phi^2 \phi^2 - y_{\phi f_i f_i} \phi \bar{f}_i X f_i - \frac{1}{64\pi^2 M} \kappa_{\phi gg} \phi Y_{\mu\nu\sigma\tau} G^{a\sigma\tau} G^{a\mu\nu} \\
& - \frac{1}{64\pi^2 M} \kappa_{\phi ZZ} \phi Y_{\mu\nu\sigma\tau} Z^{\sigma\tau} Z^{\mu\nu} - \frac{1}{32\pi^2 M} \kappa_{\phi WW} \phi Y_{\mu\nu\sigma\tau} W^{\sigma\tau} W^{\mu\nu} \quad (3.0.1) \\
& - \frac{1}{64\pi^2 M} \kappa_{\phi\gamma\gamma} \phi Y_{\mu\nu\sigma\tau} A^{\sigma\tau} A^{\mu\nu} - \frac{1}{32\pi^2 M} \kappa_{\phi Z\gamma} \phi Y_{\mu\nu\sigma\tau} Z^{\sigma\tau} A^{\mu\nu} \\
& + y_{\phi WW} \phi W^\mu W_\mu + y_{\phi ZZ} \phi Z^\mu Z_\mu.
\end{aligned}$$

where $X = \gamma_5$, $Y_{\mu\nu\sigma\tau} = \epsilon_{\mu\nu\sigma\tau}$ for the CP-odd scalar, while $X = I$ (identity matrix), $Y_{\mu\nu\sigma\tau} = g_{\mu\sigma} g_{\nu\tau}$ for the CP-even scalar and “a” are the color indices. In any given model the effective couplings $\kappa_{\phi VV}$ will be generated by loop induced processes. For convenience we have defined the dimensionless effective couplings κ by pulling out an arbitrary mass-scale M in the effective ϕVV terms. In any given model the $\kappa_{\phi VV}$ can be obtained by calculating the relevant loop diagrams. If ϕff couplings exist, the SM fermions also contribute to the ϕVV processes and these contributions must also be included in $\kappa_{\phi VV}$. If the particles in the loop go onshell, then the ϕVV amplitude become complex. In that case the $\kappa_{\phi VV}$ should be interpreted as $|\kappa_{\phi VV}|$. Eq. (3.0.1) should be interpreted as an effective Lagrangian at a scale just above M_ϕ . In Appendix A we present the explicit expressions for $\kappa_{\phi\gamma\gamma}$ and $\kappa_{\phi gg}$ for a general scalar coupled to a set of fermions.

In terms of the effective couplings, the ϕ partial decay widths are given by

$$\begin{aligned}
\Gamma(\phi \rightarrow Z\gamma) &= \frac{1}{32\pi} \left(\frac{\kappa_{\phi Z\gamma}}{16\pi^2 M} \right)^2 M_\phi^3 (1 - r_Z)^3, \\
\Gamma(\phi \rightarrow \gamma\gamma) &= \frac{1}{64\pi} \left(\frac{\kappa_{\phi\gamma\gamma}}{16\pi^2 M} \right)^2 M_\phi^3, \\
\Gamma(\phi \rightarrow gg) &= \frac{1}{8\pi} \left(\frac{\kappa_{\phi gg}}{16\pi^2 M} \right)^2 M_\phi^3, \\
\Gamma(\phi \rightarrow ff) &= \frac{N_c}{8\pi} y_{\phi ff}^2 M_\phi (1 - 4r_f)^{n/2}, \quad (3.0.2)
\end{aligned}$$

where $n = 3/2$ for CP-even scalars and $1/2$ for CP-odd scalars, and $r_f = m_f^2/M_\phi^2$. We have included a color factor of 8 for $\Gamma(\phi \rightarrow gg)$. However, it turns out that the actual color factor

is only 2. To compensate for this we have included an extra factor of 2 in the expression of $\kappa_{\phi\gamma\gamma}$ in Eq. (A.0.4). From the expressions of $\Gamma(\phi \rightarrow VV)$ (in Eq. (3.0.2)) and $\kappa_{\phi VV}$ (in Eqs. (A.0.4), (A.0.7)), we can see that when calculated for a particular model, the “ M ” cancels out from the expressions of the $\phi \rightarrow gg$ and $\gamma\gamma$ decay widths. Here we present our results for $M = 1$ TeV. But if one wishes to choose some other scale, say M' then our results for the $\kappa_{\phi gg}$ have to be multiplied by M'/M .

3.1 8 TeV LHC constraints and 14 TeV LHC cross section

In this section we discuss the 8 and 14 TeV LHC $\sigma(gg \rightarrow \phi)$ and the constraints on y, κ from the 8 TeV LHC results. The currently relevant decay channels at the 8 TeV LHC are $\phi \rightarrow \gamma\gamma, tt, \tau\tau$ (collectively called XX). The 8 TeV LHC results put a certain upper limit (UL) on each $\sigma(pp \rightarrow \phi \rightarrow XX)$ using which we can put constraints on κ and y . We take the upper limit on $\sigma(pp \rightarrow \phi \rightarrow \gamma\gamma)$ from the CMS analysis in Ref. [8] which puts constraints up to $M_\phi = 850$ GeV, on $\sigma(pp \rightarrow \phi \rightarrow \tau\tau)$ from the ATLAS analysis in Ref. [7] which puts constraints up to $M_\phi = 1000$ GeV, and on $\sigma(pp \rightarrow \phi \rightarrow tt)$ from the ATLAS analysis in Ref. [6].

As mentioned earlier we will focus on the ϕ being produced through the gluon fusion. However, if the ϕ couple to the b , other production mechanisms such as $b\bar{b} \rightarrow \phi$, $bg \rightarrow b\phi$ and $gg \rightarrow b\bar{b}\phi$ are possible. The relative importance of these processes compared to the gluon fusion process depends on the $bb\phi$ coupling which is model dependent. For example, if the $bb\phi$ coupling is ≈ 0.5 then the total contribution of the bottom fusion process and b -associated processes becomes comparable to the gluon fusion process for $\kappa_{\phi gg} \approx 20$. In such scenarios the b -fusion process and the b -associated processes have to be included in $\sigma(pp \rightarrow \phi)$. We do not include these in our analysis and focus only on the gluon fusion process. The b quark associated production channels of the h including $gg \rightarrow b\bar{b}h$ is studied for example in Ref. [119]. The b quark associated production channels can be studied separately by tagging on the final state b -jet as discussed in Ref. [7]. For a recent study of $b\bar{b}$ fusion and b quark associated production channels for a light CP-odd scalar see Ref. [120].

We obtain $\sigma(gg \rightarrow \phi)$ for any M_ϕ by relating it to the corresponding cross section for the SM Higgs (ϕ_{SM}) via the relation

$$\sigma(gg \rightarrow \phi) = \sigma(gg \rightarrow \phi_{SM}) \times \frac{\Gamma(\phi \rightarrow gg)}{\Gamma(\phi_{SM} \rightarrow gg)}. \quad (3.1.1)$$

The $\sigma(gg \rightarrow \phi \rightarrow XX)$ becomes

$$\sigma(gg \rightarrow \phi \rightarrow XX) = \sigma(gg \rightarrow \phi_{SM}) \times \frac{\kappa_{\phi gg}^2}{\kappa_{\phi_{SM} gg}^2} \times BR(\phi \rightarrow XX). \quad (3.1.2)$$

The $\sigma(gg \rightarrow \phi_{SM})$ can be obtained from Ref. [32] and $\kappa_{\phi_{SM} gg}$ can be calculated in SM using Eq. (A.0.7). Here we assume that the gluon PDFs involved for A, H and h are similar. If more than one scalar have masses close to each other so that they are inseparable within the experimental resolution, then contributions from all of them should be included in Eq. (3.1.2).

In Fig. 3.1.1 we plot $\sigma(gg \rightarrow \phi)$ as a function of $\kappa_{\phi gg}$ at the 8 TeV LHC and 14 TeV LHC, for $M_\phi = 200, 500, 800$ and 1000 GeV. In any given model one can calculate the $\kappa_{\phi gg}$ and obtain $\sigma(gg \rightarrow \phi)$ from Fig. 3.1.1. To discuss the constraints from the 8 TeV LHC results, we assume the narrow width approximation $\sigma(gg \rightarrow \phi \rightarrow XX) = \sigma(gg \rightarrow \phi) \times BR(\phi \rightarrow XX)$. Using the 8 TeV LHC upper limit on any given channel (XX) we can put an upper limit on $\sigma(gg \rightarrow \phi)$ for a given $BR(\phi \rightarrow XX)$, and using Eq. (3.1.1) we can translate this to an upper limit on $\kappa_{\phi gg}$. In Fig. 3.1.2 we show the constraints on $\kappa_{\phi gg}$ and $BR(\phi \rightarrow \gamma\gamma, \tau\tau, tt)$ at 95% confidence level from the 8 TeV LHC $\gamma\gamma, \tau\tau$ and tt channel results respectively. The regions above the curves are excluded at 95% confidence level. For the $\gamma\gamma$ channel the constraint is strongest for $M_\phi = 200$ GeV where the 8 TeV LHC exclusion limit is strongest. There are no constraints on $\kappa_{\phi gg}$ for $BR(\phi \rightarrow \gamma\gamma) \lesssim 10^{-4}$. In the $\tau\tau$ channel the constraint is tightest for $M_\phi = 500$ GeV for which $\kappa_{\phi gg} \gtrsim 3$ is excluded for $BR(\phi \rightarrow \tau\tau) \approx 1$. For the tt channel we see that $\kappa_{\phi gg} \gtrsim 20$ is excluded for $BR(\phi \rightarrow tt) \approx 1$. We see that in general, the constraints coming from the $\tau\tau$ channel is strongest. In Fig. 3.1.3 we plot contours of $\sigma(gg \rightarrow \phi \rightarrow \gamma\gamma, \tau\tau, tt)$ as a function of $\kappa_{\phi gg}$ and the corresponding BRs, using Eq. (3.1.2).

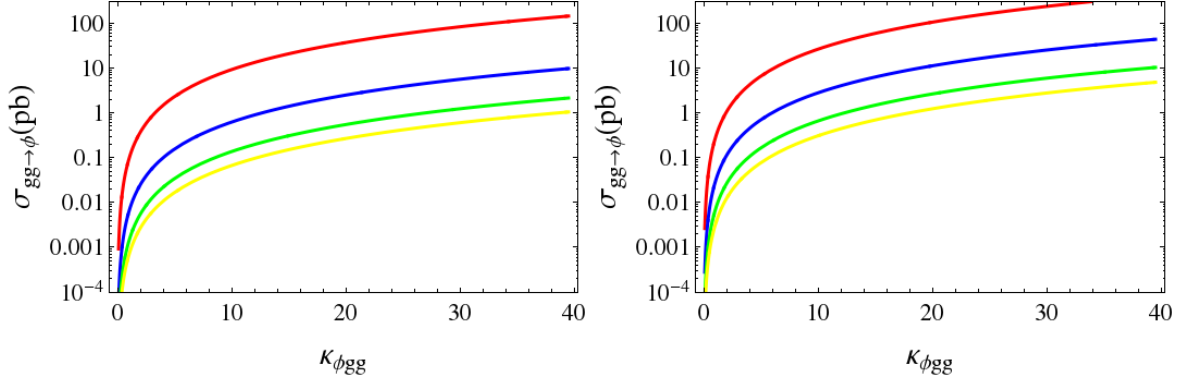


Figure 3.1.1: $\sigma(gg \rightarrow \phi)$ (in pb) at the 8 TeV LHC (left) and 14 TeV LHC (right) for $m_\phi = 200$ GeV (red), 500 GeV (blue), 800 GeV (green) and 1000 GeV (yellow)

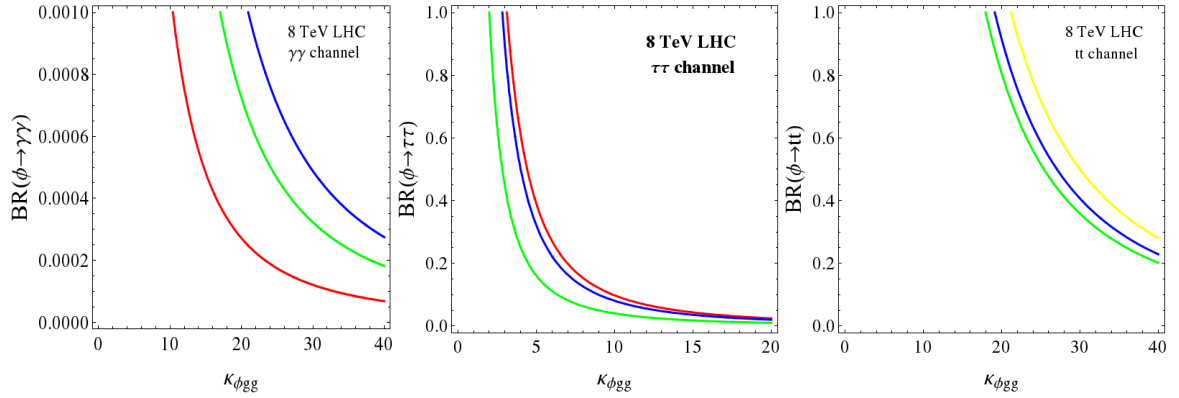


Figure 3.1.2: 8 TeV LHC constraints from the $\gamma\gamma$ channel (left), $\tau^+\tau^-$ channel (middle) and $t\bar{t}$ channel (right), for $m_\phi = 200$ GeV (red), 500 GeV (green), 800 GeV (blue) and 1000 GeV (yellow). The regions to the top and right of the curves are excluded at the 95 % CL level.

We also show in Fig. 3.1.3 the 8 TeV LHC constraints on $\kappa_{\phi gg}$ and $BR(\phi \rightarrow XX)$ by the solid curves denoted by “8 TeV”.

If the ϕ couples to the SM gauge bosons W, Z then the constraints from the $\phi \rightarrow WW, ZZ$ decays can also become important. In this thesis we will focus on scenarios where the ϕWW and ϕZZ couplings are small. In Chapter 6 and 7 we will work in the so called “2HDM alignment limit” where the tree level ϕWW and ϕZZ couplings are identically zero. In Chapter 7 and 9 we will analyze a model where the ϕ is a SM gauge singlet. There, the $\phi WW, \phi ZZ$ couplings are generated via the $\phi - h$ mixing. We will see in Chapter 9, Sec. 9.2 that the 8 TeV LHC $\phi \rightarrow hh$ results [11] constrain the mixing angle to be very small (see for example Fig. 9.2.2), and hence the ϕVV couplings are also small. Therefore, we do not analyze the constraints coming from the $\phi \rightarrow ZZ, WW$ channels.

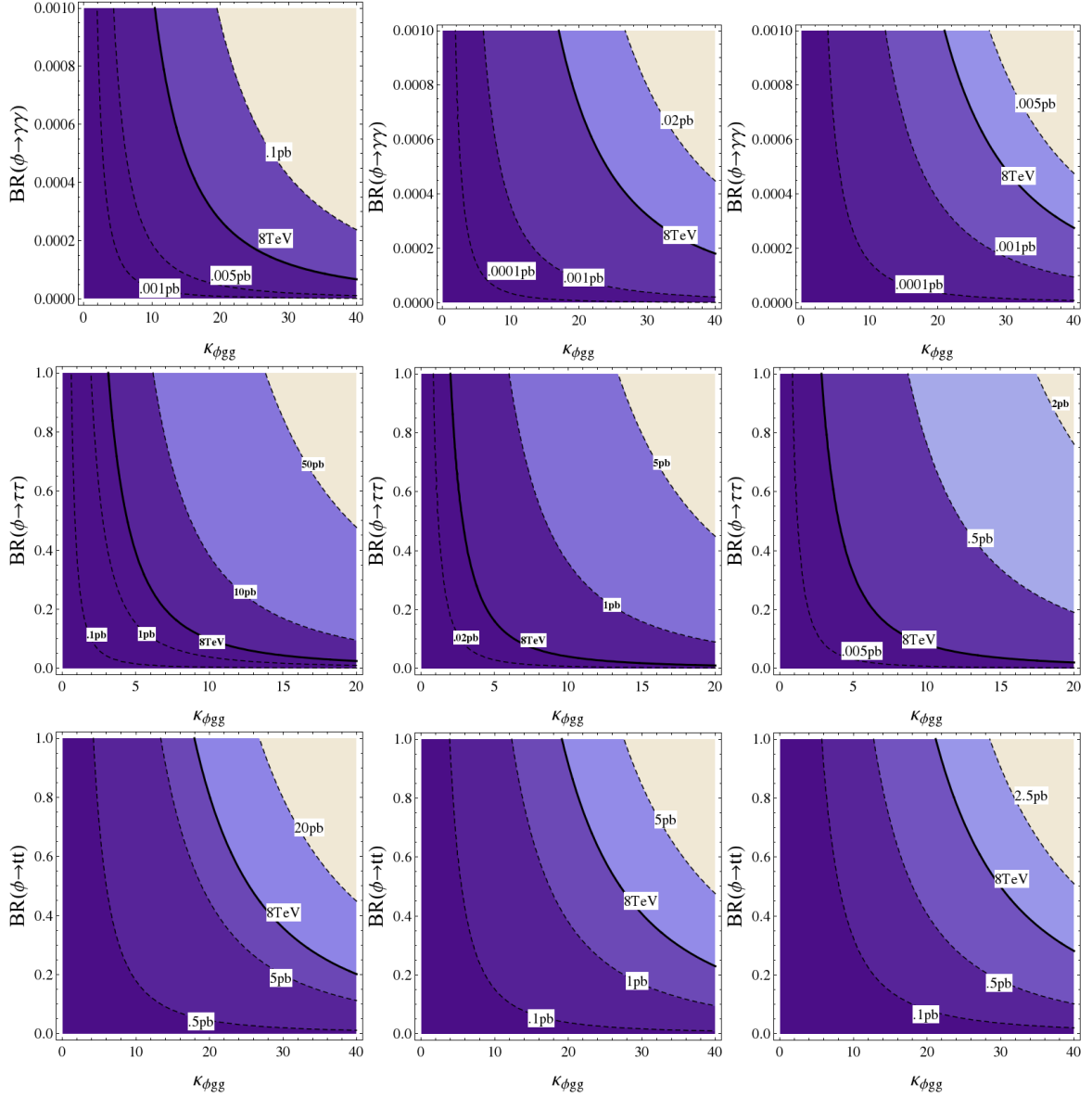


Figure 3.1.3: Contours of the 14 TeV LHC $\sigma \times BR$ (in pb) in the $\gamma\gamma$ channel (upper-row) and the $\tau^+\tau^+$ channel (middle-row) for $m_\phi = 200$ GeV (left), 500 GeV (middle), 800 GeV (right), and in the $t\bar{t}$ channel (bottom-row) for $m_\phi = 500$ GeV (left), 800 GeV (middle), 1000 GeV (right). The region above the contour labeled '8 TeV' is excluded at the 95% CL level from the 8 TeV LHC result.

As mentioned earlier, in any given model one can calculate the $\kappa_{\phi gg}$ and $BR(\phi \rightarrow XX)$ to obtain constraints on the model parameters and the LHC cross sections at 8 and 14 TeV. In later chapters we will present $\kappa_{\phi gg}$ and $BR(\phi \rightarrow XX)$ for some specific models.

Chapter 4

Phenomenology of a singlet CP-odd scalar model with vector-like fermions

This chapter is based on our work done in Ref. [9]. In many BSM theories such as the little-Higgs models [121], technicolor models [122, 123, 124], the Higgs (h) is accompanied by an $SU(2)$ singlet CP-odd scalar. These models have a bigger symmetry group than the SM and contain new vector-like fermions which together with the SM fermions complete the representation under the symmetry group. In this chapter we study few effective theories of neutral $SU(2)$ singlet CP-odd scalars with vector-like fermions also present, without specializing to any particular model. Study of such effective theories is useful to look for the CP-odd scalars without paying attention to any particular model. Specifically, we consider two models where the CP-odd scalar is coupled to either an $SU(2)$ singlet or an $SU(2)$ doublet vector-like quarks. We present the branching ratios of A and the effective Agg couplings in each of these models. We also obtain the constraints on the parameter space from the $h \rightarrow \gamma\gamma$ signal strength.

4.1 SVU model

In what we call *SVU* model an $SU(2)$ singlet CP-odd scalar A is coupled to an $SU(2)$ singlet, $SU(3)_c$ triplet VLQ (ψ) with hypercharge Y_ψ . Clearly, the electromagnetic charge

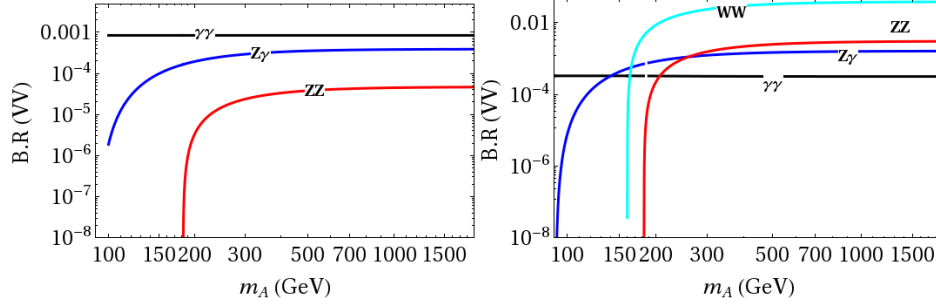


Figure 4.1.1: BR ($A \rightarrow \gamma\gamma$) (black), BR ($A \rightarrow \gamma Z$) (blue), BR($A \rightarrow ZZ$) (red), BR($A \rightarrow WW$) (cyan) as a function of m_A with $y_A = 0.1$ and $m_\psi = 1000$ GeV for SVU (left) and SVQ (right) models.

$Q = Y_\psi$. To the SM Lagrangian we add

$$\begin{aligned} \mathcal{L} \supset & \frac{1}{2} \partial_\mu A \partial^\mu A - \frac{1}{2} m_A^2 A^2 + \bar{\psi} i \not{\partial} \psi + eQ A_\mu \bar{\psi} \gamma^\mu \psi - gQ \frac{s_W^2}{c_W} Z_\mu \bar{\psi} \gamma^\mu \psi \\ & + \bar{\psi} i \not{D} \psi - i y_A A \bar{\psi} \gamma_5 \psi - m_\psi \bar{\psi} \psi - \frac{\lambda_A}{6} A^2 H^\dagger H \end{aligned} \quad (4.1.1)$$

The SM Higgs doublet is written as H here. Here we have not considered possible terms coupling the A to a SM fermion and a VLF for $Y_\psi = 2/3, -1/3$ such as $\bar{\psi}_L A u_R$, $\bar{\psi}_L A d_R$, $\bar{q} H \psi_R$. We study this possibility of off-diagonal couplings between the 3rd generation SMQ and a VLQ in the context of the $SU(2)$ doublet Φ in Chapter 6.

We restrict ourselves to $m_A < 2M_{VL}$, so that A cannot decay to a VLF pair. The possible decay modes of A are to gg , $\gamma\gamma$, $Z\gamma$ and ZZ through a VLF loop, but no decay to W^+W^- . A cannot decay to a pair of SM fermions since such couplings are forbidden by gauge invariance. The effective $AV^\mu V^\nu$ couplings induced by VLFs are given in Appendix B. From these we compute the partial widths and the BR into the above modes. In Fig. 4.1.1 we plot $\text{BR}(A \rightarrow \gamma\gamma)$, $\text{BR}(A \rightarrow Z\gamma)$ and $\text{BR}(A \rightarrow ZZ)$ where we chose $Y_\psi = 2/3$ as an example. $\text{BR}(A \rightarrow gg)$ is almost constant at around 0.999.

In Fig. 4.1.2 we plot $\kappa_{A gg}/y_A$ as a function of m_A . From this, one can read-off the $\sigma(gg \rightarrow A)$ at the 8 and 14 TeV LHC from Fig. 3.1.1 in Chapter 3. The peaks in Fig. 4.1.2 are due to the VLFs going onshell, although as mentioned earlier, we do not explore its consequences in this work. In this model, the gluon-fusion c.s. of A is induced only through

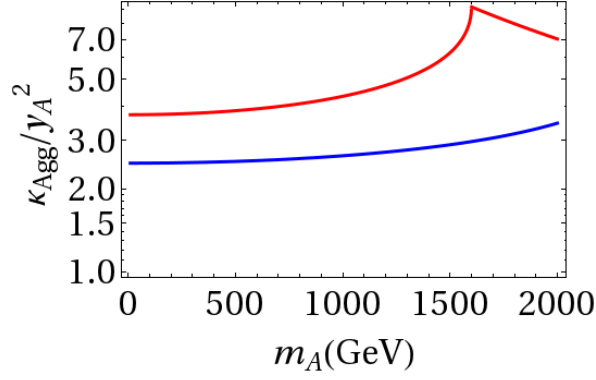


Figure 4.1.2: $\kappa_{A_{gg}}/y_A^2$ as a function of m_A for $m_\psi = 800$ GeV (red) and 1200 GeV (blue) for *SVU* model.

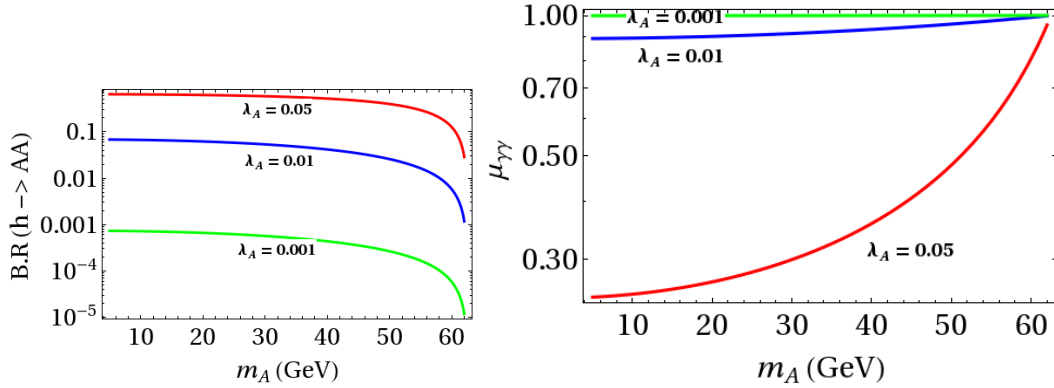


Figure 4.1.3: BR ($h \rightarrow AA$) (left) and $\mu_{\gamma\gamma}$ (right) as a function of m_A for *SVU* model.

loops of the heavy VLFs due to which the 8 TeV LHC exclusion limits on $\sigma \times BR$ into the ZZ channel (see Ref. [125]) or the $\gamma\gamma$ channel (see Ref. [8]) are rather weak, unless y_A becomes so large that perturbativity is lost.

If $m_A < m_h/2$ (where h is the 125 GeV Higgs), then $h \rightarrow AA$ becomes kinematically allowed and becomes a means of producing A in addition to the gluon-fusion channel discussed above. In Fig. 4.1.3 we plot BR($h \rightarrow AA$) for $\lambda_A = 0.1, 0.05$ and 0.001. When this decay is allowed, it will contribute to the Higgs total width thereby modifying the BRs into the other channels. In particular, it will modify the signal strength $\mu_{\gamma\gamma} = \Gamma(h \rightarrow \gamma\gamma)/\Gamma_{SM}(h \rightarrow \gamma\gamma)$, which is measured to about 10% precision (see for example Ref. [126]). We thus see that the constraint on λ_A from the 8 TeV LHC is of the order of 0.01 if $m_A < m_h/2$.

4.2 SVQ model

We consider a BSM extension, which we call the *SVQ* model, with an $SU(2)$ singlet A , and one $SU(2)$ doublet vector-like fermion $\psi = \psi_{L,R} = (\psi_{1L,R}, \psi_{2L,R})^T$ with hypercharge Y_ψ . To the SM Lagrangian we add

$$\mathcal{L} \supset \frac{1}{2} \partial_\mu A \partial^\mu A - \frac{1}{2} m_A^2 A^2 + \bar{\psi} i \not{D} \psi - i y_A A \bar{\psi} \gamma_5 \psi - m_\psi \bar{\psi} \psi - \frac{\lambda_1}{4!} A^4 - \frac{\lambda_A}{6} A^2 H^\dagger H \quad (4.2.1)$$

where the gauge interactions of the ψ are understood and are not explicitly shown. For $Y_\psi = 1/6$ one can add the terms $y'_u \bar{\psi}_L \tilde{H} u_R + y'_d \bar{\psi}_L H d_R + i y_{2A} A \bar{q}_L \psi_R + h.c$ which we will not consider here but later in Chapter 6. As in the *SVU* model, there are no decays to a pair of SM fermions, but unlike there, in this model $A \rightarrow W^+ W^-$ decay is also possible through the VLF loop, in addition to gg , $\gamma\gamma$, $Z\gamma$ and ZZ modes. The expressions for the effective couplings of the A to two SM gauge-bosons are given in Appendix B. We take $Y_\psi = 1/6$ as an example.

In Fig. 4.1.1 we plot the *BR* of A into $\gamma\gamma$, $Z\gamma$, ZZ and $W^+ W^-$ modes. As in *SVU* model, the *BR* into gg remains almost constant at around 0.99 for $m_A \gtrsim 300$ GeV. As the $\psi_1 \psi_2 W$ coupling (g) is greater than the $\psi_i \psi_i Z$ couplings $(g/c_W)(T_3 - Qs_W^2)$, the *BR* into WW is larger than into ZZ . Again, for the same reasons explained in the *SVU* model, the exclusion limits from the 8 TeV LHC in the $\gamma\gamma, ZZ, WW$ channels are rather weak in this model also.

The $\sigma(gg \rightarrow A)$ in this model is twice of what was obtained in the *SVU* model because there are two degenerate VLFs in the loop. The VLFs are degenerate since no Yukawa terms involving the SM Higgs can be written down that can split the masses after EWSB. Since no couplings to a pair of SM fermions exist, there are no b -quark initiated production processes possible.

Chapter 5

Two Higgs doublet Model type-I, II, X

In this chapter we briefly review the two Higgs doublet model (2HDM) which will be relevant in the next chapter. For a detailed review of 2HDM see Ref. [127]. 2HDM is a simple extension of the standard model (SM) which extends the scalar sector of the SM. Specifically, one introduces two SU(2) doublet scalars Φ_1 and Φ_2 with hypercharge Y_{Φ_1} and Y_{Φ_2} respectively, along with a potential term $V(\Phi_1, \Phi_2)$ for the Φ_1 and Φ_2 . To obtain the vacuum of the theory, one then minimizes $V(\Phi_1, \Phi_2)$ with respect to Φ_1 and Φ_2 . The ratio

$$\rho = \frac{(g_Z^2/M_Z^2)}{(g^2/M_W^2)} \quad (5.0.1)$$

is very precisely measured and found to be very close to 1. In general, for n SU(2) doublet scalars Φ_i with hypercharge Y_{Φ_i} and v.e.v. $\langle \Phi_i \rangle = v_i$ we have [127]

$$\rho = \frac{\sum_i \left(\frac{3}{4} - Y_{\Phi_i}^2 \right) v_i}{\sum_i 2Y_{\Phi_i}^2 v_i}. \quad (5.0.2)$$

We see that if we want $\rho = 1$, we must take $Y_{\Phi_i} = \pm 1/2$. We take $Y_{\Phi_1} = Y_{\Phi_2} = 1/2$ which is usually considered in the literature. Considering only the renormalizable terms we can write

the general 2HDM scalar potential as

$$\begin{aligned}
V(\Phi_1, \Phi_2) = & m_{11}^2 \Phi_1^\dagger \Phi_1 + m_{22}^2 \Phi_2^\dagger \Phi_2 - (m_{12}^2 \Phi_1^\dagger \Phi_2 + h.c.) + \lambda_1 (\Phi_1^\dagger \Phi_1)^2 + \lambda_2 (\Phi_2^\dagger \Phi_2)^2 \\
& + \lambda_3 \Phi_1^\dagger \Phi_1 \Phi_2^\dagger \Phi_2 + \lambda_4 \Phi_1^\dagger \Phi_2 \Phi_2^\dagger \Phi_1 + \frac{\lambda_5}{2} [(\Phi_1^\dagger \Phi_2)^2 + h.c.] + \lambda_6 \Phi_1^\dagger \Phi_1 \Phi_1^\dagger \Phi_2 \\
& + \lambda_7 \Phi_2^\dagger \Phi_2 \Phi_1^\dagger \Phi_2.
\end{aligned} \tag{5.0.3}$$

If $m_{12}^2 = \lambda_6 = \lambda_7 = 0$, then the theory has an exact discrete Z_2 symmetry under which $\Phi_1 \rightarrow -\Phi_1, \Phi_2 \rightarrow \Phi_2$. As we will see later, this Z_2 symmetry forbids tree level flavor changing neutral currents (FCNC). We will set $\lambda_6 = \lambda_7 = 0$ from now on but keep a nonzero m_{12}^2 . The m_{12}^2 term breaks the Z_2 symmetry *softly* and does not give rise to tree level FCNCs. The reason for choosing a nonzero m_{12}^2 will be clear later. The λ_i in general can be complex, in which case they contribute to CP violation. We are not interested in studying CP violation in the scalar sector and therefore we choose the λ_i to be real.

Minimizing the $V(\Phi_1, \Phi_2)$ with respect to Φ_1 and Φ_2 gives the V.E.Vs $\langle \Phi_i \rangle = (1/\sqrt{2})(0, v_i)^T$ which satisfies the conditions

$$\begin{aligned}
m_{11}^2 - m_{12}^2 \frac{v_2}{v_1} + \lambda_1 v_1^2 + \frac{1}{2}(\lambda_3 + \lambda_4 + \lambda_4)v_2^2 &= 0 \\
m_{22}^2 - m_{12}^2 \frac{v_1}{v_2} + \lambda_2 v_2^2 + \frac{1}{2}(\lambda_3 + \lambda_4 + \lambda_4)v_1^2 &= 0.
\end{aligned} \tag{5.0.4}$$

The EW vacuum (v) is given by $v = \sqrt{v_1^2 + v_2^2}$. It is useful to define the parameter $\tan \beta = v_2/v_1$. The fluctuations of Φ_i around the V.E.Vs can be parametrized as

$$\Phi_i = \begin{pmatrix} \Phi_i^+ \\ \frac{1}{\sqrt{2}}(v_i + \rho_i + i\eta_i) \end{pmatrix}. \tag{5.0.5}$$

Using Eq. (5.0.4) the mass matrix for the CP-even scalar sector (ρ_1, ρ_2) is given by

$$M_1^2 = \begin{pmatrix} 2\lambda_1 v_1^2 + m_{12}^2 \frac{v_2}{v_1} & -m_{12}^2 + \lambda_{345} v_1 v_2 \\ -m_{12}^2 + \lambda_{345} v_1 v_2 & 2\lambda_2 v_1^2 + m_{12}^2 \frac{v_1}{v_2} \end{pmatrix}. \tag{5.0.6}$$

The M_1^2 can be diagonalized by the orthogonal rotation

$$\begin{pmatrix} H \\ h \end{pmatrix} = \begin{pmatrix} \cos \alpha & \sin \alpha \\ -\sin \alpha & \cos \alpha \end{pmatrix} \begin{pmatrix} \rho_1 \\ \rho_2 \end{pmatrix} \quad (5.0.7)$$

with the mixing angle α given by

$$\tan 2\alpha = \frac{2C}{A - B} \quad (5.0.8)$$

with $C = -m_{12}^2 + \lambda_{345} v_1 v_2$, $A = 2\lambda_1 v_1^2 + m_{12}^2 \frac{v_2}{v_1}$, $B = 2\lambda_2 v_1^2 + m_{12}^2 \frac{v_1}{v_2}$. The mass eigenvalues are given by

$$m_{h,H}^2 = \frac{1}{2} \left(A + B \mp \sqrt{(A - B)^2 + 4C^2} \right). \quad (5.0.9)$$

We will identify the lighter eigenstate h with the 125 GeV Higgs boson. The mass matrix for the CP-odd sector (η_1, η_2) is given by

$$M_2^2 = \begin{pmatrix} -\lambda_5 v_1^2 + m_{12}^2 \frac{v_2}{v_1} & -m_{12}^2 + \lambda_{345} v_1 v_2 \\ -m_{12}^2 + \lambda_{345} v_1 v_2 & -\lambda_5 v_2^2 + m_{12}^2 \frac{v_1}{v_2} \end{pmatrix} \quad (5.0.10)$$

which can be diagonalized via the orthogonal rotation

$$\begin{pmatrix} G^0 \\ A \end{pmatrix} = \begin{pmatrix} \cos \beta & \sin \beta \\ -\sin \beta & \cos \beta \end{pmatrix} \begin{pmatrix} \eta_1 \\ \eta_2 \end{pmatrix}. \quad (5.0.11)$$

where G^0 is a Goldstone boson which will be eventually eaten by the SM Z boson. The mass (m_A) of the physical eigenstate A is given by

$$m_A^2 = m_{12}^2 \frac{v^2}{v_1 v_2} - \lambda_5 v^2. \quad (5.0.12)$$

The mass matrix for the charged sector is

$$M_3^2 = \begin{pmatrix} m_{11}^2 + \lambda_1 v_1^2 + \frac{1}{2} \lambda_3 v_2^2 & -m_{12}^2 + \frac{1}{2} (\lambda_4 + \lambda_5) v_1 v_2 \\ -m_{12}^2 + \frac{1}{2} (\lambda_4 + \lambda_5) v_1 v_2 & m_{22}^2 + \lambda_2 v_1^2 + \frac{1}{2} \lambda_3 v_1^2 \end{pmatrix} \quad (5.0.13)$$

which can be diagonalized by the orthogonal rotation

$$\begin{pmatrix} G^\pm \\ H^\pm \end{pmatrix} = \begin{pmatrix} \cos \beta & \sin \beta \\ -\sin \beta & \cos \beta \end{pmatrix} \begin{pmatrix} \Phi_1^\pm \\ \Phi_2^\pm \end{pmatrix} \quad (5.0.14)$$

where G^\pm are the Goldstone bosons which will be eaten by the SM W^\pm bosons. Using Eq. (5.0.4), the charged Higgs mass is given by

$$m_{H^\pm}^2 = \frac{m_{12}^2 v^2}{v_1 v_2} - \frac{1}{2} (\lambda_4 + \lambda_5) v^2. \quad (5.0.15)$$

From Eq. (5.0.6) we have

$$m_H^2 + m_h^2 = 2\lambda_1 v_1^2 + 2\lambda_2 v_2^2 + m_{12}^2 \frac{v^2}{v_1 v_2}. \quad (5.0.16)$$

For a 2HDM with exact Z_2 symmetry ($m_{12}^2 = 0$) Eq. 5.0.16 gives

$$\lambda_1 v_1^2 = \frac{1}{2} (m_H^2 + m_h^2) - \lambda_2 v_2^2. \quad (5.0.17)$$

It follows from Eq. 5.0.17 that λ_1 has an upper bound given by

$$\lambda_1 v^2 \cos^2 \beta \geq \frac{1}{2} (m_H^2 + m_h^2) \quad (5.0.18)$$

since $\lambda_2 \geq 0$ (required for the stability of the vacuum). Since $m_H > m_h$ the upper bound on λ_1 is given by

$$\begin{aligned} \lambda_1 &> \frac{m_h^2}{v^2} (1 + \tan^2 \beta) \\ &\approx 0.25 (1 + \tan^2 \beta). \end{aligned} \quad (5.0.19)$$

We see from Eq. (5.0.19) that for large $\tan \beta$, λ_1 will become nonperturbative. If we require the λ_1 to be perturbative, i.e $\lambda_1 < 4\pi$, then we have the upper bound on $\tan \beta$ as $\tan \beta \lesssim 7$ (for $m_{12}^2 = 0$). This is the same result obtained in Ref. [70]. We will always work with a non-zero m_{12}^2 so that we can explore higher values of $\tan \beta$. In total, there are eight free parameters in the 2HDM scalar potential. After fixing $v = 246$ GeV, we are left with seven free parameters which we take to be $\alpha, \tan \beta, m_{12}^2$ and the physical mass parameters m_h, m_A, m_H, m_{H^\pm} .

The gauge couplings ($g_{\phi VV}$) of the h, H with the SM gauge bosons (VV) can be obtained from the the gauge terms

$$\mathcal{L} = (D_\mu \Phi_1)^2 + (D_\mu \Phi_2)^2 \quad (5.0.20)$$

with $D_\mu = \partial_\mu - ig/\sqrt{2}(W_\mu^+ T^+ + W_\mu^- T^-) - i(g/2 \cos \theta_W) Z_\mu$. Substituting Eq. (5.0.5) in Eq. , the terms involving ρ_i, η_i, v_i can be written as

$$\begin{aligned} \mathcal{L} \supset & \frac{g^2}{2}(v_1 \rho_1 + v_2 \rho_2) W^{+\mu} W_\mu^- + \frac{g^2}{4 \cos^2 \theta_W} (v_1 \rho_1 + v_2 \rho_2) Z_\mu Z^\mu + \frac{g^2}{4} (\eta_1^2 + \eta_2^2) W^{+\mu} W_\mu^- \\ & + \frac{g^2}{8 \cos^2 \theta_W} (\eta_1^2 + \eta_2^2) Z^\mu Z_\mu + \frac{g^2}{4} (v_1^2 + v_2^2) W^{+\mu} W_\mu^- + \frac{g^2}{8} (v_1^2 + v_2^2) Z_\mu Z^\mu \end{aligned} \quad (5.0.21)$$

Using Eq. (5.0.7) the terms involving the physical states A, H, h can be written as

$$\begin{aligned} \mathcal{L} = & \frac{g^2}{2} v \cos(\beta - \alpha) H W W_\mu^- + \frac{g^2}{2} v \sin(\beta - \alpha) h W^{+\mu} W_\mu^- + \frac{g^2}{4 \cos^2 \theta_W} v \cos(\beta - \alpha) H Z^\mu Z_\mu \\ & + \frac{g^2}{2 \cos^2 \theta_W} v \sin(\beta - \alpha) h Z^\mu Z_\mu + \frac{g^2}{4} A^2 W^{+\mu} W_\mu^- + \frac{g^2}{8 \cos^2 \theta_W} A^2 Z^\mu Z_\mu + \frac{g^2}{4} v^2 W^{+\mu} W_\mu^- \\ & + \frac{g^2}{8 \cos^2 \theta_W} v^2 Z^\mu Z_\mu \end{aligned} \quad (5.0.22)$$

From Eq. (5.0.7) we can read of the hVV and HVV gauge couplings ($g_{\phi VV}$) as

$$\begin{aligned}
g_{hWW} &= \sin(\beta - \alpha) \frac{g^2 v}{2}, \\
g_{HWW} &= \cos(\beta - \alpha) \frac{g^2 v}{2}, \\
g_{hZZ} &= \sin(\beta - \alpha) \frac{g^2 v}{2 \cos^2 \theta_W}, \\
g_{HZZ} &= \cos(\beta - \alpha) \frac{g^2 v}{2 \cos^2 \theta_W}.
\end{aligned} \tag{5.0.23}$$

The tree level AVV couplings are zero, as expected from CP invariance. We see that for $\beta - \alpha = \pi/2$, the g_{hVV} couplings become identical to that of the SM Higgs. Therefore, the limit $\beta - \alpha = \pi/2$ is called the 2HDM ‘‘alignment limit’’. We also see that the g_{HVV} couplings become zero in the alignment limit.

5.1 The Yukawa couplings

In the absence of any additional symmetries (apart from the EW gauge symmetry), the SM fermions will have Yukawa couplings with both the Φ_1 and Φ_2 . For example the most general Yukawa term involving the charge $-1/3$ SM fermions (d_j) can be written as

$$\mathcal{L}^{Yuk} = y_{ij}^1 \bar{q}_{iL} \Phi_1 d_{jR} + y_{ij}^2 \bar{q}_{iL} \Phi_2 d_{jR} \tag{5.1.1}$$

where q_{iL} are the SM-quark SU(2) doublet. Substituting the V.E.Vs of Φ_1 and Φ_2 in Eq. (5.1.1) gives the mass terms

$$\mathcal{L}^{mass} = y_{ij}^1 \bar{d}_{Li} v_1 d_{Rj} + y_{ij}^2 \bar{d}_{Li} v_2 d_{Rj}. \tag{5.1.2}$$

In general the the \mathcal{L}^{Yuk} and \mathcal{L}^{mass} cannot be diagonalized simultaneously and there will be flavor changing neutral currents (FCNC). So a necessary condition for the absence of tree level FCNCs is that all the quarks of a given charge must have Yukawa couplings with only one Higgs doublet [128]. However to guarantee the absence of tree level FCNCs, we need a

second condition. To derive this let's consider the neutral Z current

$$J_Z^\mu = (g/\cos\theta_W) [\bar{q}_L K_L q_L + \bar{q}_R K_R q_R] \quad (5.1.3)$$

with,

$$\begin{aligned} K_L &= T_L^3 - Q \sin^2_{\theta_W} \\ K_R &= T_R^3 - Q \sin^2_{\theta_W} \end{aligned} \quad (5.1.4)$$

We diagonalize the mass terms in Eq. (5.1.2) by a bi-unitary rotations $q_L \rightarrow U_L q_L, q_R \rightarrow U_R q_R$. Under these bi-unitary rotations the K_L and K_R transform as $K_{L,R} \rightarrow U_{L,R}^\dagger K_{L,R} U_{L,R}$. From Eq. (5.1.3) we see that the conservation of flavor requires that $[U_L, K_L] = [U_R, K_R] = 0$. Also, the charge conservation requires that $[U_L, Q] = 0, [U_R, Q] = 0$. Then from Eq. (5.1.4) we arrive at the condition $[T_L^3, Q] = [T_R^3, Q] = 0$, that is all the quarks of a given charge Q and helicity must have the same T^3 . Combining this with the first condition, we conclude that the necessary and sufficient condition for the absence of tree-level FCNC is that all the quarks of a given charge must have the same T^3 for a given helicity, and should have Yukawa couplings with only one Higgs doublet [128]. In the 2HDM this condition can be enforced by imposing a Z_2 symmetry under which the 2HDM scalars and the SM fermions transform in a certain way. The Z_2 transformation of the 2HDM scalars can be taken to be $\Phi_1 \rightarrow -\Phi_1, \Phi_2 \rightarrow \Phi_2$. Whether a given SM fermion couple to Φ_1 or Φ_2 depends on its transformation property under the Z_2 . Usually three types of Yukawa structures are considered in the literature, the so called 2HDM of type-I, type-II, type-X. Below we briefly discuss each of these types .

2HDM type-I:

In 2HDM of type-I (2HDM-I) all the SM fermions are left unchanged under the Z_2 . In this case all the SM fermions couple to the Φ_2 . This Yukawa term is given by

$$\mathcal{L} \supset -y_d \bar{q}_L \Phi_2 d_R - y_u \bar{q}_L \tilde{\Phi}_2 u_R + h.c. , \quad (5.1.5)$$

where $\tilde{\Phi}_2 = i\sigma_2 \Phi_2^*$. The Yukawa couplings of h, H, A are given by

$$\mathcal{L}^{Yuk} \supset -\frac{1}{\sqrt{2}} \left(y_u h c_\alpha \bar{u}_L u_R + y_d h c_\alpha \bar{d}_L d_R + y_u c_\beta i A \bar{u}_L u_R - y_d c_\beta i A \bar{d}_L d_R + h.c. \right) \quad (5.1.6)$$

and the mass terms for the SM fermions are given by

$$\mathcal{L}^{mass} \supset -\frac{v}{\sqrt{2}} (y_d s_\beta \bar{d}_L d_R + y_u s_\beta \bar{u}_L u_R + h.c.). \quad (5.1.7)$$

The h, H and A Yukawa couplings can be written as $y_{hdd} = (m_d/v)(c_\alpha/s_\beta)$, $y_{huu} = (m_u/v)(c_\alpha/s_\beta)$, $y_{Hdd} = (m_d/v)(s_\alpha/s_\beta)$, $y_{Hu u} = (m_u/v)(s_\alpha/s_\beta)$, $y_{Add} = -(m_d/v) \cot \beta$, $y_{Auu} = (m_d/v) \cot \beta$, where $m_{d,u} = y_{d,u} s_\beta / \sqrt{2}$ and we have introduced the notation $c_\theta = \cos \theta$, $s_\theta = \sin \theta$. In the alignment limit the H and A Yukawa couplings become the same and the h Yukawa couplings become identical to that of the SM Higgs boson.

2HDM type-II:

In 2HDM type-II (2HDM-II) all the right-handed down-type SM fermions transforms under Z_2 as $d_R \rightarrow -d_R$ and the up-type fermions remain unchanged. In this case all the down-type fermions couple to Φ_1 , while all the up-type fermions couple to Φ_2 . The Yukawa term for the 2HDM-II is given by

$$\mathcal{L} \supset -y_d \bar{q}_L \Phi_1 d_R - y_u \bar{q}_L \tilde{\Phi}_2 u_R + h.c. . \quad (5.1.8)$$

The h, H, A Yukawa couplings in this case are given by $y_{hdd} = -(m_d/v)(s_\alpha/c_\beta)$, $y_{huu} = (m_u/v)(c_\alpha/s_\beta)$, $y_{Hdd} = (m_d/v)(c_\alpha/c_\beta)$, $y_{Hu u} = (m_u/v)(s_\alpha/s_\beta)$, $y_{Add} = (m_d/v) \tan \beta$, $y_{Auu} = (m_d/v) \cot \beta$, where $m_d = y_d \cos \beta / \sqrt{2}$, $m_u = y_u \sin \beta / \sqrt{2}$.

2HDM type-X:

In 2HDM type-X (2HDM-X) all the right-handed SM leptons (e) transform under Z_2 as $e_R \rightarrow -e_R$ and all other fermions remains unchanged. In this case The Yukawa term for the 2HDM-X is given by

$$\mathcal{L} \supset - (y_d \bar{q}_L \Phi_2 d_R + y_u \bar{q}_L \tilde{\Phi}_2 u_R + y_e \bar{l}_L \Phi_1 e_R + h.c). \quad (5.1.9)$$

The h, H, A Yukawa couplings in this case are given by $y_{hee} = -(m_e/v)(s_\alpha/c_\beta)$, $y_{Hee} = (m_e/v)(c_\alpha/c_\beta)$, $y_{Aee} = (m_e/v) \tan \beta$, where $m_e = y_e \cos \beta / \sqrt{2}$ for the leptons. The quark Yukawa couplings are same as in 2HDM-I.

The measurements of the Higgs signal strengths μ_{XX} at the 8 TeV LHC [81, 82] reveals that the hXX couplings are very close to that of their SM values, where $\mu_{XX} = \sigma(h) \times BR(h \rightarrow XX) / [\sigma(h) \times BR(h \rightarrow XX)]_{\text{SM}}$. For example, measurement of the μ_{WW} puts a 95% confidence level constraint on the hWW coupling (g_{hWW}) as $0.81 < g_{hWW}/g_{hWW}^{SM} < 1.01$ (Table 14 of Ref. [129]). Therefore in the 2HDM, the ‘‘alignment limit’’ ($\beta - \alpha = \pi/2$) is strongly favored (see for example Ref. [63]). Also, since in the alignment limit the tree level gauge couplings of the H, A are zero, the heavy Higgs searches [125] in the WW, ZZ channel do not put any significant constraints on the parameter space. In the chapters to follow we will always work in the alignment limit.

In the next chapter we will discuss the phenomenology of the neutral heavy scalars (H, A) in 2HDM-II, X. Then we will analyze several models where we introduce new vector-like fermion to 2HDM-II and X.

Chapter 6

Phenomenology of neutral scalars in Two Higgs doublet model with vector-like fermions

This chapter is based on the work done in Ref. [9]. As discussed in Chapter 5, the two Higgs doublet model is one of the simplest extensions of the SM, obtained by extending its scalar sector. Apart from the 125 GeV Higgs boson (h), the 2HDM has three new scalars, namely the neutral heavy scalars A, H and a heavy charged scalar H^\pm . Their phenomenology is very rich and has been studied extensively in the literature (see for example Refs. [65, 66, 67, 68, 69, 130]). It will be interesting to explore the possibility of extending the 2HDM to include new fermions. One possibility is to simply add an extra generation of chiral fermions. Such chiral fermions are strongly disfavored from experiments [24]. However, there exists the possibility where the new fermions are vector-like under $SU(2) \times U(1)_Y$. In fact there are several UV complete models [3, 4, 100, 105] which has a 2HDM structure with new vector-like fermions also present. In this chapter, we will study the phenomenology of some effective theories which has the structure of the 2HDM, and also contain VLFs. We will focus on the neutral scalars A, H . We present the branching ratios of A, H to two-body decay channels and obtain the LHC cross sections in the gluon fusion channel. We also present the constraint on the parameter space from the 8 TeV LHC $\tau\tau$ channel results.

We will first briefly discuss the phenomenology of the neutral scalars (H, A) of 2HDM-II and X with the SM fermions only. We will then study several models where we introduce vector-like fermions to the 2HDM-II and X.

6.1 2HDM with SMF only

As mentioned before, the 2HDM has two neutral heavy scalars H and A (collectively called ϕ here). The phenomenology of these neutral scalars has already been studied for example in Refs. [62, 63, 64, 76]. The 8 TeV LHC constraints on the 2HDM parameter-space are discussed for example in Refs. [71, 72, 73, 75]. Here we will briefly review some of the phenomenological aspects of H, A . We present the branching ratios of the neutral scalars and the effective ϕgg couplings. We focus on the scenario where the lightest 2HDM scalar h is identified with the 125 GeV Higgs. Ref. [60] considered the possibility that the observed 125 GeV state at the LHC is the CP-odd scalar (A), and found that this possibility is disfavored by the LHC data. The couplings of the ϕ to the SM gauge bosons and the SM fermions are given in Chapter 5. As we have mentioned in Chapter 5 we will work in the 2HDM alignment limit which is strongly favored from the measurements of the Higgs observables. For a detailed discussion of 2HDM alignment limit see [130]. We recall that in the alignment limit the tree level couplings of the H and A are similar. Also, the tree level couplings of both the H and A to the SM gauge bosons become zero in the alignment limit. In this case the couplings of the H and A to the SM gauge bosons are generated by loop level processes with SM fermions running in the loop. The effective ϕgg couplings ($\kappa_{\phi gg}$) can be obtained from the general expressions given in Appendix A using which one can obtain $\sigma(gg \rightarrow \phi)$ from Fig. 3.1.1 in Chapter 3. Production cross sections of A, H in 2HDM has been studied for example in Refs. [131, 132]. If A and H have nearly degenerate masses so that experiments cannot distinguish them, their contributions must be added in any given channel. Because of different CP properties of the A and H , their sum will be incoherent i.e. $\sigma(pp \rightarrow \phi \rightarrow XX) = \sigma(pp \rightarrow A \rightarrow XX) + \sigma(pp \rightarrow H \rightarrow XX)$. Below we present the ϕ branching ratios and $\kappa_{\phi gg}$ for 2HDM-II and 2HDM-X.

6.1.1 2HDM-II

The Lagrangian and the ϕ couplings for the 2HDM-II is given in Chapter 5. In Fig. 6.1.1 we plot the branching ratios $BR(A \rightarrow \tau\tau, bb)$ as a function of m_A for $\tan\beta = 1, 5, 10, 15, 30$ and $BR(A \rightarrow tt)$ for $\tan\beta = 1, 5, 10, 15$, in the alignment limit. We see that for $m_A < 2m_t$, the dominant decay channel is $A \rightarrow bb$ since the $A\tau\tau$ coupling ($\propto m_\tau \tan\beta$) is smaller than the $A\bar{b}b$ coupling ($\propto m_b \tan\beta$). For $m_A > 2m_t$, the $A \rightarrow tt$ channel opens up and dominates for small $\tan\beta$. However for large $\tan\beta$ the $A\bar{t}t$ coupling ($\propto \cot\beta$) is suppressed and $BR(A \rightarrow bb)$ dominates as can be seen from Fig. 6.1.1. The loop level branching ratios $BR(A \rightarrow \gamma\gamma, Z\gamma)$ are shown in Fig. 6.2.5 (by the dashed curve) in Sec. 6.2.2 where we discuss 2HDM-II with VLFs. We see that the BRs into $\gamma\gamma$ and $Z\gamma$ are smaller compared to that of the corresponding loop induced SM Higgs branching ratios even for $\tan\beta = 1$ when the couplings of A to the SM fermions are equal to the Higgs Yukawa couplings. This is because the partial width $\Gamma(h \rightarrow \gamma\gamma, \gamma Z)$, being dominated by the W loop, is larger than the partial width $\Gamma(A \rightarrow \gamma\gamma, \gamma Z)$ in which only the fermions contribute (see for example Fig. 2.10 of Ref. [133]). For larger $\tan\beta$ the branching ratios are even smaller because of the increased $\Gamma(A \rightarrow b\bar{b})$ and $\Gamma(A \rightarrow \tau^+\tau^-)$. The discontinuity at $m_A = 2m_t$ in the BRs in Fig. 6.2.5 for $\tan\beta = 1$ is because of the onset of $A \rightarrow t\bar{t}$ on-shell decay. For larger $\tan\beta$, the discontinuity is smaller since the $A\bar{t}t$ coupling becomes smaller. The $h \rightarrow AA$ decay, possible for $m_A < m_h/2$, is studied in Ref. [63] and we will not discuss it here. Since the coupling of the H to the SM fermions are same as the A in the alignment limit, the H branching ratios to the SM fermions will be quite similar to that of the A and we do not explicitly show them here.

The effective couplings $\kappa_{A\bar{g}g}$ and $\kappa_{H\bar{g}g}$ can be obtained from the general expressions given in Eq. (A.0.7) in Appendix A. In Fig. 6.1.2 we plot contours of $\kappa_{A\bar{g}g}$ and $\kappa_{H\bar{g}g}$ in the $m_A - \tan\beta$ plane. Using this one can calculate the $\sigma(\phi \rightarrow gg)$ from Fig. 3.1.1 in Chapter 3. Near $m_\phi \approx 2m_t$, $\kappa_{A\bar{g}g} \approx 2.5 \times \kappa_{H\bar{g}g}$, since $F_{1/2}^A \approx 2.5 \times F_{1/2}^H$ for $m_\phi \approx 2m_t$ (see Fig. A.0.2 in Appendix A) which explains the difference in the behavior of $\kappa_{A\bar{g}g}$ and $\kappa_{H\bar{g}g}$ near $m_A \approx 2m_t$. In 2HDM-II, the $H\bar{b}b$ coupling and $H\bar{t}t$ have a relative sign between them which results in

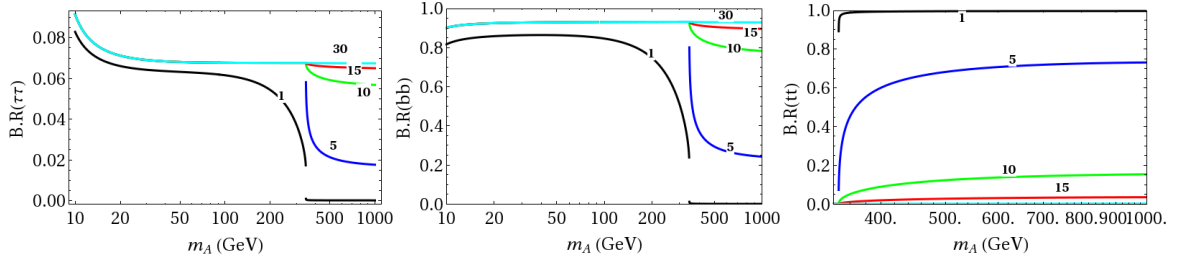


Figure 6.1.1: $BR(A \rightarrow \tau^+\tau^-, b\bar{b})$ (left, middle) for $\tan\beta = 1, 5, 10, 15, 30$ and $BR(A \rightarrow t\bar{t})$ (right) for $\tan\beta = 1, 5, 10, 15$ in 2HDM Type-II model. The loop-level $BR(A \rightarrow VV)$ in the Type-II 2HDM are shown in Fig. 6.2.5 by the dashed-black curves.

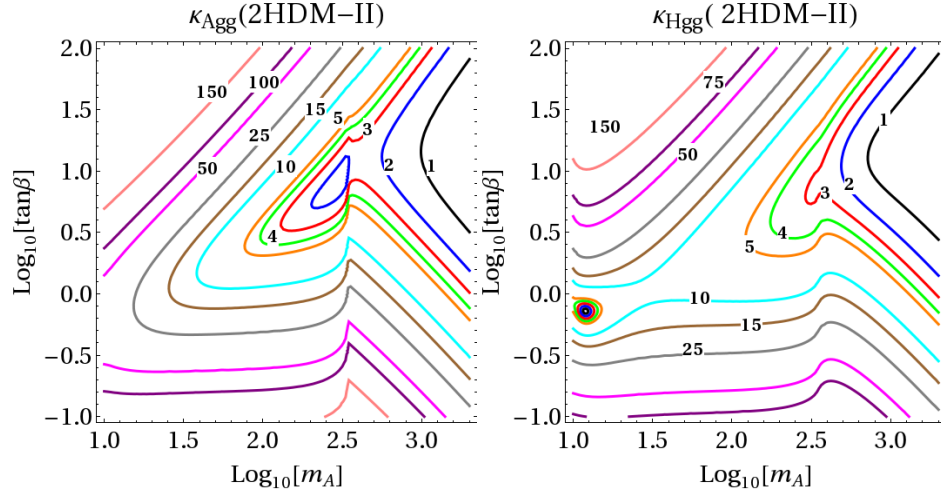


Figure 6.1.2: Contours of $\kappa_{A_{gg}}$ (left) and Contours of $\kappa_{A_{gg}}$ (left) and $\kappa_{H_{gg}}$ (right) in the Type-II 2HDM. (right) in the Type-II 2HDM..

destructive interference between the t contribution and the b contribution. For $m_A \sim 10$ GeV the cancellation becomes significant since b can go onshell at this value of m_A and can contribute significantly to $\kappa_{H_{gg}}$ which explains the behavior of $\kappa_{H_{gg}}$ near $m_H \approx 10$ GeV in Fig. 6.1.2.

We saw in Chapter 3 that the $\phi \rightarrow \tau\tau$ channel 8 TeV LHC results puts stringent constraint on $\kappa_{\phi_{gg}}$ and $BR(\phi \rightarrow \tau\tau)$. Here we present the constraints on $m_A - \tan\beta$ plane from the 8 TeV LHC $\phi \rightarrow \tau\tau$ results for the 2HDM-II. As mentioned before, if m_A and m_H are within the experimental resolution so that they cannot be separated, then both of this contributions must be added. For the $\phi \rightarrow \tau\tau$ channel the experimental invariant-mass resolution is about 30%. Therefore, we consider two cases, one when m_A and m_H are within 30% and add the contributions from the “degenerate” A and H , and another when they are split by more

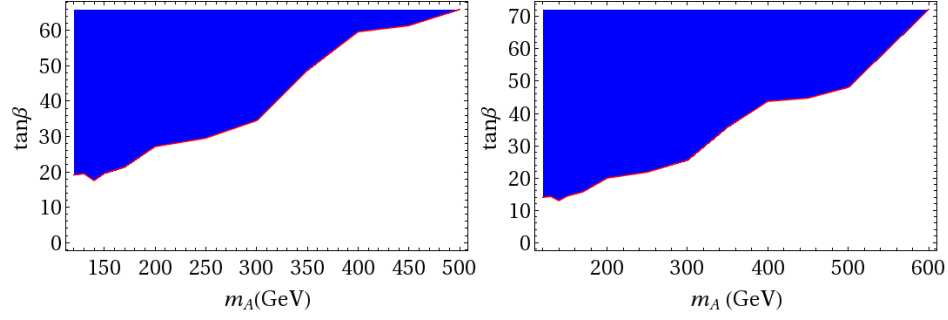


Figure 6.1.3: For Type-II 2HDM, regions of the $m_A \text{tan}\beta$ plane (blue region) which is excluded at 95% confidence level from $\phi \rightarrow \tau^+\tau^-$ decay when only A is present (left) and when m_A and m_H are degenerate (right).

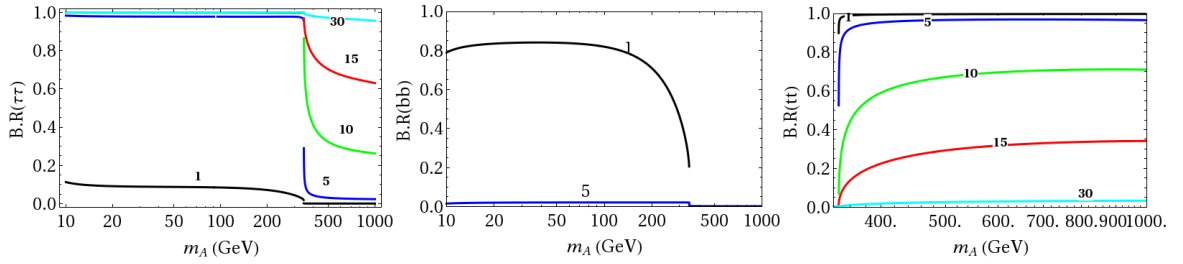


Figure 6.1.4: For the Type-X 2HDM, $BR(A \rightarrow \tau^+\tau^-, t\bar{t})$ (left, right) for $\tan\beta = 1, 5, 10, 15, 30$, and $BR(A \rightarrow b\bar{b})$ (middle) for $\tan\beta = 1, 5$. The $BR(A \rightarrow \gamma\gamma, Z\gamma)$ for the Type-X 2HDM is shown in Fig. 6.3.1 as the dashed-black curve.

than 30% and treat them separately. When they are degenerate, we have $BR(A \rightarrow \tau^+\tau^-) \approx BR(H \rightarrow \tau^+\tau^-)$ in the alignment limit and we can use the constraints obtained in Chapter 3 if we interpret $\kappa_{\phi gg}$ shown there as $\sqrt{\kappa_{A gg}^2 + \kappa_{H gg}^2}$ and $BR(\phi \rightarrow \tau\tau)$ as $BR(A \rightarrow \tau^+\tau^-) + BR(H \rightarrow \tau^+\tau^-)$. In Fig. 6.1.3 we plot the constraints on $m_A - \tan\beta$ plane from the 8 TeV LHC $\tau\tau$ channel results for these two scenarios.

6.1.2 2HDM type-X

We recall from Chapter 5 that in 2HDM-X, all the quarks couple to the H, A like $\cot\beta$ and all the leptons couple to H, A as $\tan\beta$. Since all the SM quarks couple very weakly to A for large $\tan\beta$, $\sigma(gg \rightarrow A)$ becomes very small for large $\tan\beta$. As a consequence there are no constraints from $\sigma(pp \rightarrow A) \times BR(A \rightarrow \tau^+\tau^-)$. In Fig. 6.1.4 we show the tree-level $BR(A \rightarrow \tau^+\tau^-, b\bar{b}, t\bar{t})$. The $BR(A \rightarrow VV)$ for the Type-X 2HDM is shown in Fig. 6.3.1 (by the dashed-black curve) in section 6.3.

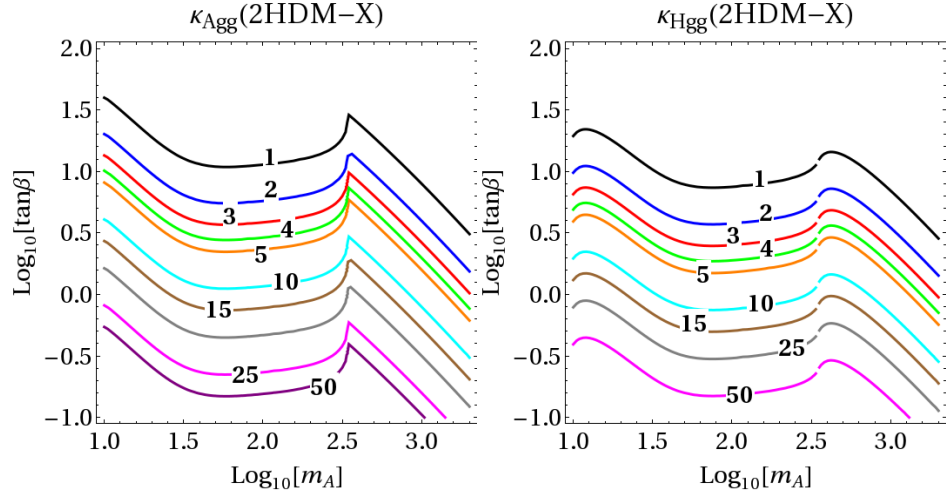


Figure 6.1.5: For the Type-X 2HDM, contours of $\kappa_{A_{gg}}$ (left) and $\kappa_{H_{gg}}$ (right).

In Fig. 6.1.5 we plot contours of $\kappa_{A_{gg}}$ and $\kappa_{H_{gg}}$. From this one can read off $\sigma(gg \rightarrow \phi)$ for 8 TeV and 14 TeV LHC from Fig. 3.1.1 in Chapter 3.

6.2 2HDM with vectorlike fermions

In this section we will extend the 2HDM to include new vector-like fermions. As mentioned before, there are several examples of UV complete models that have a 2HDM structure. In order to make the theory symmetric under the larger group, they also necessarily have new vector-like fermions which together with the SM fermions furnish a complete representation of the bigger symmetry group. Instead of committing to a single UV complete model, here we study the phenomenology of the A, H in some effective models where we add vector-like fermions to the 2HDM. Such an analysis will capture many of the common features present in realistic BSM theories as far as the phenomenology of A, H is concerned. We mainly focus on the scenario where $m_\phi < 2M_{VLF}$. We do not study the scenario where ϕ can decay to a pair of vector-like fermions. In order to be safe from direct search limits [111, 134, 135, 136] on VLQ mass we will take $M_{VLQ} > 920$ GeV. We first study the scenario where the VLFs have off-diagonal couplings with the third generation SM fermions. Subsequently we consider the scenario where the off-diagonal coupling of the VLFs with the SM fermions are absent.

6.2.1 2HDM with VLQ-SM Yukawa coupling

In this section we consider the scenario where VLFs couple to the third generation SM quarks. These kinds of models are very similar in nature to many of the realistic BSM theories. We analyze three situations separately: the *MVU* model where we introduce an $SU(2)$ singlet VLQ of charge $2/3$ to the 2HDM-II, the *MVD* model where we introduce an $SU(2)$ singlet VLQ of charge $-1/3$ to the 2HDM-II and the *MVQ* model where we introduce a VLQ $SU(2)$ doublet to the 2HDM-II. We also consider an explicit example of an UV complete model namely $SU(6)/Sp(6)$ little-Higgs model [5] where our analysis can be used to obtain the effective $\kappa_{\phi gg}$ couplings and $\sigma(gg \rightarrow \phi)$.

MVU model:

Here we introduce an $SU(2)$ -singlet VLF ψ , with EM charge $2/3$, and add to the 2HDM Type-II Lagrangian the following terms

$$\mathcal{L} \supset M_\psi \bar{\psi}\psi - \left(y_1 \bar{q}_L \tilde{\Phi}_1 \psi_R + h.c. \right). \quad (6.2.1)$$

After EWSB the mass terms for the EM-charge $2/3$ fermions can be written as

$$\mathcal{L}^{mass} = -\frac{1}{\sqrt{2}} \left(y_u v_2 \bar{t}_L t_R + y_1 v_1 \bar{t}_L \psi_R + h.c. \right) + M_\psi \bar{\psi}\psi. \quad (6.2.2)$$

We define the mass eigenstates $t_{L,R}^0$ and $t_{2L,R}$, for the EM-charge $2/3$ quarks as

$$\begin{aligned} t_{L,R} &= \cos \theta_{L,R}^U t_{L,R}^0 - \sin \theta_{L,R}^U t_{2L,R}, \\ \psi_{L,R} &= \sin \theta_{L,R}^U t_{L,R}^0 + \cos \theta_{L,R}^U t_{2L,R}. \end{aligned} \quad (6.2.3)$$

The mixing angles are given by

$$\begin{aligned}\tan 2\theta_L^U &= \frac{2\sqrt{2}y_1v_1M_\psi}{y_u^2v_2^2 - 2M_\psi^2 + y_1^2v_1^2} \\ \tan 2\theta_R^U &= \frac{2\sqrt{2}y_1y_uv_1v_2}{y_u^2v_2^2 - 2M_\psi^2 - y_1^2v_1^2}.\end{aligned}\quad (6.2.4)$$

The mass eigenvalues are given by

$$m_{t^0, t_2} = \frac{1}{2} \left(\sqrt{\left(\frac{y_u}{\sqrt{2}}v_2 + M_\psi\right)^2 + \frac{y_1^2}{2}v_1^2} \mp \sqrt{\left(\frac{y_u}{\sqrt{2}}v_2 - M_\psi\right)^2 + \frac{y_1^2}{2}v_1^2} \right). \quad (6.2.5)$$

For notational brevity we call t^0 simply as t , which we will identify with the SM top-quark. Constraints on the mixing from EWPT and a vector-like top decaying to Wb, Zt, Ht are studied in Refs. [112, 116, 137, 138]. The A couplings to the EM-charge 2/3 fermions in terms of the mass eigenstates are given by

$$\mathcal{L} = \frac{i}{\sqrt{2}}A \left(y_{Att} \bar{t}_L t_R + y_{At_2t_2} \bar{t}_{2L} t_{2R} + y_{At_2t} \bar{t}_{2L} t_R + y_{Att_2} \bar{t}_L t_{2R} \right) + h.c. , \quad (6.2.6)$$

where

$$\begin{aligned}y_{Att} &= (y_u c_L^U c_R^U \cos \beta - y_1 c_L^U s_R^U \sin \beta), \\ y_{At_2t_2} &= (y_u s_L^U s_R^U \cos \beta + y_1 s_L^U c_R^U \sin \beta), \\ y_{At_2t} &= -(y_u s_L^U c_R^U \cos \beta - y_1 c_L^U s_R^U \sin \beta), \\ y_{Att_2} &= -(y_u c_L^U s_R^U \cos \beta + y_1 c_L^U c_R^U \sin \beta).\end{aligned}\quad (6.2.7)$$

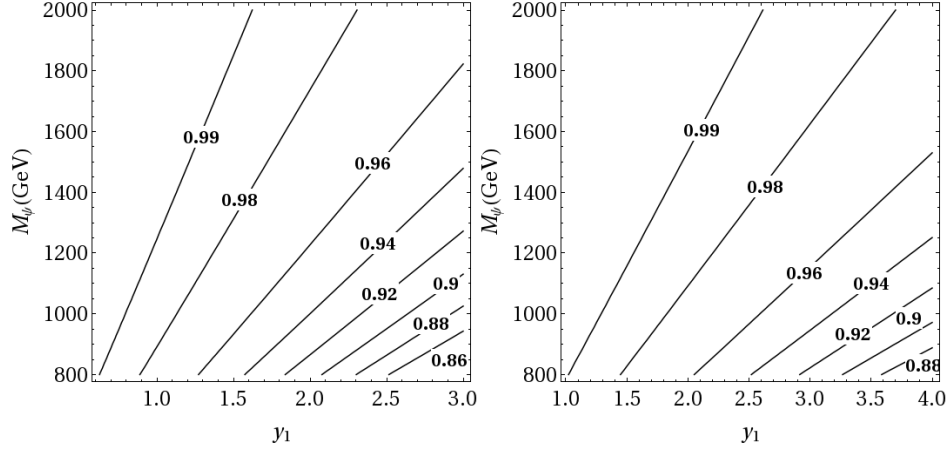


Figure 6.2.1: For the MVU model, contours of κ_{htt} for $\tan\beta = 1$ (left) and $\tan\beta = 5$ (right) with y_u chosen such that $m_t = 163$ GeV.

The h couplings to the EM-charge $2/3$ fermions are given by,

$$\begin{aligned}
y_{htt} &= (-y_u c_L^U c_R^U \cos\alpha + y_1 c_L^U s_R^U \sin\alpha), \\
y_{ht_2 t_2} &= (-y_u s_L^U s_R^U \cos\alpha - y_1 s_L^U c_R^U \sin\alpha), \\
y_{ht_2 t} &= (y_u s_L^U c_R^U \cos\alpha - y_1 c_L^U s_R^U \sin\alpha), \\
y_{htt_2} &= (y_u c_L^U s_R^U \cos\alpha + y_1 c_L^U c_R^U \sin\alpha).
\end{aligned} \tag{6.2.8}$$

Because of the $t - \psi$ mixing the y_{htt} will be different from its SM value (y_{htt}^{SM}). We define the quantity $\kappa_{htt} = y_{htt}/y_{htt}^{SM}$ which parametrizes the deviation of the htt coupling from its SM value. The experimental limit on κ_{htt} is $0.63 < |\kappa_{htt}| < 1.2$ [50]. In Fig. 6.2.1 we plot κ_{htt} in the $y_1 - M_\psi$ plane for $\tan\beta=1$ and 5. For large y_1 and small M_ψ , the mixing is large and the κ_{htt} differs from 1 by about 15% as can be seen from Fig. 6.2.1.

In Fig. 6.2.1 we show contours of κ_{Agg}^{VLF}/y_1^2 in the $m_A - M_\psi$ plane for $\{\tan\beta, y_u\} = \{1, 1.4\}$ and $\{5, 1\}$, and also show κ_{Agg}^{VLF} as a function of y_1 for 1000 GeV, $M_\psi = 1250$ GeV and $\tan\beta = 0.1, 1, 5, 10, 15$. For large $\tan\beta$, the mixing angles become small, which makes κ_{Agg}^{VLF} small. For Fig. 6.2.1, we fix $y_u = 1.4$ so that m_t is close to its \overline{MS} value $m_t^{\overline{MS}} = 163$ GeV [139], and once a specific choice of y_1 is made, m_t can be fixed exactly by choosing y_u slightly differently; the resulting change in κ_{Agg}^{VLF} due to such differences in y_u is insignificant. The

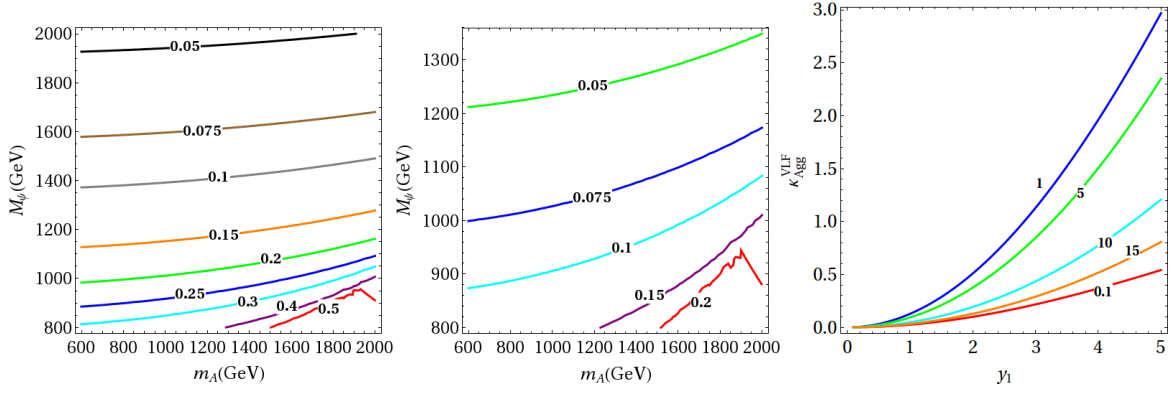


Figure 6.2.2: Contours of k_{Agg}^{VLF}/y_1^2 for $\{\tan\beta, y_u\} = \{1, 1.4\}$ (left) and $\{5, 1\}$ (middle) for the *MVU* model. k_{Agg}^{VLF} as a function of y_1 , for $m_A = 1000$ GeV, $M_\psi = 1250$ GeV and $\tan\beta = 0.1, 1, 5, 10, 15$ is plotted on the right.

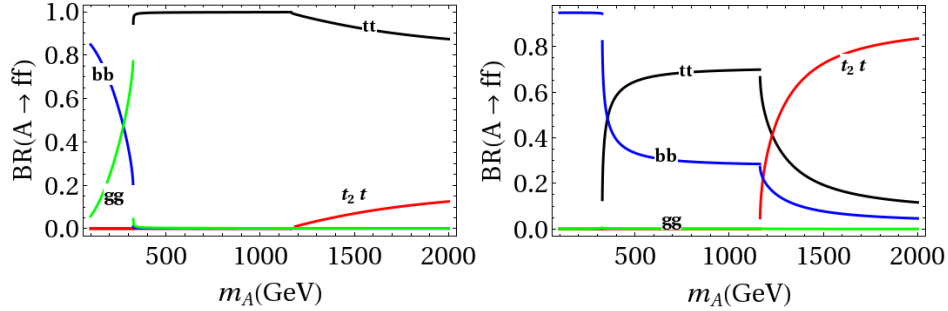


Figure 6.2.3: Contours of $BR(A \rightarrow tt)$ (black), $BR(A \rightarrow bb)$ (blue), $BR(A \rightarrow t_2 t)$ (red), $BR(A \rightarrow gg)$ (green) with $M_\psi = 1000$ GeV, $y_1 = 1$ for $\tan\beta = 1$ (left) and 5 (right), for the *MVU* model, with y_u chosen such that $m_t = 163$ GeV.

fermionic BRs for $m_A < (M_{t_2} + m_t)$ will be largely unchanged from the Type-II 2HDM plots shown in Fig. 6.2.3. However, if $m_A > (M_{t_2} + m_t)$ the $A \rightarrow t_2 t$ decay becomes kinematically allowed. In Fig. 6.2.3 we plot $BR(A \rightarrow tt)$, $BR(A \rightarrow bb)$, $BR(A \rightarrow gg)$ and $BR(A \rightarrow t_2 t)$, for $M_\psi = 1$ TeV, $y_1 = 1$ and $\tan\beta = \{1, 5\}$ with y_u fixed such that m_t is at the physical value. For $\tan\beta=5$, $BR(A \rightarrow tt)$ becomes small since $y_{Att} \propto \cot\beta$. $BR(A \rightarrow \gamma\gamma, Z\gamma)$ do not change by much from the 2HDM-II case.

MVD model:

In the MVD model, we introduce an SU(2)-singlet VLF χ , with EM charge $-1/3$, and add to the 2HDM Type-II Lagrangian the following terms

$$\mathcal{L}_A = M_\chi \bar{\chi}\chi - (y_2 \bar{q}_L \Phi_1 \chi_R + h.c.) . \quad (6.2.9)$$

The mass eigenstates, $b_{L,R}^0$ and $b_{2L,R}$ for the EM-charge $-1/3$ fermions are defined in the same way as in Eq. 6.2.3 with the mixing angles $\theta_{L,R}^D$. The mixing angles are given by

$$\begin{aligned} \tan 2\theta_L^D &= \frac{2\sqrt{2}y_2v_1M_\psi}{y_d^2v_1^2 - 2M_\chi^2 + y_2^2v_1^2} \\ \tan 2\theta_R^U &= \frac{2\sqrt{2}y_1y_u v_1v_2}{y_d^2v_1^2 - 2M_\chi^2 - y_2^2v_1^2}. \end{aligned} \quad (6.2.10)$$

The mass eigenvalues are given by

$$m_{t,t_2} = \frac{1}{2} \left(\sqrt{\left(\frac{y_d}{\sqrt{2}}v_1 + M_\chi\right)^2 + \frac{y_2^2}{2}v_1^2} \mp \sqrt{\left(\frac{y_d}{\sqrt{2}}v_1 - M_\chi\right)^2 + \frac{y_2^2}{2}v_1^2} \right). \quad (6.2.11)$$

The A couplings to the EM-charge $-1/3$ fermions are given by

$$\begin{aligned} y_{Att} &= (y_d c_L^D c_R^D \sin \beta - y_2 c_L^D s_R^D \sin \beta), \\ y_{At_2t_2} &= (y_d s_L^D s_R^D \sin \beta + y_2 s_L^D c_R^D \sin \beta), \\ y_{At_2t} &= -(y_d s_L^D c_R^D \sin \beta - y_2 c_L^D s_R^D \sin \beta), \\ y_{Att_2} &= -(y_d c_L^D s_R^D \sin \beta + y_2 c_L^D c_R^D \sin \beta). \end{aligned} \quad (6.2.12)$$

The h couplings to the charge $-1/3$ fermions are given by

$$\begin{aligned} y_{htt} &= (y_d c_L^D c_R^D \sin \alpha + y_2 c_L^D s_R^D \sin \alpha), \\ y_{ht_2t_2} &= (y_d s_L^D s_R^D \sin \alpha - y_2 s_L^D c_R^D \sin \alpha), \\ y_{ht_2t} &= (-y_d s_L^D c_R^D \sin \alpha - y_2 c_L^D s_R^D \sin \alpha), \\ y_{htt_2} &= (-y_d c_L^D s_R^D \sin \alpha + y_2 c_L^D c_R^D \sin \alpha). \end{aligned} \quad (6.2.13)$$

As in the case of charge $2/3$ fermions, we choose y_d such that $m_b^{\overline{MS}} = 4.2$ GeV [140]; y_{hbb} stays close its SM value. In Fig. 6.2.4, we plot contours of $\kappa_{Agg}^{\text{VLF}}/y_2^2$ in the $m_A - M_\chi$ plane

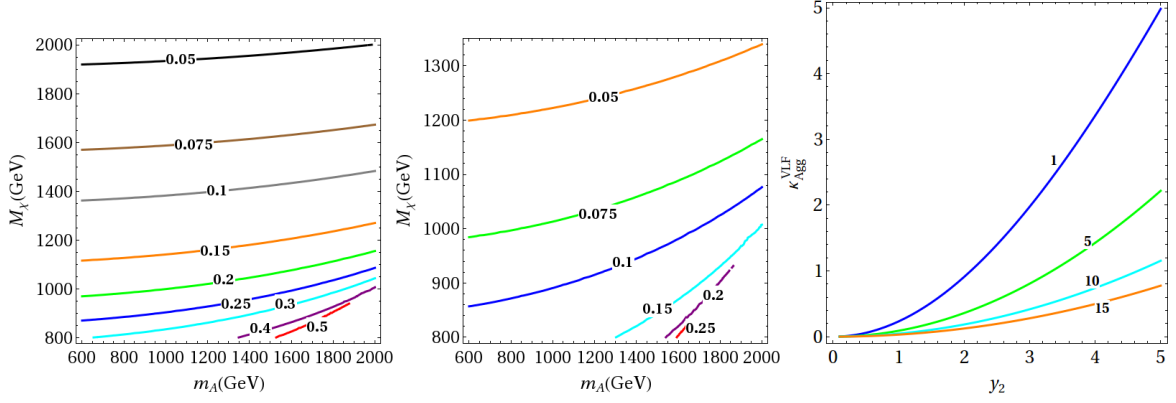


Figure 6.2.4: Contours of k_{Agg}^{VLF}/y_2^2 for $\{\tan\beta, y_d\} = \{1, 0.03\}$ (left) and $\{5, 0.12\}$ (middle) for the MVD model. k_{Agg}^{VLF} with y_2 for $m_A = 1500$ GeV, $M_\chi = 1000$ GeV and $\tan\beta = 1, 5, 10, 15$ is plotted on the right..

for $\{\tan\beta, y_d\} = \{1, 0.03\}$ and $\{5, 0.12\}$, and κ_{Agg}^{VLF} as a function of y_2 for $m_A = 1500$ GeV, $M_\chi = 1000$ GeV for $\tan\beta = 1, 5, 10, 15$.

MVQ model

For the MVQ model, we add an $SU(2)$ doublet VLF Q' and add to the Type-II 2HDM Lagrangian the terms

$$\mathcal{L} \supset M_{QQ} \bar{Q}' Q' + \left(M_{qQ} \bar{q}_L Q'_R - \tilde{y}_1 \bar{Q}'_L \tilde{\Phi}_2 t_R - \tilde{y}_2 \bar{Q}'_L \Phi_1 b_R + h.c. \right). \quad (6.2.14)$$

Below we only show the top-sector since in most of the BSM models, usually the top sector is relevant. The M_{qQ} induces a mixing between Q'_L and q_L . We diagonalize the VLF masses by redefining the q and Q' fields by an orthogonal rotation to obtain

$$\mathcal{L} \supset M_{QQ}^{eff} \bar{Q}' Q' + \left(-y_u^{eff} \bar{q}_L \tilde{\Phi}_2 t_R - \tilde{y}_1^{eff} \bar{Q}'_L \tilde{\Phi}_2 t_R + h.c. \right), \quad (6.2.15)$$

with $M_{QQ}^{eff} \equiv \sqrt{(M_{QQ}^2 + M_{qQ}^2)}$, $y_u^{eff} \equiv (y_u M_{QQ} - \tilde{y}_1 M_{qQ})/M_{QQ}^{eff}$, $\tilde{y}_1^{eff} \equiv (y_u M_{qQ} + \tilde{y}_1 M_{QQ})/M_{QQ}^{eff}$, which imply $y_u^{eff} = (y_u - \tilde{y}_1 M_{qQ}/M_{QQ})/\sqrt{1 + (M_{qQ}/M_{QQ})^2}$ and $\tilde{y}_1^{eff} = y_u^{eff} M_{qQ}/M_{QQ} + \tilde{y}_1 \sqrt{1 + (M_{qQ}/M_{QQ})^2}$. The $\kappa_{\phi gg}$ due to the t', b' in the MVQ model are qualitatively similar to the MVU case presented earlier and we do not show this explicitly.

SU(6)/Sp(6) little-Higgs model

Here we apply the results of our analysis to a specific example of a BSM model namely the SU(6)/Sp(6) little-Higgs model (LSS) [5]. In the LSS model, an SU(6) global symmetry is broken down to Sp(6) by the expectation value of an antisymmetric condensate. Interestingly, the scalar sector of this model has a 2HDM structure and to complete the symmetry representation of the bigger symmetry group it also has new vector-like fermions. In Ref. [10] we have studied this model in detail. It has two charge $2/3$ VLQs t_2, t_3 and two charge $-1/3$ VLQs b_2, b_3 . Here we apply some of the results of Sec. 6.2.1 to this model. While comparing with Ref. [10], one should keep in mind that there we had $\tan\beta = v_1/v_2$ while in this analysis we have $\tan\beta = v_2/v_1$, and therefore $\tan\beta$ here is related to that of Ref. [10] via $\tan\beta = (1/\tan\beta^{LSS})$. In Ref. [10] we have found the allowed points of the parameter space from the 8 TeV LHC Higgs measurements and the precision electroweak constraints. Some of the allowed points can be found in Appendix B of Ref. [10]. Here we focus on two such sample points namely sample-points 1 and 2. For the sample-point-1, the two lightest VLFs are the t_2 with a mass of 1218 GeV, the b_2 with a mass of 1315 GeV, and we have $\tan\beta = 1.36$, $m_A = 1671$ GeV, $y_1 = 1.7$, $y_u = 1.2$ and $m_t \approx 164$ GeV. Here y_1 is given by $y_1 = y_1^{LSS} c_{23}$, and for point-1, since $y_1 \gg y_4$, to a very good approximation $s_{14} \approx 1$ and $c_{14} \approx 0$. Also $m_t \approx c_{23} y_2 v_2 / \sqrt{2}$ in the limit where t_3 is decoupled away, i.e. $y_u = y_2 c_{23}$, and $c_{23} \approx 0.9$. The b_2 is an SU(2)-singlet since it does not mix with the other charge $-1/3$ states. Keeping only the lighter t_2 since the t_3 is somewhat heavier, a good approximation is obtained by considering the addition of only a singlet EM charge $+2/3$ state ψ as introduced in Eq. 6.2.1. Ignoring the smaller b_2 contribution, the κ_{Agg}^{VL} due to the t_2 can be read off from the $\tan\beta = 1$ curve of the rightmost panel of Fig. 6.2.1 to be approximately 0.4. This is about 10% of the SM-fermion contribution. For the sample-point-2 the the lightest VLQ is the b_2 with a mass of 947.5 GeV. The b_2 is an SU(2)-singlet state and does not mix with the other charge $-1/3$ states. For this point, $m_A = 1671$ GeV, $\tan\beta = 1.36$, $y_2 = 1.422$, $c_{23} = 1.15$. κ_{Agg} can be read off from the $\tan\beta = 1$ curve of the rightmost panel of Fig. 6.2.4 to be approximately 0.3.

6.2.2 2HDM-II with VLQ-VLQ Yukawa coupling

In this section we study few example models where the off-diagonal couplings of the VLFs with the SM fermions are shut-off. We add SU(2) doublet and singlet VLFs with SM-like hypercharge assignments, and write Yukawa couplings between them both involving the $\Phi_{1,2}$. We separately consider three minimal extensions of 2HDM-II: $MVQD_{11}$ model where we introduce an SU(2) doublet VLQ and an SU(2) singlet down-type VLQ which have Yukawa couplings only with Φ_1 , $MVQU_{22}$ model which is similar to $MVQD_{11}$ model but with an up-type VLQ singlet (instead of a down-type one) and has Yukawa couplings involving only Φ_2 , $MVQU_{12}$ model where the right-handed up-type singlet couples to Φ_1 , whereas the left handed up-type singlet couples to Φ_2 . We also consider a model similar to $MVQD_{11}$ but for 2HDM type-X and denote it by $MVQDX_{11}$. Although there could be Yukawa couplings between a VLF and an SMF also present, we do not write them here for simplicity, and their effects are investigated separately in section 6.2.1 .

$MVQD_{11}$ model:

To the Type-II 2HDM we introduce one doublet VLQ, $\psi = (\psi_1, \psi_2)$ with hypercharge Y_ψ and one singlet VLQ (χ) with hypercharge $(Y_\psi - 1/2)$ so that VLF couplings with Φ_1 are allowed. The additional Lagrangian terms to the 2HDM-II are

$$\mathcal{L} \supset \bar{\psi} i \not{D} \psi + \bar{\chi} i \not{D} \chi - (y_1 \bar{\psi}_L \Phi_1 \chi_R + \tilde{y}_1 \bar{\psi}_R \Phi_1 \chi_L + \text{h.c.}) - M_\psi \bar{\psi} \psi - M_\chi \bar{\chi} \chi. \quad (6.2.16)$$

We can also write the terms $\bar{\psi}_L \Phi_2 \chi_R$ and $\bar{\psi}_R \Phi_2 \chi_L$, which we do not add here but will consider them subsequently as another model. These terms are forbidden if $\chi \rightarrow -\chi$ under

the Z_2 symmetry of 2HDM-II. The terms involving h , A , H and VLFs after EWSB are

$$\begin{aligned}
\mathcal{L} \supset & -M_\psi \bar{\psi} \psi - M_\chi \bar{\chi} \chi + \frac{1}{\sqrt{2}} A \sin \beta (i y_1 \bar{\psi}_{2L} \chi_R + i \tilde{y}_1 \bar{\psi}_{2R} \chi_L + h.c.) \\
& - \frac{v}{\sqrt{2}} \cos \beta (y_1 \bar{\psi}_{2L} \chi_R + \tilde{y}_1 \bar{\psi}_{2R} \chi_L + h.c.) + \frac{1}{\sqrt{2}} h \sin \alpha (y_1 \bar{\psi}_{2L} \chi_R + \tilde{y}_1 \bar{\psi}_{2R} \chi_L + h.c.) \\
& - \frac{1}{\sqrt{2}} H \cos \alpha (y_1 \bar{\psi}_{2L} \chi_R + \tilde{y}_1 \bar{\psi}_{2R} \chi_L + h.c.) \tag{6.2.17}
\end{aligned}$$

Gauge interactions of the VLFs are present and not shown explicitly. ψ_2 and χ mix after EWSB, while ψ_1 is itself a mass eigenstate. We define the mass eigenstates ζ_1 and ζ_2 as

$$\begin{aligned}
\psi_{2L,R} &= \zeta_{1L,R} \cos \theta_{L,R} - \zeta_{2L,R} \sin \theta_{L,R}, \\
\chi_{L,R} &= \zeta_{1L,R} \sin \theta_{L,R} + \zeta_{2L,R} \cos \theta_{L,R}, \tag{6.2.18}
\end{aligned}$$

where the mixing angles are given by

$$\begin{aligned}
\tan 2\theta_L &= \frac{2\sqrt{2}vc_\beta(y_1 M_\chi + \tilde{y}_1 M_\psi)}{2(M_\psi^2 - M_\chi^2) - v^2 s_\beta^2(\tilde{y}_1^2 - y_1^2)}, \\
\tan 2\theta_R &= \frac{2\sqrt{2}vc_\beta(y_1 M_\chi + \tilde{y}_1 M_\psi)}{2(M_\psi^2 - M_\chi^2) + v^2 s_\beta^2(\tilde{y}_1^2 - y_1^2)}. \tag{6.2.19}
\end{aligned}$$

The mass eigen values are given by

$$M_{1,2} = \frac{1}{2} \sqrt{(M_\psi + M_\chi)^2 + \frac{1}{2} c_\beta^2 v^2 (y_1 - \tilde{y}_1)^2} \pm \sqrt{(M_\psi - M_\chi)^2 + \frac{1}{2} v^2 c_\beta^2 (y_1 + \tilde{y}_1)^2}. \tag{6.2.20}$$

In terms of these mass eigenstates, Eq. (6.2.17) can be written as

$$\begin{aligned}
\mathcal{L} \supset & -M_i \bar{\zeta}_i \zeta_i - M_\psi \bar{\psi}_1 \psi_1 + \kappa_{ij} Z_\mu \bar{\zeta}_i \gamma_\mu \zeta_j + e Q_i A_\mu \bar{\zeta}_i \gamma_\mu \zeta_i - y_{ij}^A (i A \bar{\zeta}_i \zeta_j + h.c.) \\
& - y_{ij}^h (h \bar{\zeta}_i \zeta_j + h.c.) - y_{ij}^H (H \bar{\zeta}_i \zeta_j + h.c.), \tag{6.2.21}
\end{aligned}$$

where $i, j = 1, 2$. The κ_{ij} are given by

$$\begin{aligned}
\kappa_{11} &= (g/c_W)[(T^3/2)(c_L^2 + c_R^2) - Qs_W^2], \\
\kappa_{22} &= (g/c_W)[(T^3/2)(s_L^2 + s_R^2) - Qs_W^2], \\
\kappa_{12} &= -(g/c_W)(T^3/2)(s_L c_L + s_R c_R)
\end{aligned} \tag{6.2.22}$$

and the y_{ij}^A are given by

$$\begin{aligned}
y_{11}^A &= (1/\sqrt{2})s_\beta(-y_1 c_L s_R + \tilde{y}_1 s_L c_R), \\
y_{22}^A &= (1/\sqrt{2})s_\beta(y_1 s_L c_R - \tilde{y}_1 c_L s_R), \\
y_{12}^A &= -(1/\sqrt{2})s_\beta(y_1 c_L c_R + \tilde{y}_1 s_L s_R), \\
y_{21}^A &= (1/\sqrt{2})s_\beta(y_1 s_L s_R + \tilde{y}_1 c_L c_R).
\end{aligned} \tag{6.2.23}$$

The y_{ij}^h are given

$$\begin{aligned}
y_{11}^h &= -(1/\sqrt{2})s_\alpha(y_1 c_L s_R + \tilde{y}_1 s_L c_R), \\
y_{22}^h &= (1/\sqrt{2})s_\alpha(y_1 s_L c_R + \tilde{y}_1 c_L s_R), \\
y_{12}^h &= -(1/\sqrt{2})s_\alpha(y_1 c_L c_R - \tilde{y}_1 s_L c_R), \\
y_{21}^h &= -(1/\sqrt{2})s_\alpha(-y_1 s_L s_R + \tilde{y}_1 c_L c_R).
\end{aligned} \tag{6.2.24}$$

The couplings y_{ij}^H can be obtained from the y_{ij}^h by the replacement, $s_\alpha \rightarrow -c_\alpha$. We take the y_1 and \tilde{y}_1 to be real, enforcing CP invariance in the BSM sector. The relative sign between y_1 and \tilde{y}_1 in Eq. (6.2.16) is physical for the following reason. If we want to get rid of this relative sign we need to make the transformations $\chi_L \rightarrow -\chi_L$ and $\chi_R \rightarrow \chi_R$, or $\chi_L \rightarrow \chi_L$ and $\chi_R \rightarrow -\chi_R$. In either case, the M_χ changes its sign and is therefore a physical effect. For chiral fermions, the sign of the mass term is not physical since one can rotate it away by the above transformations.

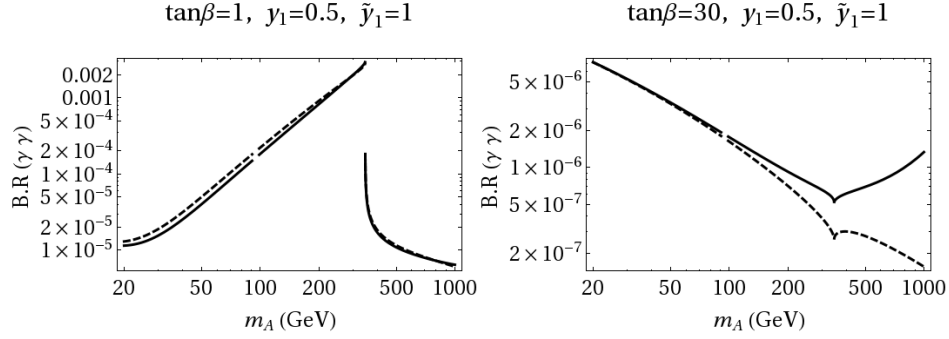


Figure 6.2.5: $BR(A \rightarrow \gamma\gamma)$ (top-panel) and $BR(A \rightarrow Z\gamma)$ (bottom-panel) with $M_\psi = M_\chi = 1000$ (GeV), $\tan\beta = 1$ (left) and 30 (right) in $MVQD_{11}$ model (solid-black) and in 2HDM Type-II (dashed-black). $BR(A \rightarrow f\bar{f})$ in Type-II 2HDM are as shown in Fig. 6.1.1

Instead of the χ (with hypercharge $(Y_\psi - 1/2)$), if we consider a VLF (say ξ) of hypercharge $(Y_\psi + 1/2)$, we get a different model where the ξ couples to the $\tilde{\Phi}_1$ instead of the Φ_1 . This model will have similar phenomenology as $MVQD_{11}$ model, which we discuss later.

The effective k_{AVV} couplings for this model are given in Appendix A. When $y_1 = \tilde{y}_1$, in addition to CP invariance, the Lagrangian in Eq. (6.2.17) is also invariant under P and C individually, with A transforming as $A \xrightarrow{P} A$, $A \xrightarrow{C} -A$. This implies that the VLF contribution to κ_{AVV} is zero since $AV_{\mu\nu}\tilde{V}^{\mu\nu}$ is not P invariant (although it is CP invariant). Also, the VLF contributions are maximum for $M_\psi = M_\chi$ when the mixing between the VLFs (ψ_2 and χ) is maximum. We will take M_ψ and M_χ to be equal from now on.

In Fig. 6.2.5, we plot $BR(A \rightarrow VV)$, for $Y_\psi = 1/6$ as an example, which is the SM quark-doublet hypercharge assignment. The tree-level decays to SM fermions $BR(A \rightarrow b\bar{b}, \tau^+\tau^-, t\bar{t})$ are unchanged from what is shown in Fig. 6.1.1 for the Type-II 2HDM. We see that for small values of $\tan\beta$ the VLF contribution to $BR(A \rightarrow VV)$ is small compared to the 2HDM-II. This is because the y_{ij} are proportional to $\sin\beta$. For large $\tan\beta$ and for large m_A , the VLF contributions to the $BR(A \rightarrow \gamma\gamma)$ become significant.

In Fig. 6.2.6, we plot contours of $\kappa_{A_{gg}}$ for $M_\psi = 800$ GeV, 1700 GeV. Using this, one can read-off the $\sigma(gg \rightarrow A)$ at the 8 and 14 TeV LHC from Fig. 3.1.1 in Chapter 3. The corresponding contours in the Type-II 2HDM (without the VLFs) are shown in Fig. 6.2.7. In Fig. 6.2.7 (left) we plot y_{11}^h and y_{11}^A (defined in Eq. (6.2.21)) in the alignment limit ($\beta - \alpha = \pi/2$), which shows that the h couplings to the VLFs become very small as $\tan\beta$ increases.

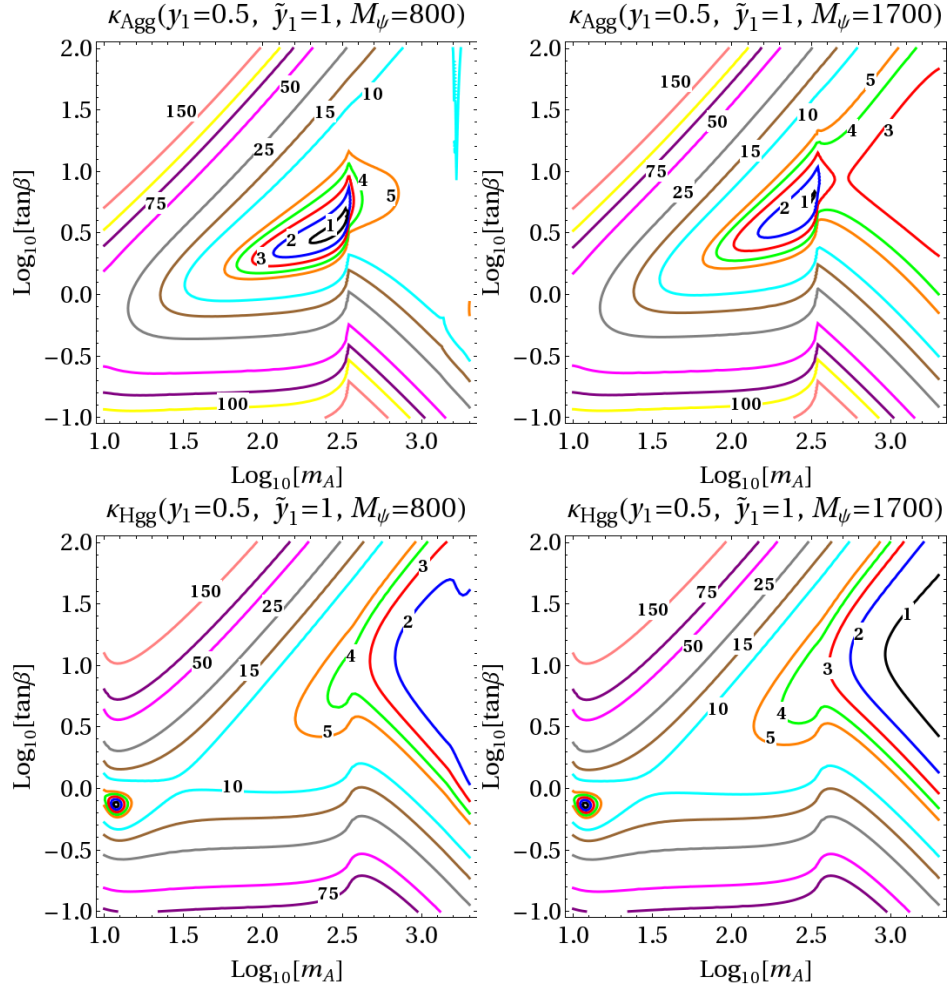


Figure 6.2.6: Contours of $\kappa_{A_{gg}}$ (top) and $\kappa_{H_{gg}}$ (bottom) for $M_\psi = M_\chi = 800$ GeV (left), 1700 GeV (right), $y_1 = 0.5$, $\tilde{y}_1 = 1$ for $MVQD_{11}$ model.

Thus, the VLFs can modify $\sigma(gg \rightarrow A)$ and $\Gamma(A \rightarrow VV)$ significantly, while the h remains SM-like as required by the LHC measurements of the 125 GeV state. We find that the VLF contributions partially cancel the SM fermion contributions for a range of low $\tan\beta$ values and for some ranges of the m_A , while for larger $\tan\beta$ the effective couplings always increase compared to the 2HDM-II. To illustrate this point more explicitly, we plot $\kappa_{A_{gg}}$ as a function of $\tan\beta$ in Fig. 6.2.7 for $m_A = 300$ GeV and 600 GeV.

In Fig. 6.2.6, we also plot contours of $\kappa_{H_{gg}}$ for $m_A = m_H$, in the alignment limit. Corresponding contours in Type-II 2HDM are shown in Fig. 6.1.2.

The constraint on the 2HDM was nontrivial only for large $\tan\beta$ (see Fig. 6.1.3). Therefore, for large $\tan\beta$, since the $\kappa_{\phi_{gg}}$ is bigger for this model compared to 2HDM (see Fig. 6.2.7), and $\text{BR}(\phi \rightarrow \tau\tau)$ from which the tightest constraint appears is almost unchanged, the con-

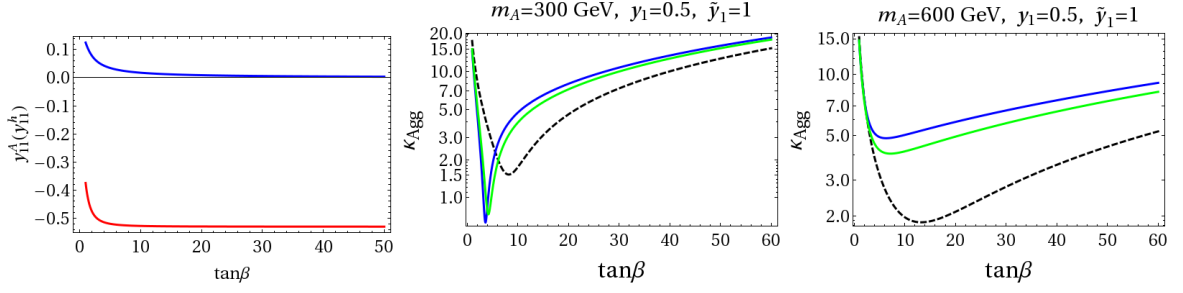


Figure 6.2.7: For the $MVQD_{11}$ model, y_{11}^A (red), y_{11}^h (blue) as a function of $\tan\beta$ (left); κ_{Agg} as a function of $\tan\beta$ for GeV (middle) and 600 GeV (right), with $y_1 = 0.5$, $\tilde{y}_1 = 1$ and $M_\psi = 800$ GeV (blue), 1000 GeV (green) .

straint on this model will be tighter.

$MVQU_{22}$ model:

We introduce one doublet VLQ (ψ) with hypercharge Y_ψ and one singlet VLQ (ξ) with hypercharge $Y_\psi + 1/2$, which couples only to Φ_2 . We add the following terms to the 2HDM-II Lagrangian

$$\mathcal{L} \supset \bar{\psi} i \not{D} \psi + \bar{\xi} i \not{D} \xi - y_2 \bar{\psi}_L \tilde{\Phi}_2 \xi_R - \tilde{y}_2 \bar{\psi}_R \tilde{\Phi}_2 \xi_L + \text{h.c} - M_\psi \bar{\psi} \psi - M_\xi \bar{\xi} \xi. \quad (6.2.25)$$

Here we do not include the terms $\bar{\psi}_L \tilde{\Phi}_1 \xi_R$ and $\bar{\psi}_R \tilde{\Phi}_1 \xi_L$ as their effects have been considered in $MVQD_{11}$ model. As the $\text{BR}(A \rightarrow VV)$ s do not change much compared to the 2HDM-II case, we do not show them here. Similar to $MVQD_{11}$ model we diagonalize the mass matrix by an orthogonal rotation and define the couplings y_{ij}^ϕ . The mass eigenvalues, mixing angles can be obtained from that of $MVQD_{11}$ by the replacements $y_1 \rightarrow y_2$ and $c_\beta \rightarrow s_\beta$. The y_{ij}^h 's in $MVQU_{22}$ model can be obtained from y_{ij}^h 's in $MVQD_{11}$ model by the replacements $y_1 \rightarrow y_2$ and $s_\alpha \rightarrow -c_\alpha$. The y_{ij}^A 's in $MVQU_{22}$ model can be obtained from the y_{ij}^A 's in $MVQD_{11}$ model by the replacements $y_1 \rightarrow y_2$ and $s_\beta \rightarrow c_\beta$. The couplings y_{ij}^H can be obtained from the y_{ij}^h 's in $MVQD_{11}$ model by the replacement $s_\alpha \rightarrow -s_\alpha$. The effective $\kappa_{\phi gg}$ in this model can be obtained the general expressions given in Appendix A.

In Fig. 6.2.8 we plot contours of κ_{Agg} and κ_{Hgg} in m_A - $\tan\beta$ plane. Since the y_{ij}^ϕ in this case goes like $\cos\beta$, for large $\tan\beta$ the $\kappa_{\phi gg}$ do not change by much from the 2HDM-II.

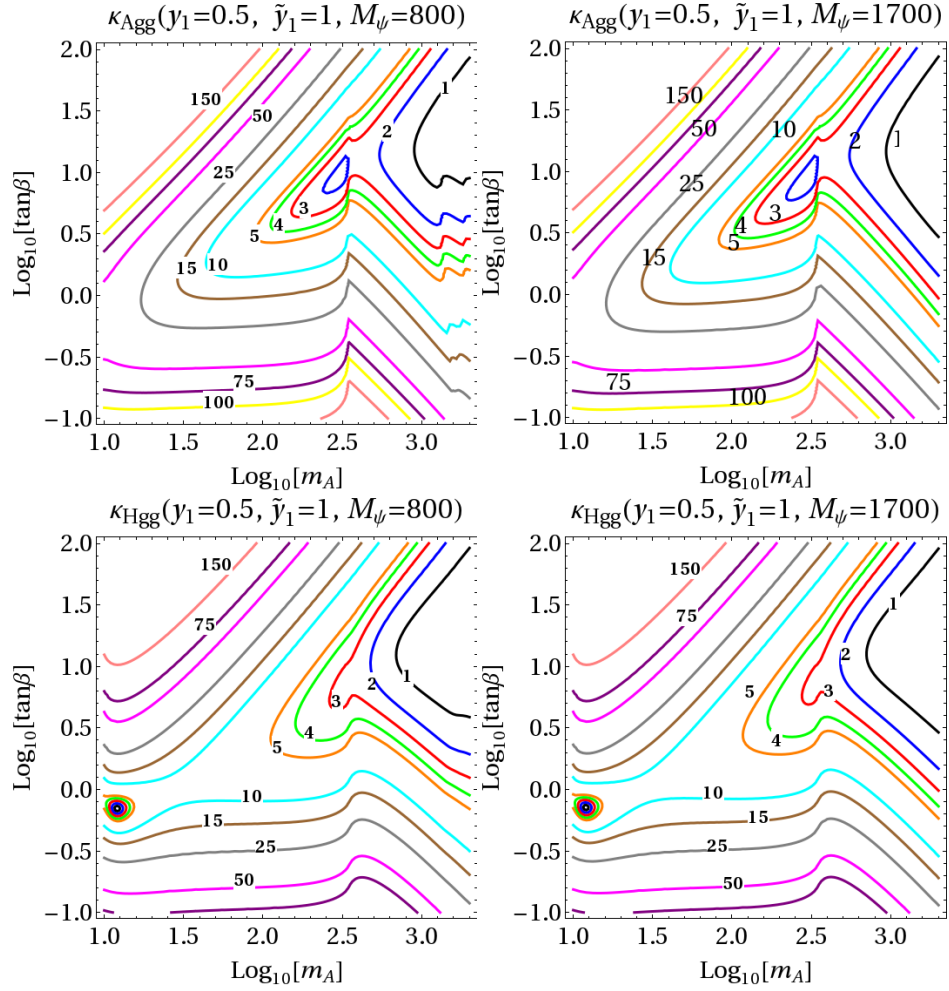


Figure 6.2.8: Contours of $\kappa_{A_{gg}}$ (top) and $\kappa_{H_{gg}}$ (bottom) for $M_\psi = M_\chi = 800$ GeV (left), 1700 GeV (right), $y_1 = 0.5$, $\tilde{y}_1 = 1$ for $MVQU_{22}$ model.

$MVQU_{12}$ model

We introduce one doublet VLQ(ψ) with hypercharge Y_ψ and one singlet VLQ (ξ) with hypercharge ($Y_\psi + 1/2$). We consider the case where ξ_R couples only to Φ_1 and ξ_L couples only to Φ_2 . To the 2HDM-II Lagrangian, we add

$$\mathcal{L} \supset \bar{\psi} i \not{D} \psi + \bar{\xi} i \not{D} \xi - (y \bar{\psi}_L \tilde{\Phi}_1 \xi_R + \tilde{y}_1 \bar{\psi}_R \tilde{\Phi}_2 \xi_L + \text{h.c.}) - M_\psi \bar{\psi} \psi - M_\chi \bar{\xi} \xi. \quad (6.2.26)$$

We get different models if instead of the couplings above, the ψ_R couples to $\tilde{\Phi}_1$ and ψ_L couples to $\tilde{\Phi}_2$, or, if instead of ξ we introduce a VLF singlet (say χ) with hypercharge ($Y_\psi - 1/2$) with couplings to Φ_1 and Φ_2 . All these models have similar phenomenology as $MVQU_{12}$ model. After EWSB, EM charge $Y_\psi + 1/2$ component of ψ mixes with ξ . We define the mass eigenstates ζ_1, ζ_2 as

$$\begin{aligned} \psi_{1L,R} &= \zeta_{1L,R} \cos \theta_{L,R} - \zeta_{2L,R} \sin \theta_{L,R}, \\ \xi_{L,R} &= \zeta_{1L,R} \sin \theta_{L,R} + \zeta_{2L,R} \cos \theta_{L,R}. \end{aligned} \quad (6.2.27)$$

The mixing angles are given by

$$\begin{aligned} \tan 2\theta_L &= \frac{2\sqrt{2}v(y_1 c_\beta M_\xi + \tilde{y}_1 s_\beta M_\psi)}{2(M_\psi^2 - M_\xi^2) - v^2(\tilde{y}_1^2 s_\beta^2 - y_1^2 c_\beta^2)}, \\ \tan 2\theta_R &= \frac{2\sqrt{2}v(y_1 c_\beta M_\xi + \tilde{y}_1 s_\beta M_\psi)}{2(M_\psi^2 - M_\xi^2) + v^2(\tilde{y}_1^2 s_\beta^2 - y_1^2 c_\beta^2)}. \end{aligned} \quad (6.2.28)$$

The mass eigenstates are given by

$$M_{1,2} = \frac{1}{2} \left(\sqrt{(M_\psi + M_\xi)^2 + \frac{1}{2}v^2(y_1 c_\beta - \tilde{y}_1 s_\beta)^2} \pm \sqrt{(M_\psi - M_\xi)^2 + \frac{1}{2}v^2(y_1 c_\beta + \tilde{y}_1 s_\beta)^2} \right). \quad (6.2.29)$$

The gauge interactions of the ζ_i , and the $\phi\zeta_i\zeta_j$ Yukawa couplings are defined in the same way as in Eq. (6.2.21). The effective couplings κ_{ij} are of the same from as in Eq. (6.2.21). The effective couplings y_{ij}^A are given by

$$\begin{aligned}
y_{11}^A &= (1/\sqrt{2})(y_1 s_\beta c_L s_R + \tilde{y}_1 c_\beta s_L c_R), \\
y_{22}^A &= -(1/\sqrt{2})(y_1 s_\beta s_L c_R + \tilde{y}_1 c_\beta c_L s_R), \\
y_{12}^A &= (1/\sqrt{2})(y_1 s_\beta c_L c_R - \tilde{y}_1 c_\beta s_L s_R), \\
y_{21}^A &= -(1/\sqrt{2})(y_1 s_\beta s_L s_R - \tilde{y}_1 c_\beta c_L c_R).
\end{aligned} \tag{6.2.30}$$

The effective couplings y_{ij}^h are given by

$$\begin{aligned}
y_{11}^h &= (1/\sqrt{2})(-y_1 s_\alpha c_L s_R + \tilde{y}_1 c_\alpha s_L c_R), \\
y_{22}^h &= (1/\sqrt{2})(y_1 s_\alpha s_L c_R - \tilde{y}_1 c_\alpha c_L s_R), \\
y_{12}^h &= -(1/\sqrt{2})(y_1 s_\alpha c_L c_R + \tilde{y}_1 c_\alpha s_L s_R), \\
y_{21}^h &= (1/\sqrt{2})(y_1 s_\alpha s_L s_R + \tilde{y}_1 c_\alpha c_L c_R).
\end{aligned} \tag{6.2.31}$$

The effective couplings y_{ij}^H can be obtained from the y_{ij}^h by the replacements $s_\alpha \rightarrow -c_\alpha$ and $c_\alpha \rightarrow s_\alpha$. In this model, the effective couplings do not reduce to zero for $y_1 = \tilde{y}_1$, unlike in $MVQD_{11}$ and $MVQU_{22}$ models, as there are no additional P and C symmetries in the VLF sector.

In Fig. 6.2.9, we plot the $BR(A \rightarrow VV)$ for an example choice of $Y_\psi = 1/6$. The $BR(A \rightarrow \gamma\gamma, Z\gamma)$ for $\tan\beta = 1, y_1 = 0.5, \tilde{y}_1 = 1$ and the tree-level $BR(A \rightarrow \tau\tau, bb, tt)$ are not explicitly shown in Fig. 6.2.9 as they are identical to those shown for the $MVQD_{11}$ model in Fig. 6.2.5, and Type-II 2HDM in Fig. 6.1.1 respectively.

In Fig. 6.2.10, we plot contours of $\kappa_{A\gamma\gamma}$ for $y_1 = \tilde{y}_1 = 1$ and $M_\psi = M_\xi = 800$ GeV and 1700 GeV. From this, one can obtain $\sigma(gg \rightarrow A)$ at the 8 and 14 TeV LHC from Fig. 3.1.1 in Chapter 3. For low values of $\tan\beta$ the effective coupling increases compared to the

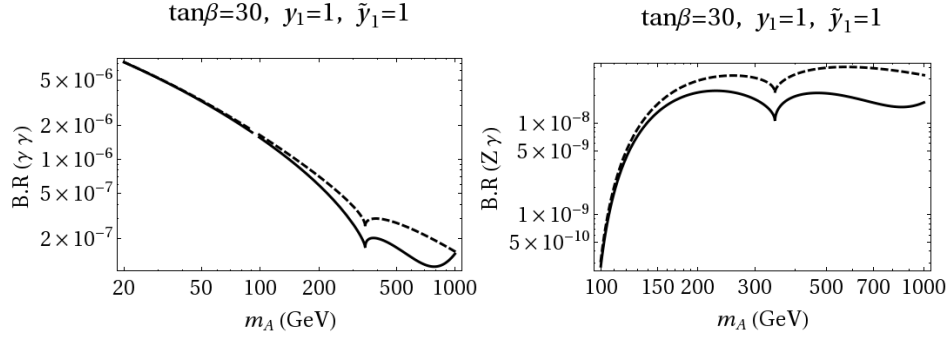


Figure 6.2.9: $BR(A \rightarrow \gamma\gamma)$ (left) and $BR(A \rightarrow Z\gamma)$ (right) with $M_\psi = M_\chi = 1000$ GeV for $\tan\beta = 30$ for $MVQU_{12}$ model (solid-black), and the corresponding variation in the Type-II 2HDM (dashed-black). These BR for $\tan\beta = 1$ and the $BR(A \rightarrow \tau\tau, bb, tt)$ are not explicitly shown here as they are identical to those in Figs. 6.2.5 and 6.1.1 respectively.

2HDM-II case, while for larger values of $\tan\beta$ the effective coupling decreases compared to the 2HDM-II. To show this more explicitly, we plot $\kappa_{A\text{gg}}$ with $\tan\beta$ in Fig. 6.2.11. The decreased coupling is due to a destructive interference between the contributions from SM fermions and the VLFs. If we reverse the sign of y_1 or \tilde{y}_1 , we get the opposite effect; for low values of $\tan\beta$ the effective coupling decreases compared to the 2HDM-II while for larger values of $\tan\beta$ the effective coupling increases compared to the 2HDM-II. In Fig. 6.2.10 we also plot contours of $\kappa_{H\text{gg}}$ in the alignment limit. From this, one can also obtain $\sigma(gg \rightarrow H)$ from Fig. 3.1.1 by reading $\kappa_{A\text{gg}}$ there as $\kappa_{H\text{gg}}$ as mentioned earlier.

In Fig. 6.2.12 we plot the region of the m_A - $\tan\beta$ parameter-space which is excluded at 95% confidence level for two cases, when only A is present, and when A and H are degenerate and both present. For comparison, we have also plotted the corresponding limit for the 2HDM-II case. We see that the constraints are loosened compared to the 2HDM-II due to the presence of VLFs. This happens because of the reduction of $\kappa_{A\text{gg}}$ ($\kappa_{H\text{gg}}$) compared to the 2HDM-II.

6.3 2HDM-X with VLQ-VLQ Yukawa coupling

To the 2HDM Type-X model in Eq. 5.1.1 in Chapter 5, we introduce VLFs in a similar fashion as in $MVQD_{11}$ model as a representative case, and call it $MVQDX_{11}$ model. The other ways of coupling VLFs similar to $MVQU_{22}$ or $MVQU_{12}$ model will be qualitatively

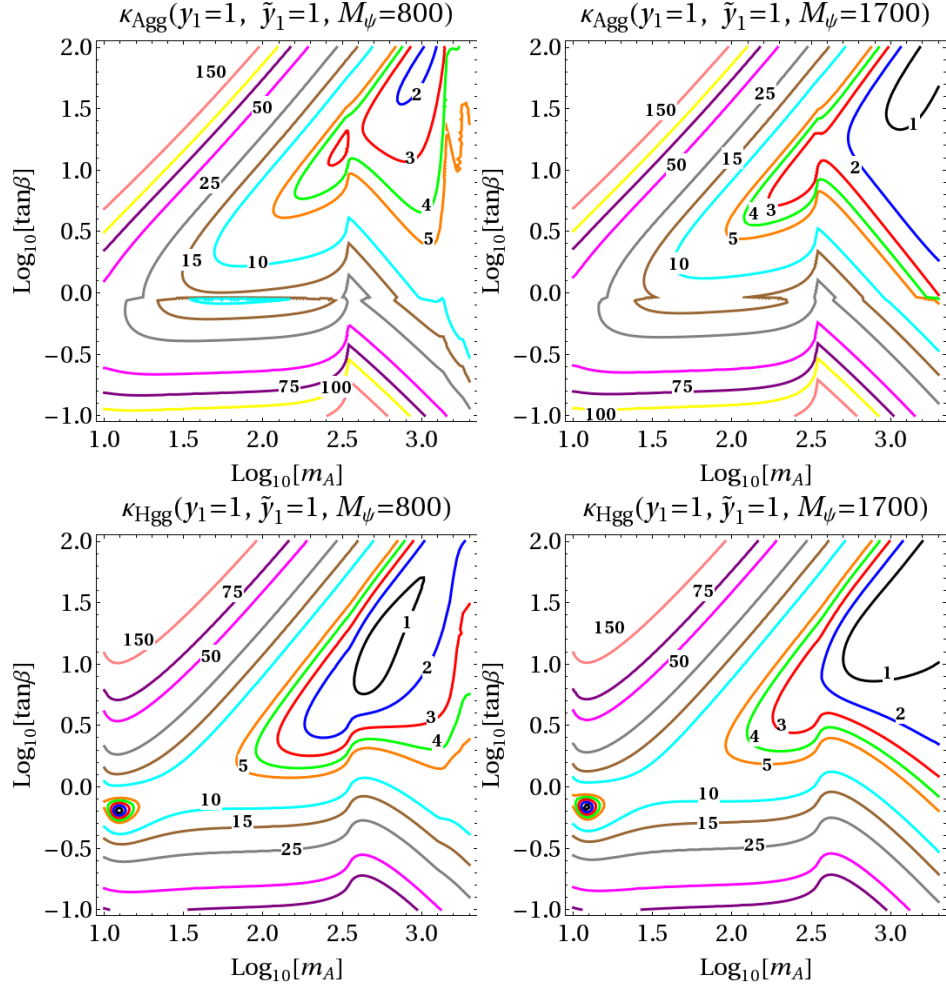


Figure 6.2.10: Contours of $\kappa_{A_{gg}}$ (top) and $\kappa_{H_{gg}}$ (bottom) for $y_1 = 1$, $\tilde{y}_1 = 1$, for $M_\psi = M_\chi = 800$ GeV (left) and 1700 GeV (right) for $MVQU_{12}$ model.

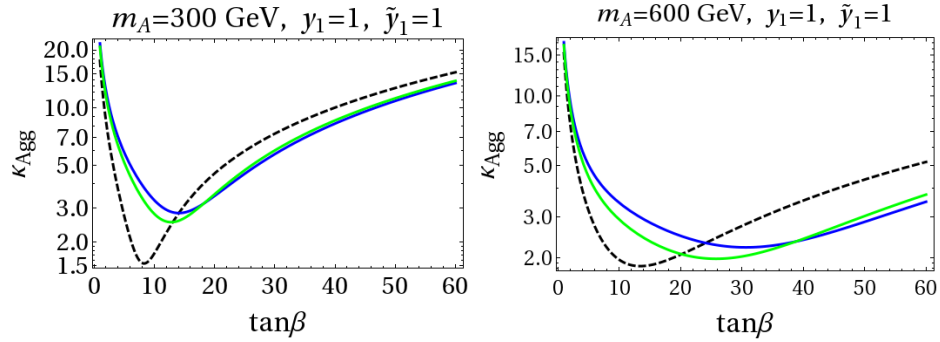


Figure 6.2.11: $\kappa_{A_{gg}}$ with $\tan\beta$ for $m_A = 300$ GeV (left) and 600 GeV (right) with $y_1 = 1$, $\tilde{y}_1 = 1$ and $M_\psi = 800$ GeV (blue), 1000 GeV (green) for $MVQU_{12}$ model and 2HDM-II (dashed-black).

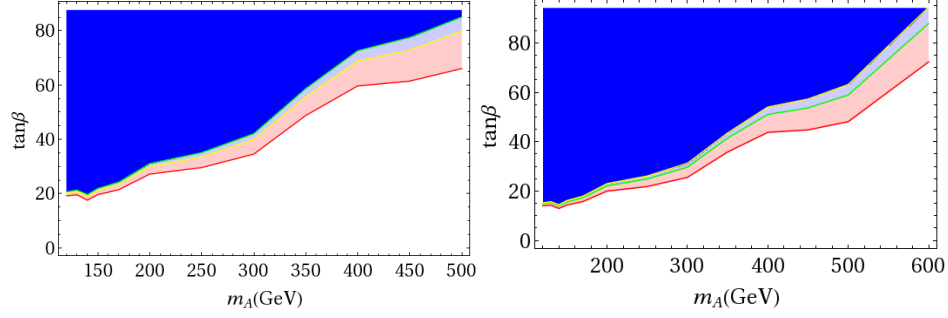


Figure 6.2.12: For $MVQU_{12}$ model, regions of the m_A - $\tan\beta$ parameter-space excluded at the 95% CL from $\phi \rightarrow \tau^+\tau^-$ decay when only A is present (left), and when A and H are degenerate and both present (right), with $y_1 = \tilde{y}_1 = 1$, $M_\psi = M_\chi = 800$ GeV (dark-blue region), 1000 GeV (light-blue and dark-blue regions). All shaded regions are excluded in the 2HDM-II.

similar to our results here. We introduce a doublet VLQ $\psi = (\psi_1, \psi_2)$ with hypercharge Y_ψ , and a singlet VLQ (χ) with hypercharge $(Y_\psi - 1/2)$ which couples only to Φ_1 . To the 2HDM-X Lagrangian we add

$$\mathcal{L} \supset \bar{\psi}i\not{D}\psi + \bar{\chi}i\not{D}\chi - (y_1\bar{\psi}_L\Phi_1\chi_R + \tilde{y}_1\bar{\psi}_R\Phi_1\chi_L + \text{h.c.}) - M_\psi\bar{\psi}\psi - M_\chi\bar{\chi}\chi. \quad (6.3.1)$$

After EWSB ψ_2 and χ mix to give two mass eigenstates ζ_1, ζ_2 . Since the VLQs couple to the Φ_1 in the same way as in $MVQD_{11}$ model, the mixing angles and the mass eigenstates are identical to those of $MVQD_{11}$ and can be read off from Eqs. (6.2.19) and (6.2.20) respectively. The gauge interactions of ζ_i and the $\phi\zeta_i\zeta_j$ couplings also remains the same as in $MVQD_{11}$ model and can be read off from Eqs. (6.2.30) and (6.2.31). In Fig. 6.3.1 we show $\text{BR}(A \rightarrow VV)$ including the VLF contributions for the $MVQDX_{11}$ model, and the tree-level $\text{BR}(A \rightarrow \tau^+\tau^-, b\bar{b}, t\bar{t})$ is unchanged from what are shown in Fig. 6.1.4 $\text{BR}(A \rightarrow \gamma\gamma, Z\gamma)$ for $\tan\beta = 1$, $y_1 = 0.5$, $\tilde{y}_1 = 1$ are almost identical to the 2HDM values shown in Fig. 6.2.5 and are therefore not shown explicitly in Fig. 6.3.1. For $\tan\beta = 30$, $\text{BR}(A \rightarrow \gamma\gamma, Z\gamma)$ is increased compared to 2HDM-II, because for large $\tan\beta$, $\Gamma(A \rightarrow b\bar{b})$ becomes much smaller in 2HDM-X.

In Fig. 6.3.2 we plot contours of $\kappa_{A_{gg}}$ and $\kappa_{H_{gg}}$. The $\kappa_{\phi_{gg}}$ contours in 2HDM-X (without VLFs) are shown in Fig. 6.1.5. Using these plots, one can read off $\sigma(gg \rightarrow A)$ for 8 TeV and

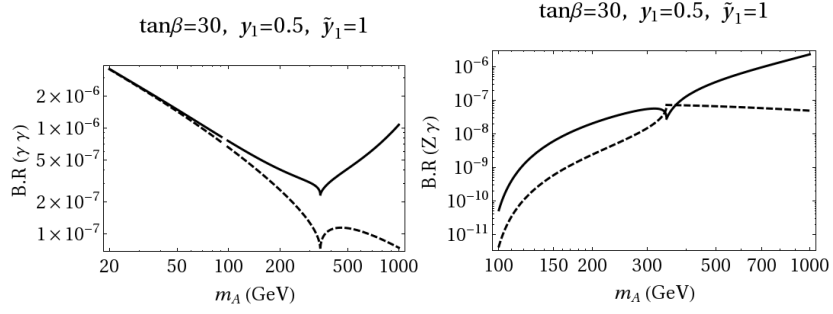


Figure 6.3.1: $\text{BR}(A \rightarrow \gamma\gamma, Z\gamma)$ with $M_\psi = M_\chi = 1000$ GeV (solid-black) for $\tan\beta = 30$ for the $MVQDX_{11}$ model, and the corresponding variation in the 2HDM-X (dashed-black).

14 TeV LHC from Fig. 3.1.1 in Chapter 3. As expected, for large $\tan\beta$, $\kappa_{A\gamma\gamma}$ is significantly larger in this model compared to 2HDM-X since the VLFs contribute substantially while the SM quark contributions alone are very small. In order to show explicitly how large the change is, we plot $\kappa_{A\gamma\gamma}$ as a function of $\tan\beta$ for $m_A = 300$ GeV and 600 GeV in Fig. 6.3.3.

6.4 2HDM-II with VLL-VLL Yukawa couplings

In this section we investigate the scenario in which we add vector-like leptons instead of VLQs. We introduce one doublet VLL (ψ) with hypercharge, Y_ψ and one singlet VLL (χ) with hypercharge, $Y_\psi - 1/2$. The Lagrangian we consider is exactly the same as in Eq. (6.2.16), except here the VLLs ψ and χ do not couple to gluons. Although vector-like leptons do not contribute in $gg \rightarrow A$, they contribute in $A \rightarrow \gamma\gamma, Z\gamma$. As an example, we choose $Y_\psi = -1/2$ and plot $\text{BR}(A \rightarrow \gamma\gamma)$ as a function of m_A in Fig. 6.4.1, with $M_\psi = M_\chi = 500$ GeV, for $\tan\beta = 1$ and 30. We see that the effect of VLLs is qualitatively similar to vector-like quarks; for low $\tan\beta$ the effect of VLLs is negligible while for large $\tan\beta$ and large m_A VLL contributions are significant. Near $m_A = 1000$ GeV, the VLL contribution is quite large due to them going onshell for our choice of VLL mass of 500 GeV (see Fig. A.0.2 in Appendix A). $\text{BR}(A \rightarrow Z\gamma)$ will show the same behavior and we do not show this explicitly.

To summarize, we considered several effective theories which has a 2HDM with VLFs also present. We presented the 2-body branching ratios of the neutral scalars H, A and the

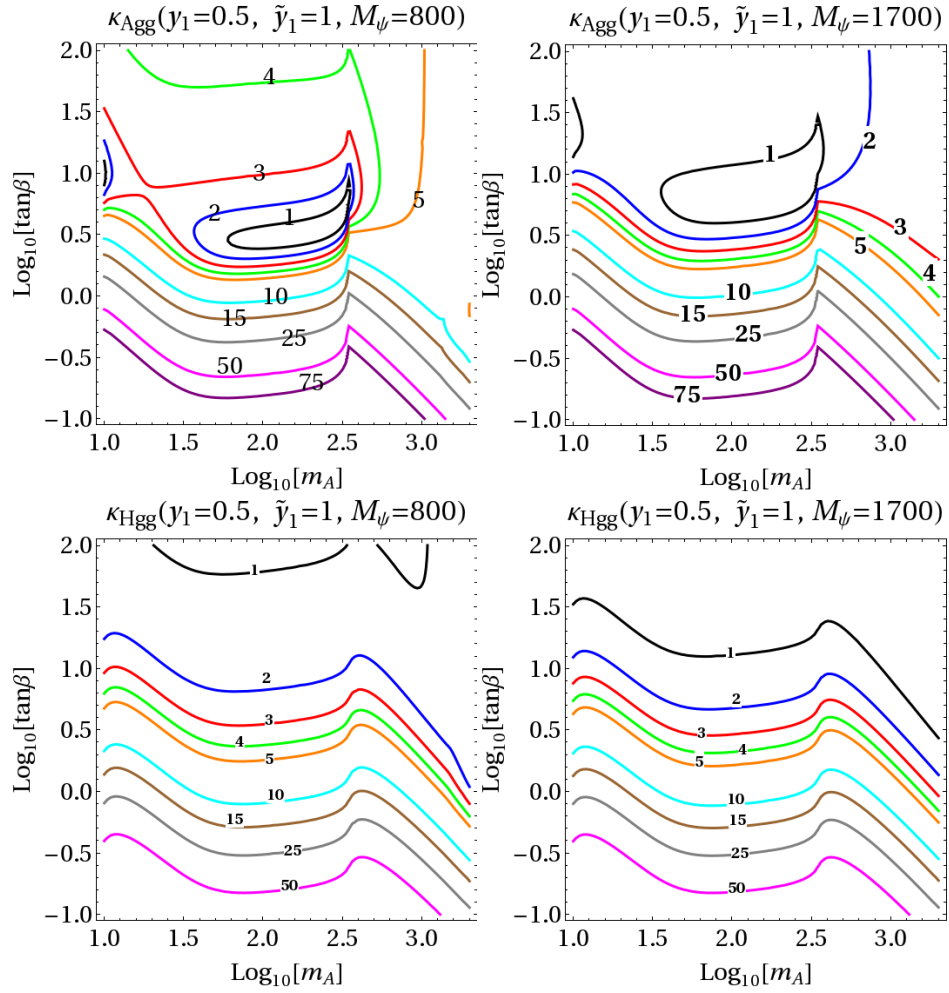


Figure 6.3.2: Contours of $\kappa_{A_{gg}}$ (top) and $\kappa_{H_{gg}}$ (bottom) for $y_1 = 0.5$, $\tilde{y}_1 = 1$, for $M_\psi = M_\chi = 800$ GeV (left) and 1700 GeV (right) for $MVQDX_{11}$ model.

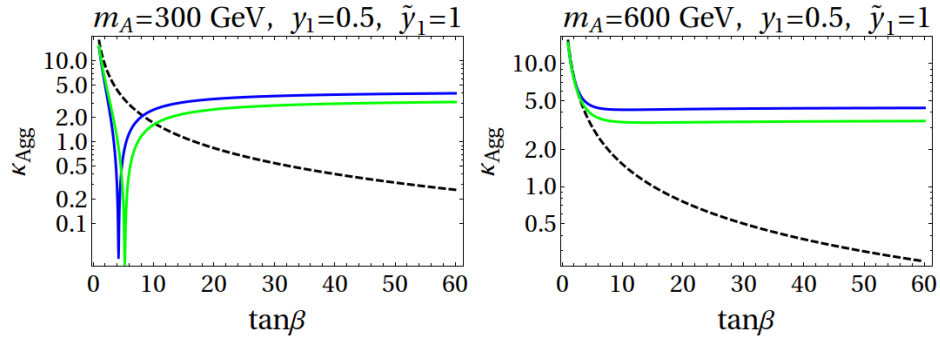


Figure 6.3.3: $\kappa_{A_{gg}}$ with $\tan\beta$ for $m_A = 300$ GeV (left) and 600 GeV (right) with $y_1 = 0.5$, $\tilde{y}_1 = 1$ and $M_\psi = 800$ GeV (blue), 1000 GeV (green) for $MVQDX_{11}$ model and 2HDM-II (dashed-black).

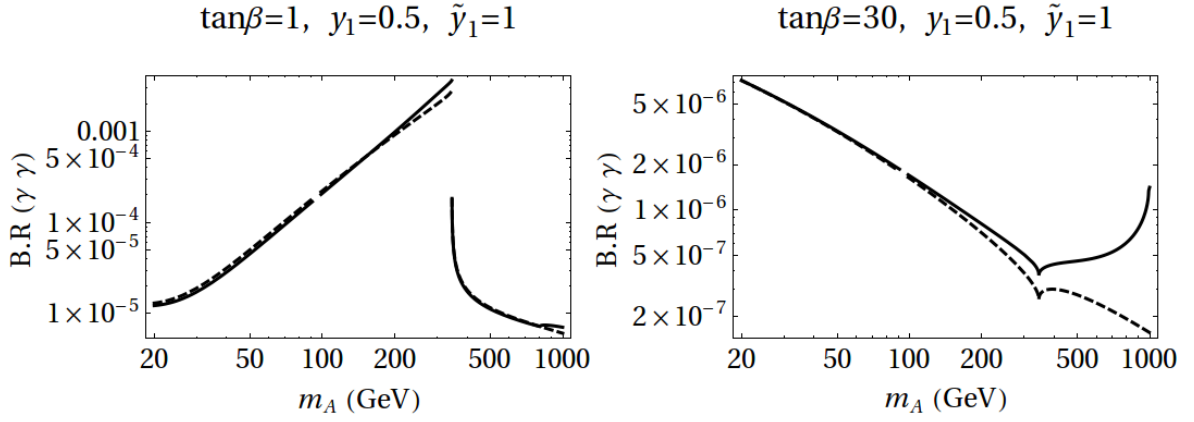


Figure 6.4.1: $BR(A \rightarrow \gamma\gamma)$ with $M_\psi = M_\chi = 500$ GeV, $y_1 = 0.5$, $\tilde{y}_1 = 1$ for $\tan\beta = 1$ (left) and $\tan\beta = 30$ (right) for $MVLE_{11}$ model.

effective ϕgg couplings in each of these models. We found that the VLFs can modify the $BR(A \rightarrow VV)$ and $\kappa_{\phi gg}$ significantly compared to the 2HDM with SM fermions only. Using these effective couplings one can calculate the 8 TeV and 14 TeV LHC $\sigma(gg \rightarrow \phi)$. We also discussed the constraints on the parameter space from the 8 TeV LHC $\phi \rightarrow \tau\tau$ results. We found one particular model in which the constraints on the parameter space is relaxed due to addition of VLFs. Our analysis should be applicable to many realistic BSM theories which has a 2HDM structure and also VLFs.

Chapter 7

Diphoton rates in 2HDM and a singlet scalar model

This chapter is based on the work done in Ref. [12]. In this chapter we analyze the 13 TeV LHC $\sigma(pp \rightarrow \phi \rightarrow \gamma\gamma)$ for a scalar (ϕ) coupled to the SM fermions and new vector-like fermions. As before we will assume that this scalar is produced via the gluon fusion process. We first perform a model independent analysis to obtain the 13 TeV LHC $\sigma(pp \rightarrow \phi \rightarrow \gamma\gamma)$ as a function of effective ϕgg and $\phi\gamma\gamma$ couplings. We also perform a model independent analysis of the 8 TeV LHC constraints and the perturbative unitarity constraints. We then consider few specific models namely the 2HDM-II, X, I and a singlet scalar model. For each of these models we obtain the 13 TeV LHC $\sigma(pp \rightarrow \phi \rightarrow \gamma\gamma)$ and the constraints on the parameters space from the 8 TeV LHC results and the perturbative unitarity.

Earlier, both the ATLAS and the CMS had reported an excess in the di-photon channel at an invariant mass of about 750 GeV [1, 2]. The predicted $\sigma(pp \rightarrow \phi) \times BR(\phi \rightarrow \gamma\gamma)$ were 10 ± 3 fb at ATLAS and 3.75 ± 1.2 fb at CMS with both the 8 TeV and 13 TeV LHC data combined. The best-fit width of these resonance was $\Gamma_\phi \approx 45$ GeV at ATLAS and $\Gamma_\phi \approx 0.1$ GeV at CMS. However, recent results from both ATLAS and CMS indicate that the presupposed excess was a statistical fluctuation [141, 142]. In this work we also present from our publication [12], the regions of parameter space which could have explained the di-photon excess.

7.1 Model Independent analysis

In this section we present a model independent analysis of a general scalar ϕ coupled to the SM and vector-like fermions. We consider the following effective Lagrangian

$$\mathcal{L} \supset -\frac{y_\psi}{\sqrt{2}}\phi\bar{\psi}\psi - \frac{y_f}{\sqrt{2}}\bar{f}_L H f_R - \frac{y'_f}{\sqrt{2}}\phi\bar{f}f - \frac{\kappa_{\phi hh}M_\phi}{2\sqrt{2}}\phi h^2 - m_\psi\bar{\psi}\psi + h.c., \quad (7.1.1)$$

where f denotes the SM fermions and ψ collectively denotes the new vector-like quarks (Q) or leptons (L). We present the $\sigma(pp \rightarrow \phi \rightarrow \gamma\gamma)$ at 13 TeV in terms of the effective ϕgg and $\phi\gamma\gamma$ couplings. We also present the constraints on y_ψ from the 8 TeV LHC results and the unitarity constraints.

7.1.1 13 TeV LHC $\sigma(gg \rightarrow \gamma\gamma)$

In this section we present the the 13 TeV LHC $\sigma(gg \rightarrow \phi \rightarrow \gamma\gamma)$ as a function of effective ϕgg and $\phi\gamma\gamma$ couplings for different values of ϕ width. As in Chapter 3 we work with the narrow width approximation (NWA) $\sigma(gg \rightarrow \phi \rightarrow \gamma\gamma) \approx \sigma(gg \rightarrow \phi) * BR(\phi \rightarrow \gamma\gamma)$ and obtain $\sigma(gg \rightarrow \phi)$ from $\sigma(gg \rightarrow \phi_{SM})$ via the relation in Eq. (3.1.1). The cross sections for the 14 TeV LHC $\sigma(gg \rightarrow \phi_{SM})$ is given in Ref. [32] for M_ϕ up to 1000 GeV. To get the approximate 13 TeV LHC $\sigma(gg \rightarrow \phi_{SM})$ we scale down the 14 TeV $\sigma(gg \rightarrow \phi_{SM})$ numbers by 10%. In order to get an approximate analytical form of the $\sigma(gg \rightarrow \phi_{SM})$ we fit a curve to the 13 TeV LHC $\sigma(gg \rightarrow \phi_{SM})$ numbers. We take the following functional form for the 13 TeV LHC $\sigma(gg \rightarrow \phi_{SM})$:

$$\begin{aligned} \sigma(gg \rightarrow \phi_{SM}) &= 8.7 \times e^{\frac{400-M_\phi}{133}} \text{ for } 400 < M_\phi < 700 \text{ GeV} \\ &= 0.922 \times e^{\frac{700-M_\phi}{163}} \text{ for } 700 < M_\phi < 1000 \text{ GeV.} \end{aligned} \quad (7.1.2)$$

In Fig. 7.1.1 we plot the 13 TeV LHC $\sigma(gg \rightarrow \phi \rightarrow \gamma\gamma)$ as obtained from 7.1.2. The cross sections for the 13 TeV LHC $\sigma(gg \rightarrow \phi \rightarrow \gamma\gamma)$ obtained from Ref. [32] is also shown in

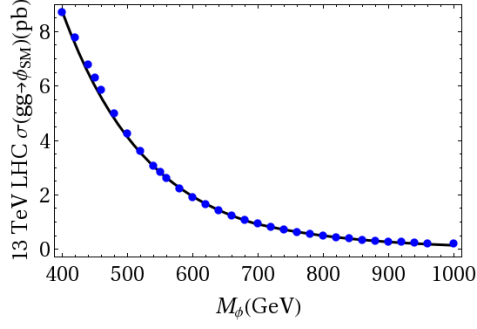


Figure 7.1.1: 13 TeV LHC $\sigma(gg \rightarrow \phi \rightarrow \gamma\gamma)$ (in fb) with M_ϕ as obtained from Eq. 7.1.2. The 13 TeV LHC $\sigma(gg \rightarrow \phi \rightarrow \gamma\gamma)$ cross sections obtained from Ref. [32] is shown by the blue dots.

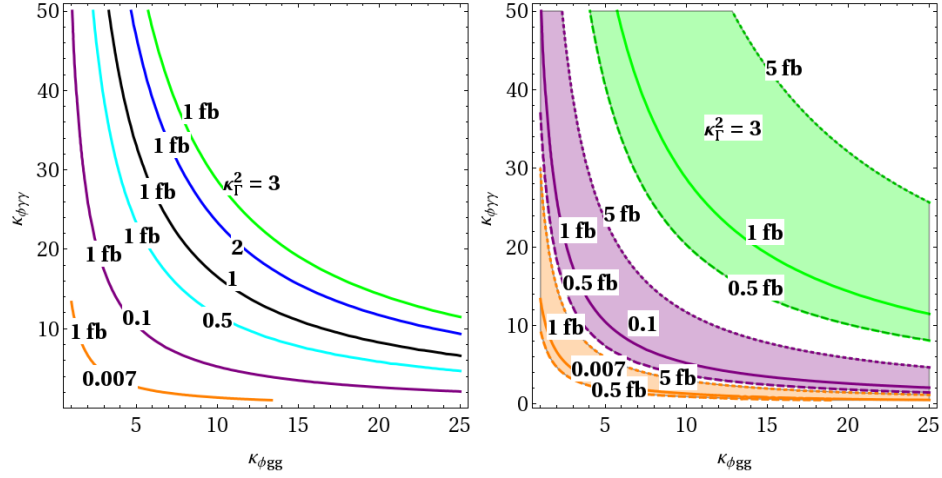


Figure 7.1.2: For $M_\phi = 750$ GeV, contours of 13 TeV LHC $\sigma(gg \rightarrow \phi \rightarrow \gamma\gamma)$ (in fb) (top left and bottom) and the regions $0.5 < \sigma(gg \rightarrow \phi \rightarrow \gamma\gamma) < 5$ fb (top right) and $4 < \sigma(gg \rightarrow \phi \rightarrow \gamma\gamma) < 10$ fb for various κ_Γ^2 shown.

Fig. 7.1.1 by the blue dots. We write ϕ width (Γ_ϕ) as

$$\Gamma_\phi = \frac{\kappa_\Gamma^2}{16\pi} M_\phi, \quad (7.1.3)$$

where κ_Γ^2 include the ϕ couplings and the phase space factors for all the relevant processes. As the benchmark point we chose $M_\phi = 750$ GeV. In Fig. 7.1.2 we plot contours of $\sigma(\phi) \times BR(\gamma\gamma)$ and the region $0.5 < \sigma(gg \rightarrow \phi \rightarrow \gamma\gamma) < 5$ fb as a function of $\kappa_{\phi gg}$ and $\kappa_{\phi\gamma\gamma}$ for various κ_Γ^2 .

7.1.2 8 TeV LHC constraints

If the $\phi tt, \phi \tau \tau$ couplings $y'_{t,\tau}$ and $\kappa_{\phi hh}$ couplings in Eq. (7.1.1) are nonzero then $\phi \rightarrow tt, \tau \tau, hh$ (collectively called XX) decays are possible and 8 TeV LHC $\phi \rightarrow tt, \tau \tau, hh$ results [6, 7, 11] can put constraints on $y'_{t,\tau}, y_Q$ and $\kappa_{\phi hh}$. In this section we analyze these constraints.

In the NWA we have

$$\begin{aligned}\sigma(gg \rightarrow \phi \rightarrow XX) &= \sigma(gg \rightarrow \phi) \times BR(\phi \rightarrow XX) \\ &= \sigma(gg \rightarrow \phi) \times \frac{\Gamma(\phi \rightarrow XX)}{\Gamma_{\text{tot}}}.\end{aligned}\quad (7.1.4)$$

Using Eq. 3.1.3 in Chapter 3 $\sigma(gg \rightarrow \phi)$ can be written as

$$\sigma(gg \rightarrow \phi) = \sigma(gg \rightarrow \phi_{SM}) \times \frac{\kappa_{\phi gg}^2}{\kappa_{\phi_{SM} gg}^2} \quad (7.1.5)$$

which can be written using the expressions for $\kappa_{\phi gg}$ in Appendix A as

$$\sigma(gg \rightarrow \phi) = \sigma(gg \rightarrow \phi_{SM}) \times \frac{y_\psi}{y_t} \frac{F_{1/2}(r_\psi)}{F_{1/2}(r_t)} \frac{m_t}{m_\psi}. \quad (7.1.6)$$

The $\Gamma(\phi \rightarrow ff)$ are given by

$$\Gamma(\phi \rightarrow ff) = \frac{N_c}{16\pi} (y'_f)^2 m_\phi (1 - 4r_f)^{n/2}, \quad (7.1.7)$$

where $n=1$ and 3 for CP-odd and CP-even scalar respectively. The $\Gamma(\phi \rightarrow hh)$ is given by

$$\Gamma(\phi \rightarrow hh) = \frac{\kappa_{\phi hh}^2}{4} \left(1 - 4\frac{m_h^2}{M_h^2}\right)^{\frac{1}{2}}. \quad (7.1.8)$$

Let $\kappa_{\phi gg(X)}^{max}$ be the value of $\kappa_{\phi gg}$ for which the $\sigma(pp \rightarrow \phi \rightarrow XX)$ reaches its upper limit from the 8 TeV LHC $\phi \rightarrow XX$ results. Then an upper bound on y_Q, y'_f and $\kappa_{\phi hh}^2$ can be

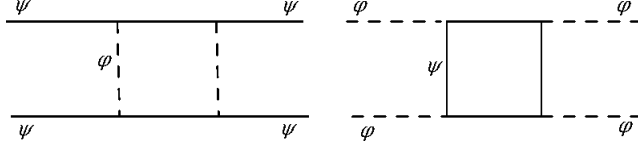


Figure 7.1.3: Feynman diagram for the processes $\psi\psi \rightarrow \psi\psi$ and $\phi\phi \rightarrow \phi\phi$.

obtained from

$$\left| \sum_Q \frac{y'_Q}{y_t} \frac{F_{1/2}(r_Q)}{F_{1/2}(r_t)} \frac{m_t}{m_\psi} \right|^2 \times \frac{\kappa_X^2}{\kappa_\Gamma^2} < \left(\frac{\kappa_{\phi gg(X)}^{max}}{\kappa_{\phi SM gg}} \right)^2, \quad (7.1.9)$$

where κ_X^2 is related to the partial $\phi \rightarrow XX$ width via $\kappa_X^2 = 16\pi\Gamma(\phi \rightarrow XX)/M_\phi$. The $\kappa_{\phi gg(X)}^{max}$ for $\phi \rightarrow tt, \tau\tau, \gamma\gamma$ channels can be found in Chapter 3.

7.1.3 Unitarity constraints

In this section we obtain the constraints on the Yukawa couplings (y_ψ) from the perturbative unitarity of $\psi\psi \rightarrow \psi\psi$ and $\phi\phi \rightarrow \phi\phi$ processes. We consider the loop level processes given by the diagrams shown in Fig. 7.1.3. We first consider the process $\psi\psi \rightarrow \psi\psi$. We expand the amplitudes (a_l) in partial waves as

$$\mathcal{M}(\cos\theta) = 16\pi \sum_l (2l+1) a_l P_l(\cos\theta). \quad (7.1.10)$$

A necessary condition for perturbative unitarity is $\text{Im}(a_l) < 1$ [24]. By optical theorem, the imaginary part of any scattering amplitude $\text{Im}[\mathcal{M}(\psi\psi \rightarrow \psi\psi)]$ is related to the total cross-section $\sigma(\psi\psi \rightarrow \phi\phi)$ via the relation

$$\text{Im}\mathcal{M}[\psi(p_1)\psi(p_2) \rightarrow \psi(p_1)\psi(p_2)] = 2E_{CM}P_{CM}\sigma[\psi(p_1)\psi(p_2) \rightarrow \phi(k_1)\phi(k_2)] \quad (7.1.11)$$

The Feynman diagram for the $\psi\psi \rightarrow \phi\phi$ process is shown in Fig. 7.1.4. In the CM frame we parametrize the momenta as

$$\begin{aligned} p_1 &= (E_\psi, 0, 0, p_\psi), p_2 = (E_\psi, 0, 0, -p_\psi) \\ k_1 &= (E_\phi, 0, 0, p_\phi \cos \theta), k_2 = (E_\phi, 0, 0, -p_\phi \cos \theta). \end{aligned} \quad (7.1.12)$$

In the CM frame the differential cross section is given by

$$\frac{d\sigma}{d\cos\theta} = \frac{(1-2r_\phi)^{1/2}}{32\pi s} \frac{1}{4} |\mathcal{M}|^2 \quad (7.1.13)$$

where $r_\phi = m_\phi^2/2E_\psi^2$ and

$$|\mathcal{M}|^2 = y_\psi^4 \frac{(1-2r_\phi)(1-\cos^2\theta)}{2(1-r_\phi-\sqrt{1-2r_\phi}\cos\theta)^2}. \quad (7.1.14)$$

Collecting all the terms we have

$$\frac{d\sigma}{d\cos\theta} = \frac{y_\psi^4}{128\pi s} \tilde{f}(\cos\theta) \quad (7.1.15)$$

where

$$\tilde{f}(\cos\theta) = \frac{(1-2r_\phi)^{3/2}(1-\cos^2\theta)}{2(1-r_\phi-\sqrt{1-2r_\phi}\cos\theta)^2}. \quad (7.1.16)$$

For $E_\psi \gtrsim m_\phi$ the integration of $\tilde{f}(\cos\theta)$ over $\cos\theta$ gives ≈ 1 and hence $\sigma \simeq y_\psi^4/(128\pi s)$. To get a conservative bound we assume that $\mathcal{M}(\psi\psi \rightarrow \psi\psi)$ is dominated by the $l=0$ partial wave. Using Eq. (7.1.10) and Eq. (7.1.11) we obtain $\text{Im}(a_0) = y_\psi^4 (4 \times (16\pi)^2) < 1$ which gives $y_\psi < 10$. For the $\phi\phi \rightarrow \phi\phi$ process shown in Fig. 7.1.3 we obtain a similar result for the $\mathcal{M}(\phi\phi \rightarrow \phi\phi)$ but multiplied by the color factor (N_c) due to the fermions running in the loop. Therefore the bound on y_ψ from the $\phi\phi \rightarrow \phi\phi$ process is given by $y_\psi N_c^{1/4} < 10$.

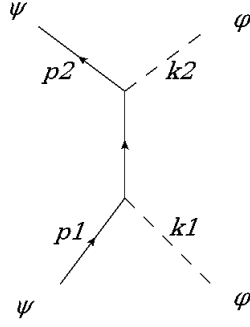


Figure 7.1.4: Feynman diagram for the process $\psi\psi \rightarrow \phi\phi$.

7.2 Diphoton rates in the 2HDM and a singlet scalar model

In this section we consider few specific models. We present the 13 TeV LHC $\sigma(gg \rightarrow \phi \rightarrow \gamma\gamma)$ for each of these models and present the constraints on the parameter space from the 8 TeV LHC results and the unitarity constraint. We first consider the case where ϕ is one or both of the 2HDM scalars coupled to VLFs and then consider a model where ϕ is an SU(2) singlet coupled to VLFs. In the 2HDM we consider the types II, X and I. For the 2HDM we consider two scenarios, one in which $M_A \gg M_H$ so that only the H contribute to $\sigma(gg \rightarrow \phi \rightarrow \gamma\gamma)$ and one in which M_H, M_A are within the experimental resolution in which case both the A, H contribution has to be included in $\sigma(gg \rightarrow \phi \rightarrow \gamma\gamma)$. As discussed in Chapter 3, because of different CP properties of H and A their sum is incoherent i.e $\sigma(gg \rightarrow \phi \rightarrow \gamma\gamma) = \sigma(gg \rightarrow H \rightarrow \gamma\gamma) + \sigma(gg \rightarrow A \rightarrow \gamma\gamma)$.

7.2.1 Two Higgs doublet model

In this section we obtain the 13 TeV LHC $\sigma(gg \rightarrow \phi \rightarrow \gamma\gamma)$ for the scalars of 2HDM-II, X and I. As our benchmark points we take $M_H = 750$ GeV for the case when only the H contribute and $M_H = 735$ GeV $M_A = 750$ GeV when both the H and A contribute. Our results are not very sensitive to the mass splitting of H and A . For the 2HDM-II we analyze the situation

where only the SM fermions (SMF) are present and subsequently we analyze the scenario where we introduce new vector-like fermions. For 2HDM-X and I we present our results only for the scenario with SMF and VLFs since for 2HDM-X and I the SM contribution to the $\kappa_{\phi VV}$ are small. We show our results only for SM-like charge assignments. For other charge assignments one can scale our results by Q_f^4 .

2HDM type-II

We already discussed 2HDM type-II in Chapter 5. We restrict ourselves to the 2HDM alignment limit. We recall that in 2HDM-II all the up-type SM fermions couple to the A as $\cot\beta$ while all the down-type fermions couple as $\tan\beta$ and in the alignment limit the H couples in the same way as A . It follows that κ_{Γ}^2 can not be made arbitrarily small in this model; the minimum occurs at $\tan\beta \simeq 5.7$ corresponding to $\kappa_{\Gamma}^2 = 0.12$ when only H contribute, and 0.24 when both H and A contribute. Any value of κ_{Γ}^2 (other than 0.24) can be realized by two values of $\tan\beta$; one for $\tan\beta < 5.7$ and the other for $\tan\beta > 5.7$.

2HDM + SMF only:

We first consider the case when only the H contributes to $\sigma(gg \rightarrow \phi \rightarrow \gamma\gamma)$. In this case we have $\kappa_{\Gamma}^2 = 3$ and $\sigma * BR_{\gamma\gamma} \simeq 0.002$ fb for $\tan\beta = 0.83$. Next we consider the case when both H and A contribute. As mentioned earlier we take $M_H = 735$ GeV and $M_A = 750$ GeV. In Fig. 7.2.1 we plot $\sigma(gg \rightarrow \phi \rightarrow \gamma\gamma)$ vs. κ_{Γ}^2 obtained by varying $\tan\beta$. The two branches of $\sigma * BR_{\gamma\gamma}$ in Fig. 7.2.1 correspond to two values of $\tan\beta$ that gives the same κ_{Γ}^2 . The upper branch for which $\tan\beta < 5.7$ has larger cross sections because of the larger contribution from the top.

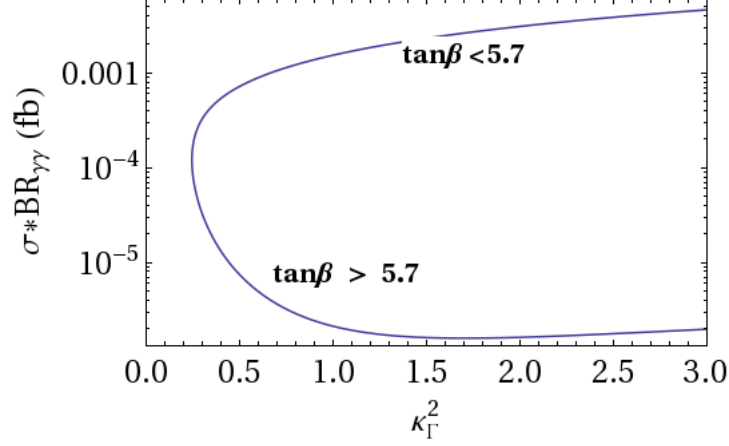


Figure 7.2.1: 13 TeV LHC $\sigma(gg \rightarrow \phi \rightarrow \gamma\gamma)$ (in fb) vs. κ_{Γ}^2 for $M_H = 735$ GeV, $M_A = 750$ GeV .

2HDM-II + SMF + VLL:

We add one doublet VLL ψ^l with hypercharge Y_{ψ^l} , and one singlet VLL χ with hypercharge $(Y_{\psi^l} - 1/2)$. To the 2HDM-II Lagrangian we add

$$\mathcal{L} \supset \bar{\psi}^l i \not{D} \psi^l + \bar{\chi} i \not{D} \chi - (y_1^l \bar{\psi} \Phi_1 \chi_R + \text{h.c.}) - M_{\psi}^l \bar{\psi}^l \psi^l - M_{\chi} \bar{\chi} \chi. \quad (7.2.1)$$

This model is same as the $MVQD_{11}$ model in Chapter 6 with \tilde{y} set equal to zero. As in $MVQD_{11}$ model we define the mass eigenstates ζ_1^l and ζ_2^l . The mass eigen states, mixing angles and the effective $\phi \zeta_i^l \zeta_i^l$ couplings (y_{ij}^{ϕ}) can be obtained from those of the $MVQD_{11}$ model in Sec. 6.2.2. We take $Y_{\psi^l} = -1/2$ and choose the mass parameters of the VLLs such that the lighter mass eigenstates (ζ_2^l) of the charge -1 VLL is $M_{VL} = 375$ GeV. In Fig. 7.2.2 we plot $\sigma_{\phi} * BR_{\gamma\gamma}$ as a function of y_1^l for various values of $\{\tan\beta, \kappa_{\Gamma}^2\}$, and also the unitarity constraint from $\psi\psi \rightarrow \psi\psi$ process given by $\sqrt{2}(y_{22}^H + y_{22}^A) < 10$ as a red vertical line where.

2HDM-II+SMF+VLL+VLQ:

We introduce one doublet VLQ ψ^q with hypercharge Y_{ψ^q} , one singlet VLQ ξ with hypercharge $Y_{\psi^q} + 1/2$, one doublet VLL ψ^l with hypercharge Y_{ψ^l} , and one singlet VLL χ with

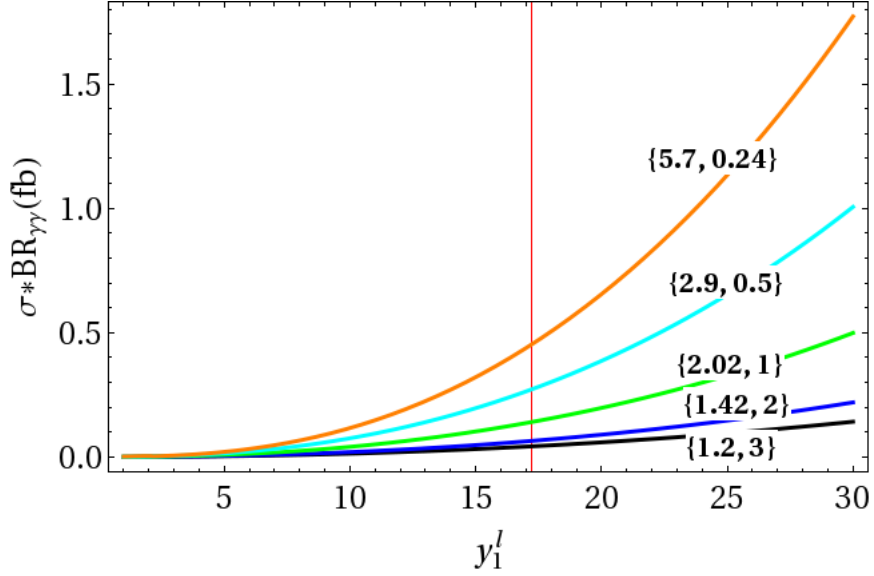


Figure 7.2.2: 13 TeV LHC $\sigma(gg \rightarrow \phi \rightarrow \gamma\gamma)$ (in fb) for $M_H = 735$ GeV, $M_A = 750$ GeV for 2HDM-II +VLL model. The region to the right of the red vertical $\psi\psi \rightarrow \psi\psi$ channel is shown by the red vertical line.

hypercharge ($Y_{\psi^l} - 1/2$). To the 2HDM-II Lagrangian we add

$$\begin{aligned} \mathcal{L} \supset & \bar{\psi}^l i \not{D} \psi^l + \bar{\chi} i \not{D} \chi - (y_1^l \bar{\psi} \Phi_1 \chi_R + \text{h.c.}) - M_{\psi^l} \bar{\psi}^l \psi^l - M_\chi \bar{\chi} \chi + \bar{\psi}^l i \not{D} \psi^l + \bar{\psi}^q i \not{D} \psi^q + \bar{\xi} i \not{D} \xi \\ & - (y_2^q \bar{\psi}_L^q \tilde{\Phi}_2 \xi_R + \text{h.c.}) - M_{\psi^q} \bar{\psi}^q \psi^q - M_\xi \bar{\xi} \xi. \end{aligned} \quad (7.2.2)$$

In this model the VLQ couplings are the same as in $MVQU_{22}$ model of Chapter 6 in Sec. 6.2.2 and the VLL couplings are the same as $MVQD_{11}$ model in section in Sec. 6.2.2. As before we define the mass eigenstates ζ_1^q, ζ_2^q for the VLQs and ζ_1^l, ζ_2^l for the VLLs. The mass eigenstates, mixing angles and the effective $\phi \zeta_i \zeta_j$ couplings (y_{ij}^ϕ) can be obtained from $MVQU_{12}$ for the VLQs and $MVQD_{11}$ model for the VLLs. We take $N'_c = 3$, $Y_{\psi^q} = 1/6$, $Y_{\psi^l} = -1/2$ and choose the mass parameters of the VLFs such that the lighter mass eigenstates (ζ_2^l) of the charge -1 VLLs has mass 375 GeV .

We first consider the case when only the H contributes to $\sigma(gg \rightarrow \phi \rightarrow \gamma\gamma)$. In Fig. 7.2.3 we plot contours of $\sigma(gg \rightarrow \phi \rightarrow \gamma\gamma) = 0.5$ fb in the $y_2^q - y_1^l$ plane with the VLQ mass parameter chosen so that the lightest VLQ mass eigenstate has mass $M_{\zeta_2^q} = 1200$ GeV. We also show in Fig. 7.2.3, the unitarity constraint on y_1^q, y_1^l from $\phi\phi \rightarrow \phi\phi$ (shown in solid red) and $\psi\psi \rightarrow \psi\psi$ (dashed red) channels given by the equations $[y_{22}^q (N'_c)^{1/4} + y_{22}^l] < 10$ and

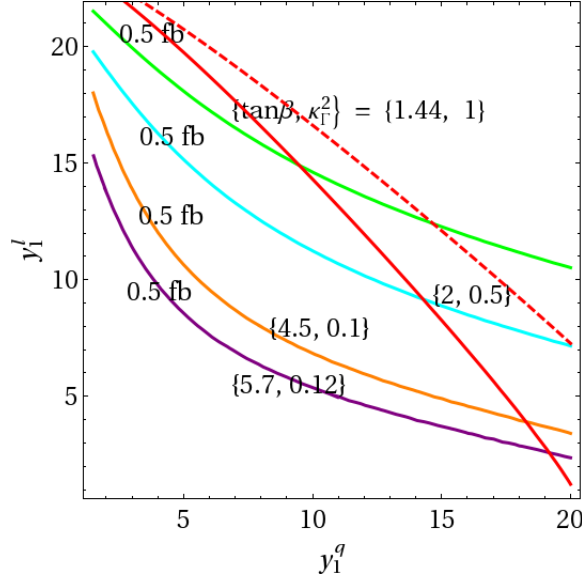


Figure 7.2.3: 13 TeV LHC $\sigma(gg \rightarrow \phi \rightarrow \gamma\gamma)$ (in fb) for $M_H = 750$ GeV in the 2HDM+VLL+VLQ model for $M_{\zeta_2^q} = 1200$ GeV $M_{VL} = 375$ GeV and unitarity constraints from $\phi\phi \rightarrow \phi\phi$ (solid red), $\psi\psi \rightarrow \psi\psi$ (dashed red)

$(y_{22}^q + y_{22}^l) < 10$ respectively, where y_{22}^q and y_{22}^l are the couplings of the H to the lighter VLQ and the lighter VLL respectively. In this case the 8 TeV LHC $\phi \rightarrow tt$ results do not put any additional constraints.

Next we consider the case when both the H and A contribute to $\sigma(gg \rightarrow \phi \rightarrow \gamma\gamma)$. In Fig. 7.2.4 we show the contours of $\sigma(gg \rightarrow \phi \rightarrow \gamma\gamma)$ and the region $0.5 < \sigma(gg \rightarrow \phi \rightarrow \gamma\gamma) < 5$ fb for $M_H = 735$, $M_A = 750$ GeV and $M_{\zeta_2^q} = 1200$ GeV for various κ_F^2 . The unitarity constraint from $\psi\psi \rightarrow \psi\psi$ is now $2^{1/4}[y_{22}^q + y_{22}^l] < 10$, since both the H and A contribute. In Fig. 7.2.4 we also show the unitarity constraints on y_1^q and y_1^l from $\phi\phi \rightarrow \phi\phi$ (solid red) and $\psi\psi \rightarrow \psi\psi$ (dashed red). The constraints on y_q from the 8 TeV LHC $\phi \rightarrow tt$ results are also shown in Fig. 7.2.4 by the red dots. In Fig. 7.2.5 we plot contours of $\sigma(gg \rightarrow \phi \rightarrow \gamma\gamma)$ in the $M_\phi - y^q$ plane obtained by saturating the unitarity bound $[y_{22}^q(N_c')^{1/4} + y_{22}^l] < 10$ and choosing $M_{VL} = M_\phi/2$ with $M_{\zeta_2^q} = 1200$ and 1500 GeV for $\tan\beta=5.7$ for which the maximum cross section occur. One can use this plot to estimate the largest possible cross section in this model. Because of saturating the unitarity constraint, for y^q small, y^l is large and therefore the $\kappa_{\phi gg}$ is small and the $BR(\phi \rightarrow \gamma\gamma)$ is large. On the other hand, for y^q large, y^l is small and therefore the $\kappa_{\phi gg}$ is large but $BR(\phi \rightarrow \gamma\gamma)$ is small. For this reasons there

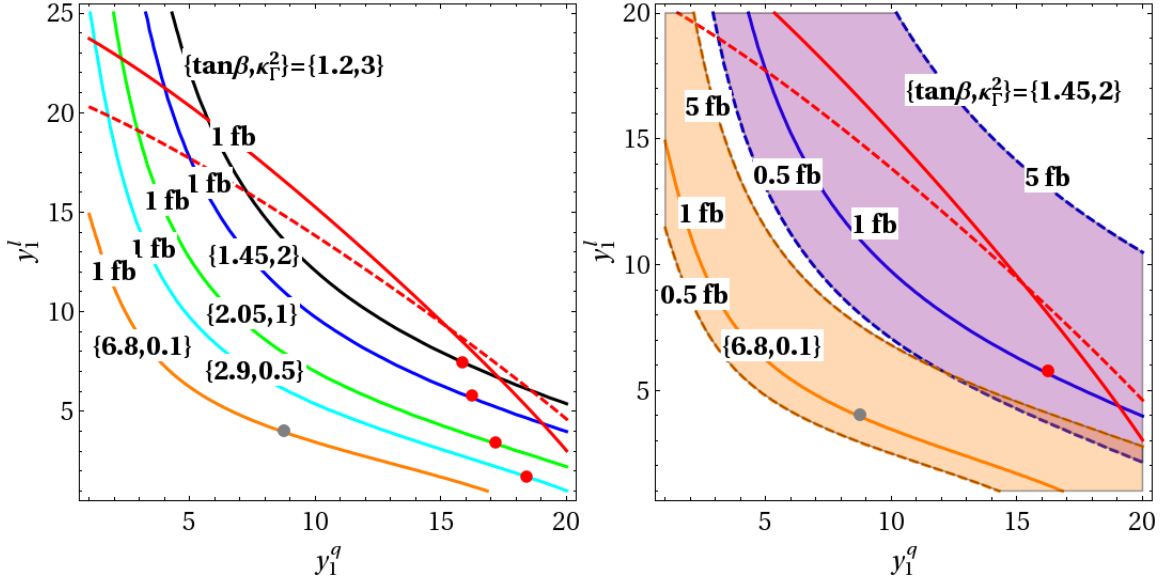


Figure 7.2.4: For 2HDM-X + VLL+VLQ model, contours of 13 TeV LHC $\sigma(gg \rightarrow \phi \rightarrow \gamma\gamma)$ (in fb) (left) and the region $0.5 < \sigma(gg \rightarrow \phi \rightarrow \gamma\gamma) < 5$ fb (right), for various κ_T^2 shown, for $M_H = 735$, $M_A = 750$ GeV, $M_{\zeta_2^q} = 1200$ GeV and $M_{VL} = 375$ GeV. To the right of the red dots and the gray dots are excluded from 8 TeV LHC $\phi \rightarrow tt$ data and the 8 TeV LHC $\phi \rightarrow \tau\tau$ data respectively.

are two values of y^q which gives the same $\sigma(gg \rightarrow \phi \rightarrow \gamma\gamma)$.

2HDM-X+VLFs:

We now move on to the 2HDM type-X. As discussed in Chapter 5, all the SM-quarks in this model couple to the H, A as $\cot\beta$, while all the SM-leptons couples as $\tan\beta$. As a result, the Γ_ϕ in this model is dominated by $\phi \rightarrow \tau\tau$ decay for large $\tan\beta$. Since m_τ is smaller than m_b , the Γ_ϕ can be smaller than that of the 2HDM-II. Specifically, the smallest $\kappa_T^2 \approx 0.028$ occurs for $\tan\beta = 11.5$.

We introduce VLQs and VLLs in the same way as in 2HDM-II. As before we start with considering only the H contribution. We first choose $M_{\zeta_2^q} = 1200$ GeV. In Fig. 7.2.6 we show contours of $\sigma(gg \rightarrow \phi \rightarrow \gamma\gamma)$ in the $y_1^q - y_1^l$ plane for various κ_T^2 , for $M_{\zeta_2^q} = 1200$ GeV and $M_H = 750$ GeV. We also show in Fig. 7.2.6 the unitarity constraints on y_1^q, y_1^q from $\phi\phi \rightarrow \phi\phi$ (solid red) and $\psi\psi \rightarrow \psi\psi$ (dashed red). As in the 2HDM-II case there are no constraints on y_1^q from the 8 TeV LHC $\phi \rightarrow tt$ results. However, for large $\tan\beta$, $\text{BR}(\phi \rightarrow \tau\tau)$ can be large in this model and the 8 TeV LHC $\phi \rightarrow \tau\tau$ puts an upper bound on y_1^q . For $\tan\beta = 11.5$ this

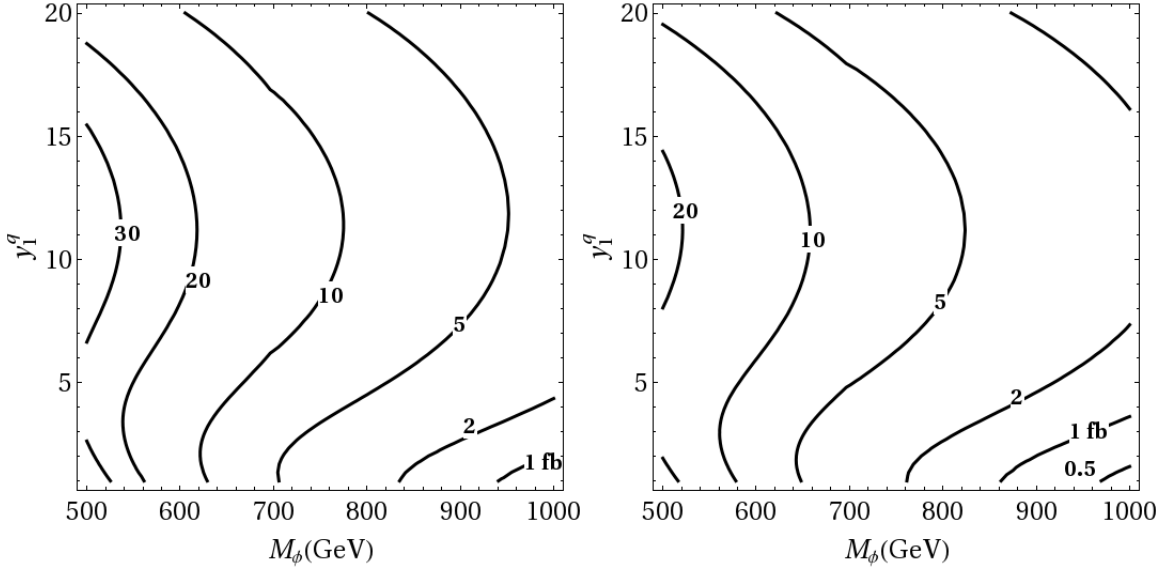


Figure 7.2.5: For 2HDM-II + VLL+VLQ model, contours of 13 TeV LHC $\sigma(gg \rightarrow \phi \rightarrow \gamma\gamma)$ (in fb) with y_1^l chosen to saturate the unitarity bound $[y_{22}^q(N_c')^{1/4} + y_{22}^l] < 10$ for $M_{VLL} = M_\phi/2$, $\tan\beta = 5.7$, $M_{\zeta_2^q} = 1200$ (left) and 1500 GeV (right).

bound is shown by the gray dot in Fig. 7.2.6.

We now consider the case when both the H and A contribute. We start with choosing $M_{\zeta_2^q} = 1200$ GeV. In Fig. 7.2.7 we show contours of $\sigma(gg \rightarrow \phi \rightarrow \gamma\gamma) = 1$ fb and region $0.5 < \sigma(gg \rightarrow \phi \rightarrow \gamma\gamma) < 5$ fb in the $y_1^q - y_1^l$ plane for $M_{\zeta_2^q} = 1200$ GeV, $M_H = 735$ and $M_A = 750$ GeV. We also show in Fig. 7.2.7 the unitarity constraints on y_1^q, y_1^l from $\phi\phi \rightarrow \phi\phi$ (solid red) and $\psi\psi \rightarrow \psi\psi$ (dashed red). The upper bounds on y_1^q from the 8 TeV LHC $\phi \rightarrow \tau\tau$ results and $\phi \rightarrow tt$ results are shown in red and gray dots respectively. In Fig. 7.2.8 we plot contours of $\sigma(gg \rightarrow \phi \rightarrow \gamma\gamma)$ in the $M_\phi - y^q$ plane obtained by saturating the unitarity bound $[y_{22}^q(N_c')^{1/4} + y_{22}^l] < 10$ and choosing $M_{VL} = M_\phi/2$, for $M_{\zeta_2^q} = 1200$ and 1500 GeV with $\tan\beta=6.8$ for which the maximum cross section occurs in the 2HDM-X

2HDM-I + VLFs:

Finally, we analyze the 2HDM type-I with VLFs. As discussed in Chapter 5, all the SM fermions couple to H, A as $\cot\beta$. The Γ_ϕ can be very small for large $\tan\beta$ and therefore the $\sigma(gg \rightarrow \phi \rightarrow \gamma\gamma)$ can be quite large in this model. We first discuss the case when only VLLs are introduced and subsequently discuss the case when both VLLs and VLQs are introduced.

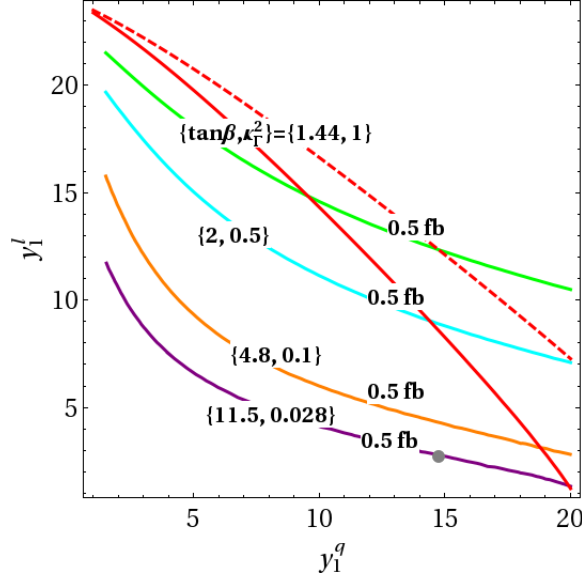


Figure 7.2.6: For 2HDM-X + VLL+VLQ model, contours of 13 TeV LHC $\sigma(gg \rightarrow \phi \rightarrow \gamma\gamma)$ (in fb) for various κ_T^2 shown, for $M_H = 750$, GeV for $M_{\zeta_2^q} = 1200$ GeV. Unitarity constraints from $\phi\phi \rightarrow \phi\phi$ and $\psi\psi \rightarrow \psi\psi$ are shown in solid red and dashed red respectively. The region to the right of the gray dots are excluded from the 8TeV LHC $\phi \rightarrow \tau\tau$ results.

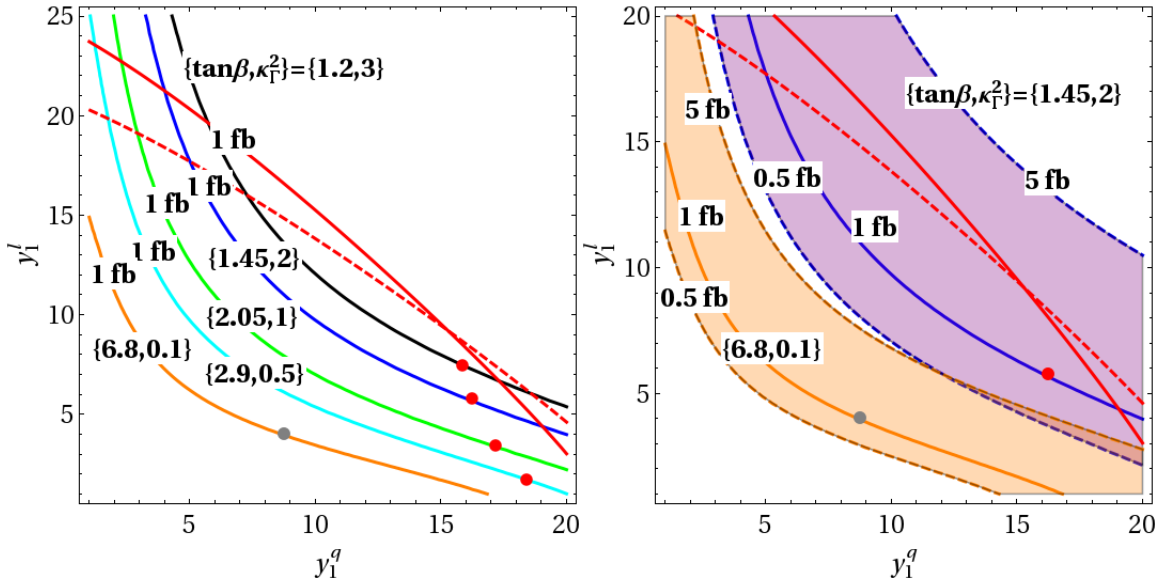


Figure 7.2.7: For 2HDM-X + VLL+VLQ model, contours of 13 TeV LHC $\sigma(gg \rightarrow \phi \rightarrow \gamma\gamma)$ (in fb) (left) and the region $0.5 < \sigma(gg \rightarrow \phi \rightarrow \gamma\gamma) < 5$ fb (right), for various κ_T^2 shown, for $M_H = 735$, $M_A = 750$ GeV, $M_{\zeta_2^q} = 1200$ GeV and $M_{VL} = 375$ GeV. To the right of the red dots and the gray dots are excluded from 8 TeV LHC $\phi \rightarrow tt$ data and the 8 TeV LHC $\phi \rightarrow \tau\tau$ data respectively.

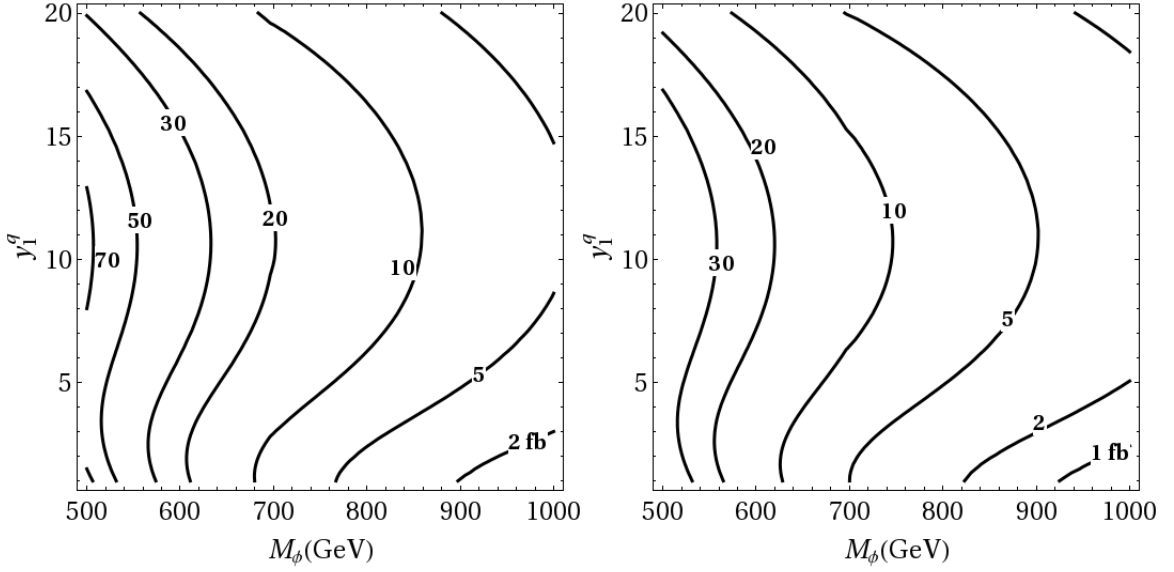


Figure 7.2.8: For 2HDM-X + VLL+VLQ model, contours of 13 TeV LHC $\sigma(gg \rightarrow \phi \rightarrow \gamma\gamma)$ (in fb) with y_1^l chosen to saturate the unitarity bound $[y_{22}^q(N_c')^{1/4} + y_{22}^l] < 10$ for $M_{VLL} = M_\phi/2$, $\tan\beta = 6.8$, $M_{\zeta_2^q} = 1200$ (left) and 1500 GeV (right).

Here we only present the results for the scenario when both H and A contribute.

2HDM-I + VLLs:

We introduce the VLLs in the same way as in 2HDM-II + VLL model. We again take $Y_{\psi^l} = -1/2$ and choose the mass parameters of the VLLs such that the lighter mass eigenvalue of the charge -1 VLL is 375 GeV. In Fig. 7.2.9 we plot $\sigma(gg \rightarrow \phi \rightarrow \gamma\gamma)$ vs. y_1^l for various $\{\tan\beta, \kappa_{\Gamma}^2\}$ for $M_H = 735$, $M_A = 750$ GeV. We also show in Fig. 7.2.9, the unitarity constraint on y_1^l from the $\psi\psi \rightarrow \psi\psi$ process as a red vertical line. We see that in this case, $\sigma * BR_{\gamma\gamma} \gtrsim 10$ fb can be comfortably reached within the unitarity constraint, but for small κ_{Γ}^2 .

2HDM-I+VLL+VLQ:

We introduce the VLLs and the VLQs in the same way as in 2HDM+VLL+VLQ model. As before we take $Y_{\psi^l} = -1/2$ and choose the VLF mass parameters such that the lighter mass eigenvalue of the VLL is $M_{VL} = 375$ GeV. We first present our results for $M_{\zeta_2^q} = 1200$ GeV. In Fig. 7.2.10 we plot contours of $\sigma(gg \rightarrow \phi \rightarrow \gamma\gamma) = 1$ fb and the region $0.5 < \sigma(gg \rightarrow \phi \rightarrow$

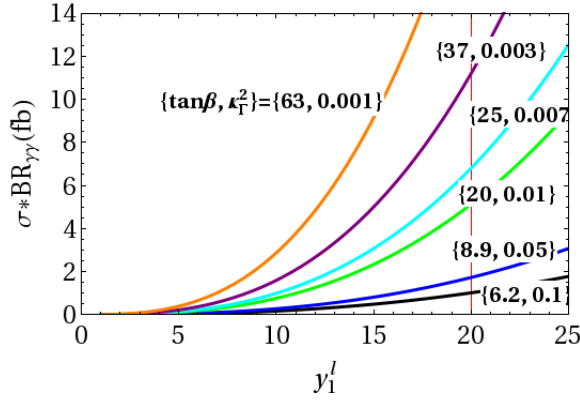


Figure 7.2.9: For 2HDM-I +VLL model,13 TeV LHC $\sigma(gg \rightarrow \phi \rightarrow \gamma\gamma)$ (in fb) with $M_{VL} = 375$ GeV. The unitarity constraint from $\psi\psi \rightarrow \psi\psi$ channel is shown by the red vertical line.

$\gamma\gamma) < 5$ for $M_{\zeta_2^q} = 1200$ GeV and $M_H = 735$, $M_A = 750$ GeV. The unitarity constraints on y_1^q, y_1^l from $\phi\phi \rightarrow \phi\phi$ and $\psi\psi \rightarrow \psi\psi$ channels are shown in solid red and dashed red respectively. In Fig. 7.2.11 we plot contours of $\sigma(gg \rightarrow \phi \rightarrow \gamma\gamma)$ in the $M_\phi - y^q$ plane obtained by saturating the unitarity bound $[y_{22}^q(N_c')^{1/4} + y_{22}^l] < 10$ and choosing $M_{VL} = M_\phi/2$, for $M_{\zeta_2^q} = 1200$ and 1500 GeV with $\tan\beta=25$.

7.2.2 Singlet scalar model

In this section we analyze a scenario where an SU(2) singlet CP-even scalar ϕ is coupled to a VLL ψ with hypercharge Y_ψ and VLQ U with hypercharge Y_U . We also introduce a coupling of the $\hat{\phi}$ with the SM-Higgs \hat{h} . We call this the $SVU\psi$ model. We consider the following Lagrangian:

$$\begin{aligned} \mathcal{L} \supset & -\frac{M_h^2}{2} H^\dagger H - \frac{M_\phi^2}{2} \Phi^2 - \frac{\kappa}{2} \Phi^2 H^\dagger H - \frac{\mu}{\sqrt{2}} \Phi H^\dagger H - M_\psi \bar{\psi}\psi \\ & - M_U \bar{U}U - \frac{y_\psi}{\sqrt{2}} \Phi \bar{\psi}\psi - \frac{y_U}{\sqrt{2}} \Phi \bar{U}U \end{aligned} \quad (7.2.3)$$

We assume that ϕ gets an expectation value $\langle \Phi \rangle = \xi$ and expand ϕ around ξ as $\Phi = \hat{\phi} + \xi$ and as usual H is expanded around its vacuum expectation value $v/\sqrt{2}$ as $H = (\hat{h} + v)/\sqrt{2}$ (in the unitary gauge). The $\kappa_{\phi hh}$ as defined in Eq. (7.1.1) becomes $\kappa_{\phi hh} = \sqrt{2}(\mu + \kappa\xi)/M_\phi$.

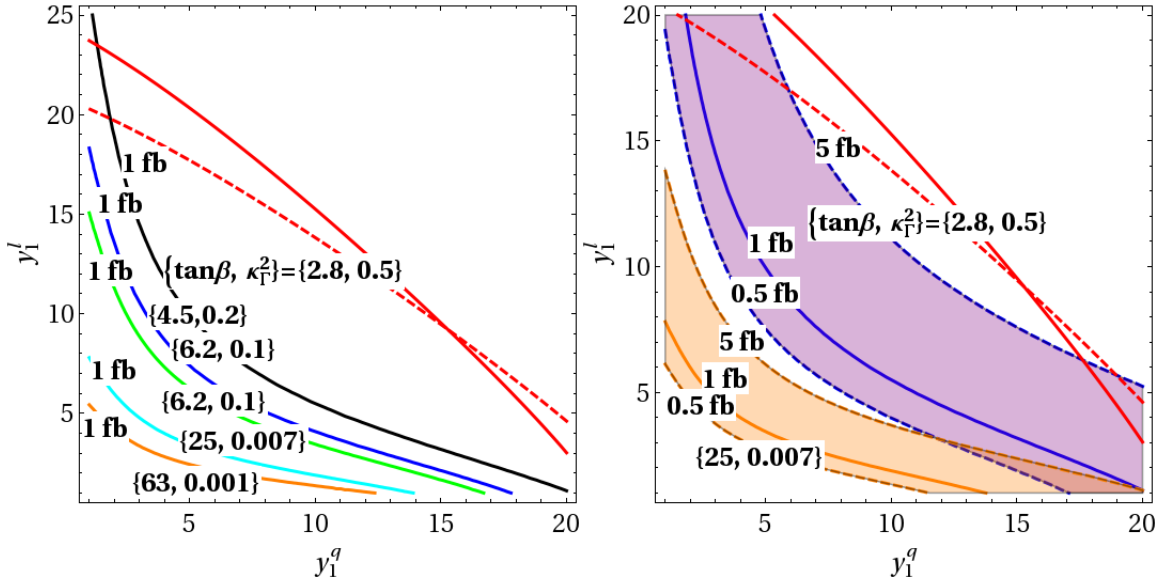


Figure 7.2.10: For 2HDM-I + VLL+VLQ model, contours of 13 TeV LHC $\sigma(gg \rightarrow \phi \rightarrow \gamma\gamma)$ (in fb) (left) and the regions $0.5 < \sigma(gg \rightarrow \phi \rightarrow \gamma\gamma) < 5$ fb (right), for various κ_F^2 shown, for $M_H = 735$, $M_A = 750$ GeV, $M_{\zeta_2^q} = 1200$ GeV and $M_{VL} = 375$ GeV.

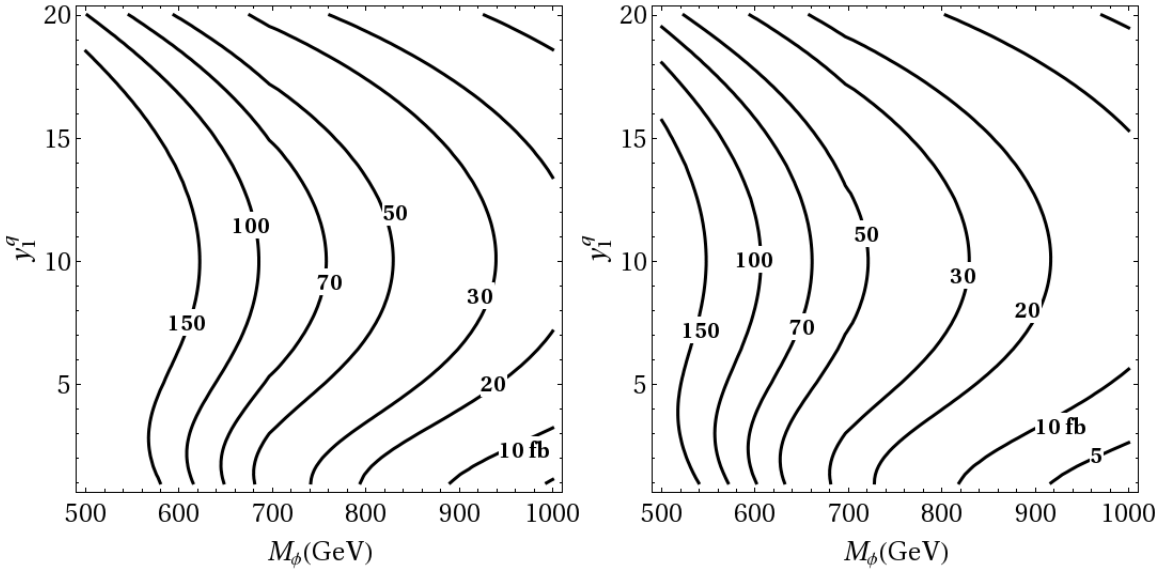


Figure 7.2.11: For 2HDM-I + VLL+VLQ model, contours of 13 TeV LHC $\sigma(gg \rightarrow \phi \rightarrow \gamma\gamma)$ (in fb) with y_1^l chosen to saturate the unitarity bound $[y_{22}^q(N_c')^{1/4} + y_{22}^l] < 10$ for $M_{VL} = M_\phi/2$, $\tan\beta = 25$, $M_{\zeta_2^q} = 1200$ (left) and 1500 GeV (right).

After EWSB $\hat{\phi}$ and \hat{h} mix, giving rise to two mass eigenstates ϕ and h which we define as

$$\begin{aligned}\phi &= \cos\theta_h \hat{\phi} + \sin\theta_h \hat{h} \\ h &= -\sin\theta_h \hat{\phi} + \cos\theta_h \hat{h}\end{aligned}\tag{7.2.4}$$

The lighter eigenstate h is identified as the SM Higgs boson. The mixing angle is given by

$$\tan 2\theta_h = \frac{\sqrt{2}\kappa_{\phi hh}}{(1 - M_h^2/M_\phi^2)} \frac{v}{M_\phi}.\tag{7.2.5}$$

In terms of the mass eigenstates the Lagrangian Eq. (7.2.3) can be written as

$$\mathcal{L} \supset -\frac{1}{4} \tan 2\theta_h (c_h^3 - 2c_h s_h^2) \frac{(M_\phi^2 - M_h^2)}{v} \phi h h.\tag{7.2.6}$$

In our numerical analysis we will take s_h as an input parameter. For a given model s_h can be related to the model parameters using Eq. (7.2.5).

If U and ψ can not decay to any SM particles it will be stable at cosmological scale. But, if $Y_U = 2/3$ than we can write down the mixed operator

$$\mathcal{L} \supset -\tilde{y}_U \bar{U} q_L^3 . H + h.c.,\tag{7.2.7}$$

where q_L^3 is the third generation SM quark doublet. In this case $U \rightarrow q^3 h$ decays are possible. We can take \tilde{y}_U to be small enough so that FCNCs are small but large enough so that U is not stable at the cosmological scale. If $Y_\psi = 0$ then we write down the mixed operator

$$\mathcal{L} \supset -\tilde{y}_\psi \bar{\psi} l_L^3 . H + h.c.,\tag{7.2.8}$$

where l_L^3 is third generation lepton. If $\tilde{y}_\psi = 0$ then \mathcal{L} has a Z_2 symmetry under which $\psi \rightarrow -\psi$ and all the SM particles are unchanged. In this case ψ cannot decay to any SM particles and can be a dark matter candidate. We will explore this scenario later in this thesis.

13 TeV LHC $\sigma(gg \rightarrow \phi \rightarrow \gamma\gamma)$

In this section we discuss the 13 TeV LHC $\sigma(gg \rightarrow \phi \rightarrow \gamma\gamma)$ in this model. The effective couplings $\kappa_{\phi gg}, \kappa_{\phi\gamma\gamma}$ in this model can be obtained from the general expressions given in Appendix A. As in the 2HDM we take $M_\phi = 750$ GeV as the benchmark point. In the ϕ width (Γ_ϕ) we include the partial widths $\Gamma(\phi \rightarrow \psi\psi, hh, tt, gg)$. The unitarity constraints on y_U, y_ψ from $UU \rightarrow UU$ and $\psi\psi \rightarrow \psi\psi$ processes obtained from the general expression given in Sec. 7.1.3 is given by

$$y_\psi + N_c^{1/4} y_U < 10. \quad (7.2.9)$$

We chose $M_\psi = 350$ GeV, $Y_\psi = 0$, $Y_U = 2/3$, $s_h = 0.01$ and plot in Fig. 7.2.12 the $\sigma(gg \rightarrow \phi \rightarrow \gamma\gamma)$ by scanning y_U, y_ψ in the range $0 < y_U < y_U^{max}, 0 < y_\psi < y_\psi^{max}$ subject to the unitarity constraint given by Eq. (7.2.9). The 8 TeV LHC hh channel as discussed in Sec. 7.1.2 constrains $\kappa_{\phi hh}$ or equivalently s_h to be very small. For example $s_h \lesssim 0.05$ for $y_U = 5$, $\kappa_\Gamma^2 = 0.1$. For $y_\psi \gtrsim 0.1$, the $BR(\phi \rightarrow \psi\psi)$ is dominant and y_ψ largely controls κ_Γ^2 . For $\kappa_\Gamma^2 = 3$, the $\sigma_\phi \times BR_{\gamma\gamma}$ can reach only 0.01 fb for $s_h = 0.01$ as seen in the left plot. For very small $y_\psi \lesssim 0.1$, the total width (i.e. κ_Γ^2) is small and dominated by $\phi \rightarrow gg$ decay through the top and U loops and the tree-level $\phi \rightarrow hh, tt$ decays. For $y_\psi \rightarrow 0$, $s_h \rightarrow 0$ both $\sigma * BR_{\gamma\gamma}$ and κ_Γ^2 comes from U loops and scales as y_U^4 and y_U^2 respectively; $\sigma * BR_{\gamma\gamma}$ increases with κ_Γ^2 in this region up to around $\kappa_\Gamma^2 \simeq 0.03$ as can be seen from Fig. 7.2.12. We can see that for $s_h = 0.01$ we can get $\sigma * BR_{\gamma\gamma} \simeq 10$ fb.

In Fig. 7.2.13 we show contours of $\sigma_\phi * BR_{\gamma\gamma}$ (in fb), and various κ_Γ^2 as colored regions, with the parameters not along the axes fixed at $s_h = 0.01$, $M_\psi = 350$ GeV, $M_U = 1000$ GeV, $y_\psi = 1$, $y_U = 5$. We also show in Fig. 7.2.13 the unitarity constraint on y_ψ (shown here by red line) for $y_U = 5$. For $y_U = 5$, $\sigma_\phi \simeq 1.5$ pb and the partial widths $\Gamma_{\{hh, tt, gg\}}$ for $s_h = 0.01$, $M_U = 1000$ GeV are 0.0065, 0.0031, 0.16 GeV respectively. For very small y_ψ or $M_\psi > M_\phi/2$, $\Gamma(\phi \rightarrow \psi\psi) \simeq 0$ and Γ_ϕ is dominated by $\Gamma_{\{hh, tt, gg\}}$; in this limit $BR_{\gamma\gamma} \simeq 3.3 * 10^{-3}$ and $\sigma * BR_{\gamma\gamma} \simeq 5$ fb for the set of parameters chosen with $s_h = 0.01$. If we decrease M_U , $\sigma * BR_{\gamma\gamma}$ can be even larger; for $M_U \simeq 650$ GeV, $M_\psi > M_\phi/2$, $\sigma * BR_{\gamma\gamma} \simeq 12$ fb can

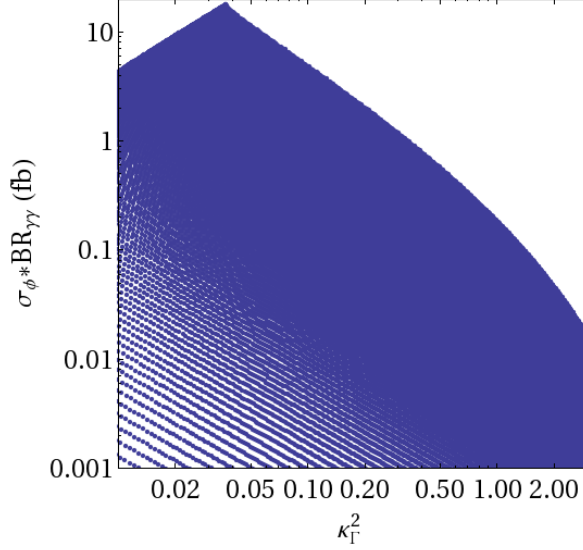


Figure 7.2.12: In the $SVU\psi$ model for $Y_\psi = 0$, $Y_U = 2/3$, the $\sigma_\phi * BR_{\gamma\gamma}$ (in fb) vs. κ_Γ^2 , for $M_\psi = 350$ GeV, $M_U = 1000$ GeV, $s_h = 0.01$ and y_U, y_ψ scanned over the range $0 < y_U < y_U^{max}$, $0 < y_\psi < y_\psi^{max}$ subject to the unitarity constraint.

be reached as can be seen from Fig. 7.2.13 although for a small $\kappa_\Gamma^2 \simeq 0.03$. For $M_\psi < M_\phi/2$ and y_ψ large, Γ_ϕ is large being dominated by $\phi \rightarrow \psi\psi$ decay resulting in very small $\sigma * BR_{\gamma\gamma}$. Thus, in the $SVU\psi$ model, it is not possible to generate both a large $\sigma_\phi \times BR_{\gamma\gamma}$ of a few fb and also a large $\kappa_\Gamma^2 \approx 3$. The reason is simply because a large Γ corresponding to $\kappa_\Gamma^2 \approx 3$ suppresses the $BR_{\gamma\gamma}$ to tiny values. In order to get an idea of how large $\sigma(gg \rightarrow \phi \rightarrow \gamma\gamma)$ can be within the unitarity constraint, in Fig. 7.2.14 we plot contours of $\sigma(gg \rightarrow \phi \rightarrow \gamma\gamma)$ in the $M_\phi - y_U$ plane with $M_\psi = M_\phi/2 - 25$ GeV, $s_h = 0$ and y_ψ chosen to saturate the unitarity constraint $y_U N_c^{1/4} + y_\psi < 10$ from the $\psi\psi \rightarrow \psi\psi$ channel.

We could take $Y_\psi = -1$, and since ψ is an SU(2) singlet, it has EM charge $Q_\psi = Y_\psi = -1$. For this case, to prevent a cosmologically stable charged relic, we additionally include a mixing term to a SM lepton that allows ψ to decay. Of course in this case ψ cannot be dark matter. One such example of a mixing term is to the SM SU(2) singlet τ_R , namely, $\mathcal{L} \supset -M'_{\psi\tau} \psi \tau^c + \text{h.c.}$, with $M'_{\psi\tau}$ taken small enough that leptonic FCNC constraints are not violated, but large enough that the ψ decay life-time due to $\psi \rightarrow h\tau$ decays is much smaller than cosmological time scales. Since ψ has EM charge, it will contribute to $\Gamma_{\gamma\gamma}$ also. In Fig. 7.2.15 we show for $Y_\psi = -1$, contours of $\sigma_\phi * BR_{\gamma\gamma}$ and regions of κ_Γ^2 for parameters

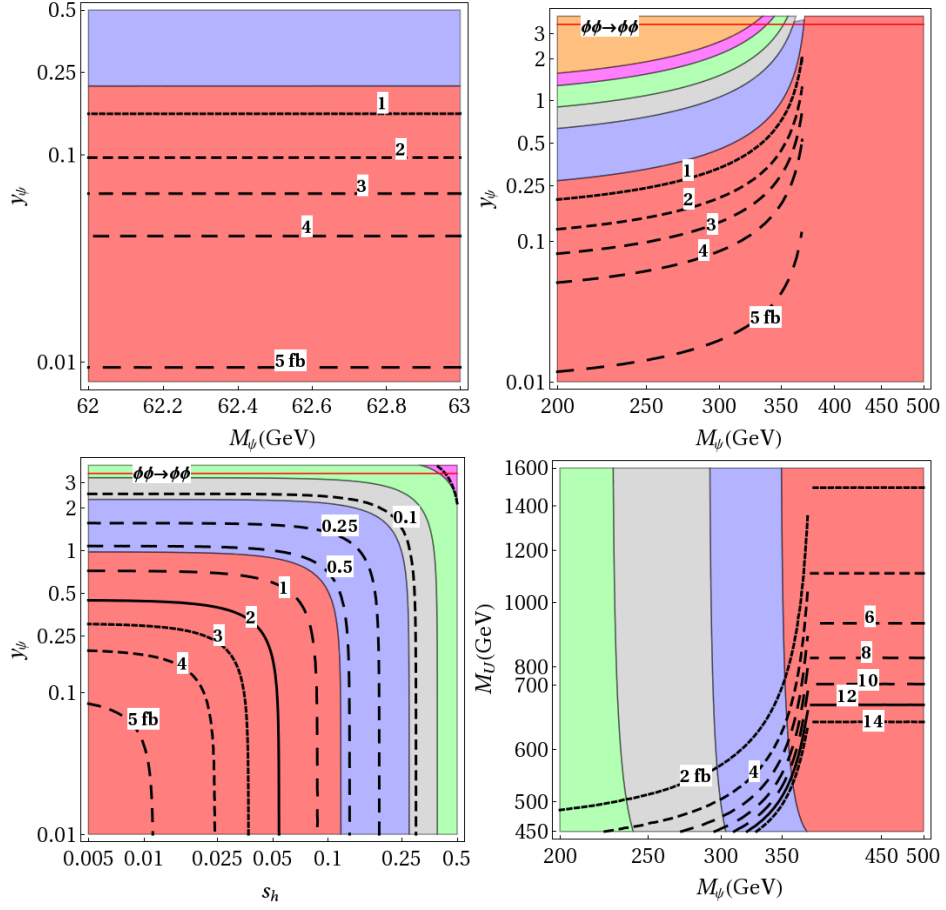


Figure 7.2.13: In the $SVU\psi$ model for $Y_\psi = 0$, $Y_U = 2/3$, the contours of $\sigma_\phi * BR_{\gamma\gamma}$ (in fb), and regions of $\kappa_T^2 < 0.1$ (red), $0.1 < \kappa_T^2 < 0.5$ (blue), $0.5 < \kappa_T^2 < 1$ (gray), $1 < \kappa_T^2 < 2$ (green), $2 < \kappa_T^2 < 3$ (pink), $\kappa_T^2 > 3$ (orange); parameters not along the axes are fixed at $s_h = 0.01$, $M_\psi = 350$ GeV, $M_U = 1000$ GeV, $y_\psi = 1$, $y_U = 5$. Unitarity constraint on y_ψ for $y_U = 5$ is shown by the red horizontal line. .

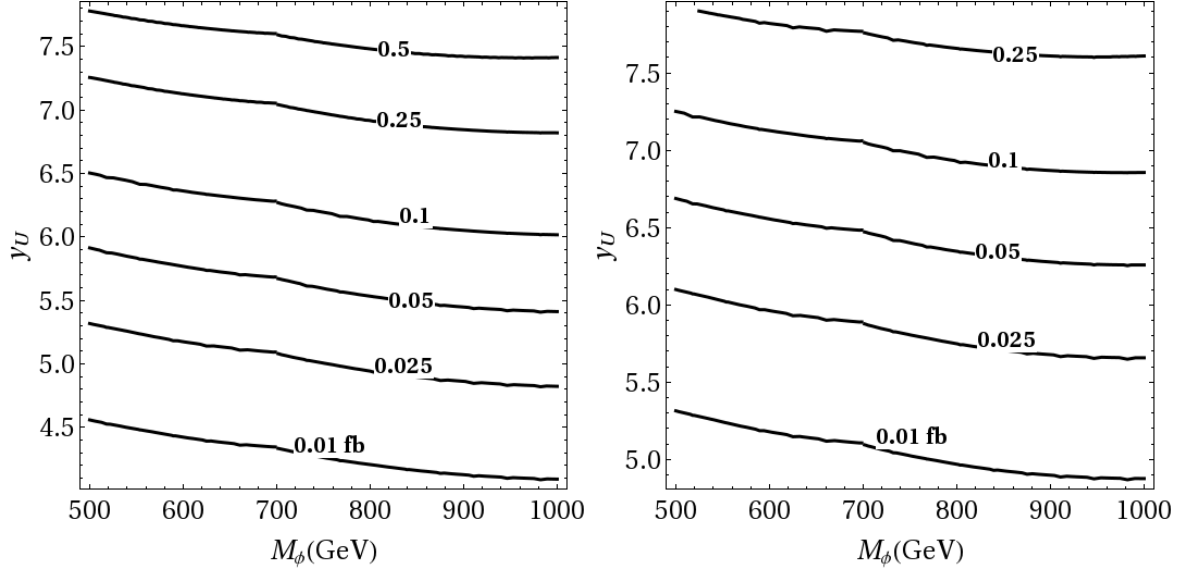


Figure 7.2.14: In $SVU\psi$ model, contours of $\sigma_\phi * BR_{\gamma\gamma}$ (in fb) for $M_U = 1200$ GeV (left) and 1500 GeV (right) with $M_\psi = M_\phi/2 - 25$ GeV, $s_h = 0$ and y_ψ chosen to saturate the unitarity constraint $y_U N_c^{1/4} + y_\psi < 10$.

not shown along the axes fixed at $y_\psi = 1$, $y_U = 5$, $s_h = 0$, $M_U = 1000$ GeV. We also show in Fig. 7.2.15 the unitarity constraint on y_ψ from $\phi\phi \rightarrow \phi\phi$ process for $y_U = 5$. In order to see how large the $\sigma(gg \rightarrow \phi \rightarrow \gamma\gamma)$ can be in this case, in Fig. 7.2.16 we plot contours of $\sigma(gg \rightarrow \phi \rightarrow \gamma\gamma)$ in the $M_\phi - y_U$ plane with $M_\psi = M_\phi/2$, $s_h = 0$ and y_ψ chosen to saturate the unitarity constraint $y_U N_c^{1/4} + y_\psi < 10$ from the $\psi\psi \rightarrow \psi\psi$ channel.

7.3 750 GeV diphoton excess

In this section we show the regions of parameter space that are consistent with the earlier 750 GeV excess. We start with a model independent analysis. In Fig. 7.3.1 we show the required values of $\kappa_{\phi gg}$ and $\kappa_{\phi\phi}$ which gives the required $\sigma(gg \rightarrow \phi \rightarrow \gamma\gamma)$ for various κ_Γ^2 . We next present the regions of parameter space which would have explained the diphoton excess in the 2HDM-II, X, I + VLF models and the $SVU\psi$ model.

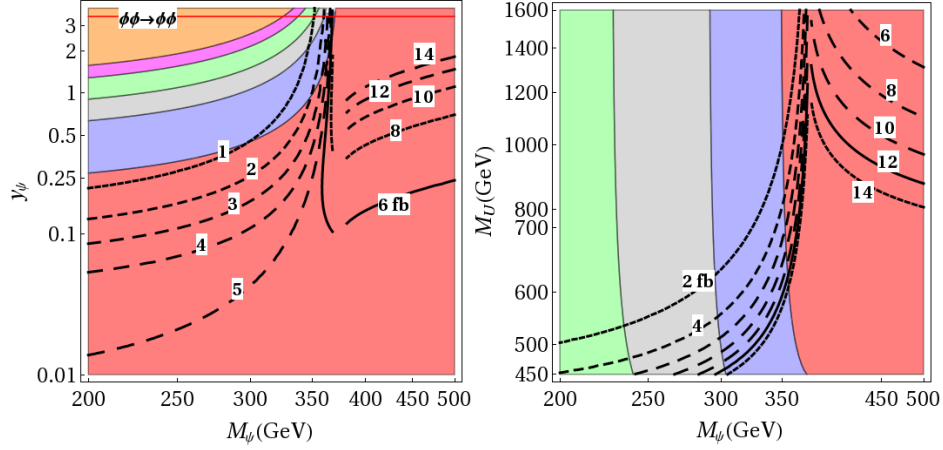


Figure 7.2.15: In the $SVU\psi$ model for $Y_\psi = -1$, $Y_U = 2/3$, $s_h = 0$, $y_U = 5$, contours of $\sigma * BR_{\gamma\gamma}$ (in fb), showing the regions $\kappa_\Gamma^2 < 0.1$ (red), $0.1 < \kappa_\Gamma^2 < 0.5$ (blue), $0.5 < \kappa_\Gamma^2 < 1$ (gray), $1 < \kappa_\Gamma^2 < 2$ (green), $2 < \kappa_\Gamma^2 < 3$ (pink), $\kappa_\Gamma^2 > 3$ (orange), with $M_U = 1000$ GeV (left), and $y_\psi = 1$ (right). Unitarity constraint on y_ψ from $\phi\phi \rightarrow \phi\phi$ for $y_U = 5$ is shown by the red horizontal line..

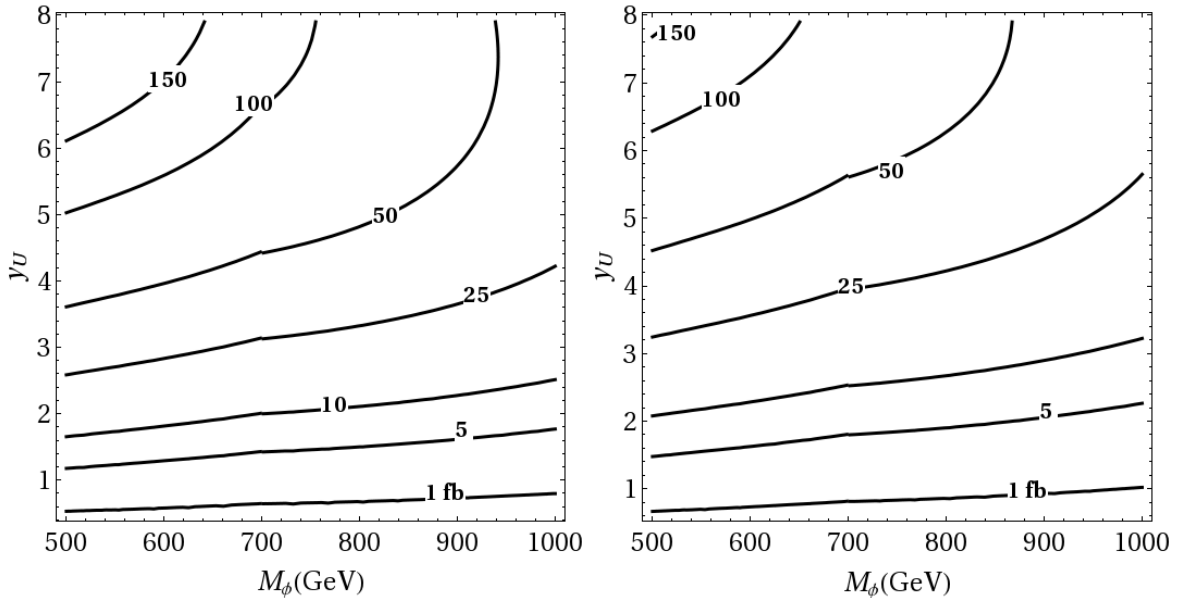


Figure 7.2.16: In $SVU\psi$ model, contours of $\sigma(gg \rightarrow \phi \rightarrow \gamma\gamma)$ (in fb) for $M_U = 1200$ GeV (left), 1500 GeV (right) with $M_\psi = M_\phi/2$ GeV, $s_h = 0$, $Y_\psi = -1$ and y_ψ chosen to saturate the unitarity constraint $y_U N_c^{1/4} + y_\psi < 10$.

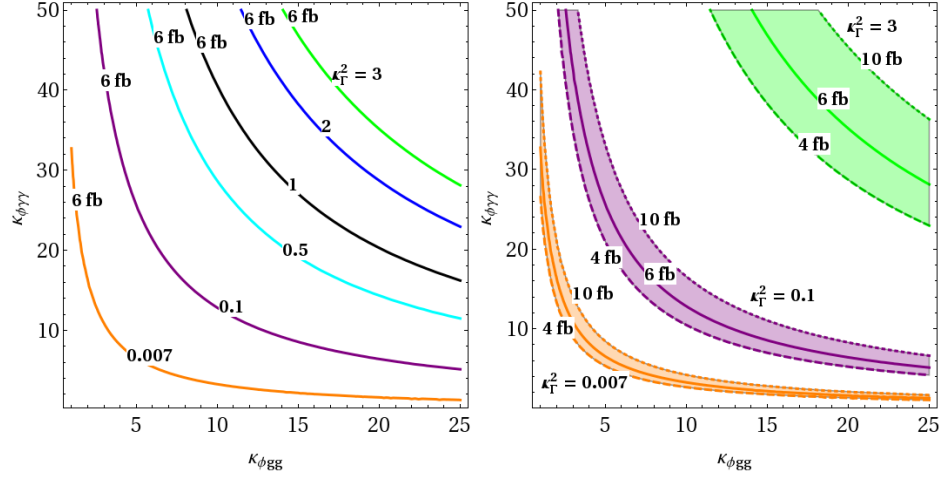


Figure 7.3.1: For $M_\phi = 750$ GeV, contours of 13 TeV LHC $\sigma(gg \rightarrow \phi \rightarrow \gamma\gamma)$ (in fb) (left) and the regions $4 < \sigma(gg \rightarrow \phi \rightarrow \gamma\gamma) < 10$ fb (right) for various κ_T^2 shown.

2HDM-II +VLL +VLQ model:

In the 2HDM-II+VLL+VLQ model we set $M_{\zeta_2^q} = 1000$ GeV and $M_{VL} = 375$ GeV. In Fig. 7.3.2 we plot contours of $\sigma(gg \rightarrow \phi \rightarrow \gamma\gamma) = 6$ fb with $M_H = 735$, $M_A = 750$ GeV for $M_{\zeta_2^q} = 1000$ GeV and show the regions that give the required cross section. Since both BR_{tt} and κ_T^2 are largely controlled by $\tan\beta$, a given κ_T^2 implies a certain BR_{tt} . In Fig. 7.3.2 we show by thick red dots the upper limit on y_1^q for a given κ_T^2 from the LHC $t\bar{t}$ search limits. For $\kappa_T^2 \gtrsim 0.5$ ($\tan\beta < 3$), $BR(\phi \rightarrow t\bar{t}) > 0.9$; therefore we get a nontrivial constraint on y_1^q in this region. For $\kappa_T^2 \simeq 0.24$ ($\tan\beta \simeq 5.7$), the $BR(\phi \rightarrow t\bar{t})$ is reduced to $\simeq 0.5$ and we do not get any constraint on y_1^q from the $\phi \rightarrow t\bar{t}$ results in the range we consider. We see that in this case it is possible to generate $\sigma * BR_{\gamma\gamma} = 6$ fb for $\kappa_T^2 \simeq 0.24$, without violating the unitarity constraint and the constraints from 8 TeV LHC $\phi \rightarrow t\bar{t}$ searches. For $\sigma * BR_{\gamma\gamma} = 6$ fb the maximum $\kappa_T^2 \simeq 0.5$. The reason for the larger cross section is the inclusion of A contribution; $\kappa_{AVV} \approx 2.5 * \kappa_{HVV}$ when $M_f \simeq M_\phi/2$ with M_f the mass of the fermion in the loop, and about $1.33 * \kappa_{HVV}$ for $M_\psi \gg M_\phi$.

2HDM-X+VLL+VLQ model:

We again choose $M_{\zeta_2^q} = 1000$ GeV and $M_{VL} = 375$ GeV and show the regions that are compatible with the excess. In Fig. 7.3.3 we show contours of $\sigma(gg \rightarrow \phi \rightarrow \gamma\gamma) = 6$ fb and

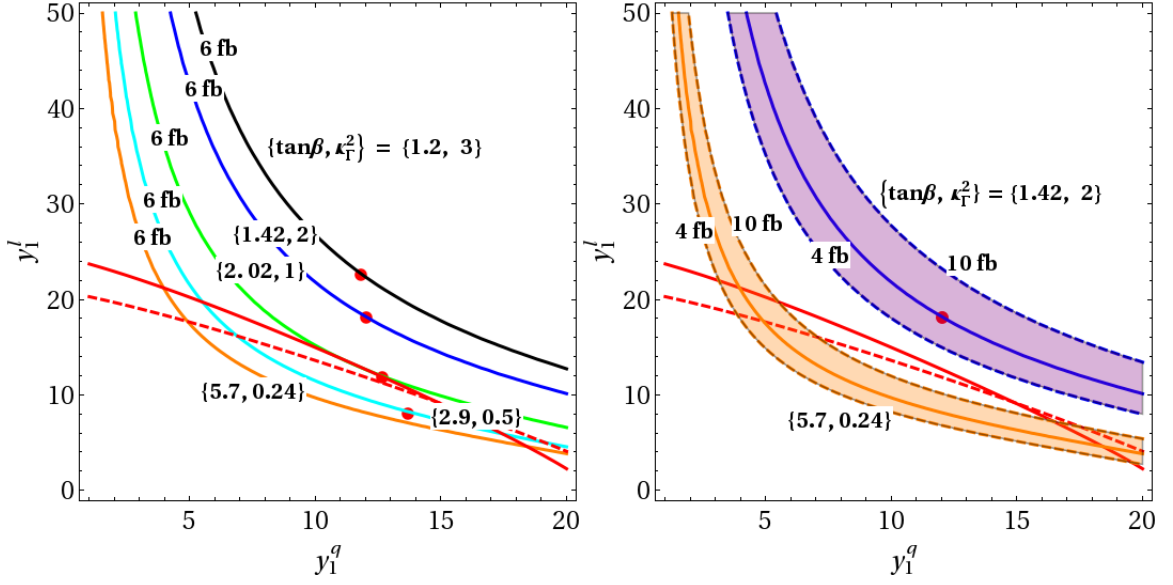


Figure 7.3.2: For 2HDM-II + VLL+VLQ model, contours of 13 TeV LHC $\sigma(gg \rightarrow \phi \rightarrow \gamma\gamma)$ (in fb) (left), $4 < \sigma(gg \rightarrow \phi \rightarrow \gamma\gamma) < 10$ fb (right) for various κ_T^2 shown, for $M_H = 735$, $M_A = 750$ $M_{\zeta_2^q} = 1000$ GeV and $M_{VL} = 375$ GeV. The region to the right of the red dots are excluded from 8 TeV LHC $\phi \rightarrow tt$ data. Unitarity constraints from $\phi\phi \rightarrow \phi\phi$ and $\psi\psi \rightarrow \psi\psi$ are shown in solid red and dashed red respectively.

the regions $4 < \sigma(gg \rightarrow \phi \rightarrow \gamma\gamma) < 10$ fb. Because of the enhanced $\sigma(gg \rightarrow \phi)$, the 8 TeV LHC $\phi \rightarrow tt$ results put constraints on y_1^q for $M_{\zeta_2^q} = 1000$ GeV. The upper bound on y_1^q is shown by the red dots. The upper bound y_1^q from the 8 TeV LHC $\phi \rightarrow \tau\tau$ result is shown by the gray dot. We see that in this case it is possible to generate $\sigma * BR_{\gamma\gamma} = 6$ fb for $\kappa_T^2 \simeq 0.1$. For $\sigma * BR_{\gamma} = 6$ fb a maximum of $\kappa_T^2 \simeq 0.5$ can be reached in this model as in the 2HDM-II.

2HDM-I +VLL model:

In Fig. 7.2.9 we have plotted the 13 TeV LHC $\sigma(gg \rightarrow \phi \rightarrow \gamma\gamma)$ with $M_{VL} = 375$ GeV for $M_H = 735$ and $M_A = 750$ GeV and also show the unitarity constraint from $\psi\psi \rightarrow \psi\psi$ channel by the red vertical line for 2HDM-I+VLL model. We see from Fig. 7.2.9 that within the unitarity bound $\sigma(gg \rightarrow \phi \rightarrow \gamma\gamma) \sim 6$ fb can be reached in this model for $\{\tan\beta, \kappa_T^2\} = \{25, 0.007\}$.

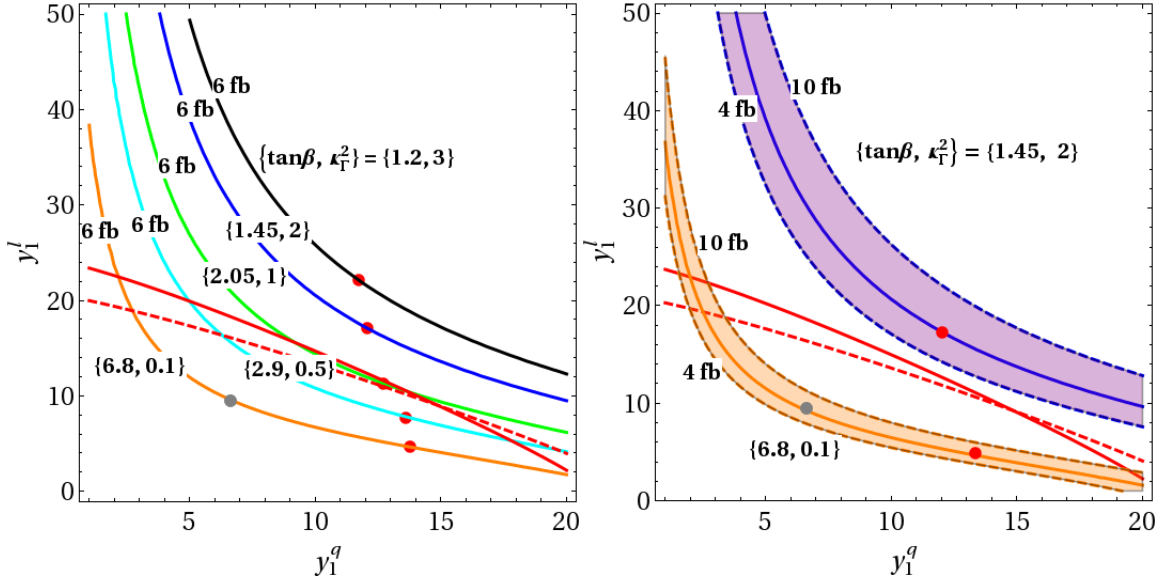


Figure 7.3.3: For 2HDM-X + VLL+VLQ model, contours of 13 TeV LHC $\sigma(gg \rightarrow \phi \rightarrow \gamma\gamma)$ (in fb) (left) and the region $4 < \sigma(gg \rightarrow \phi \rightarrow \gamma\gamma) < 10$ fb (right) for various κ_1^2 shown, for $M_H = 735$, $M_A = 750$ GeV, $M_{\zeta_2^q} = 1000$ GeV, $M_{VL} = 375$ GeV. To the right of the red dots and the gray dots are excluded from 8 TeV LHC $\phi \rightarrow tt$ data and the 8 TeV LHC $\phi \rightarrow \tau\tau$ data respectively.

2HDM-I+VLL+VLQ model:

In the 2HDM-I+VLL+VLQ we choose $M_{\zeta_2^q} = 1000$ GeV and $M_{VL} = 375$ GeV. In Fig. 7.3.4 we show contours of $\sigma(gg \rightarrow \phi \rightarrow \gamma\gamma) = 6$ fb and the region $4 < \sigma(gg \rightarrow \phi \rightarrow \gamma\gamma) < 10$ fb for various κ_1^2 with $M_{\zeta_2^q} = 1000$ GeV and $M_H = 735$, $M_A = 750$ GeV. Since $BR(\phi \rightarrow tt, \tau\tau)$ becomes small for large $\tan\beta$, there are no constraints on y_1^q from the 8 TeV LHC $\phi \rightarrow tt, \tau\tau$ results, for the range of parameters we have considered. We see that at $M_{\zeta_2^q} = 1000$ GeV, $\sigma * BR_{\gamma\gamma} \simeq 10$ fb can be reached within the unitarity constraint for $\kappa_1^2 \simeq 0.5$.

SVU ψ model:

In Figs. 7.2.13 and 7.2.15 we have plotted in the $M_\psi - y_\psi$ plane, the 13 TeV LHC $\sigma(\phi) \times BR(\gamma\gamma)$ for $s_h = 0.01, Y_\psi = 0$ and $s_h = 0, Y_\psi = -1$ respectively with $M_U = 1000$ GeV and $y_U = 5$, for SVU ψ model. For $Y_\psi = -1$, $\sigma(\phi) \times BR(\gamma\gamma) \sim 10$ fb can be reached for κ_1^2 as can be seen from Fig. 7.2.15. For $Y_\psi = 0$ the maximum cross section for $y_U = 5, M_U = 1000$ GeV is ~ 5 fb. However, for lower values of y_U , $\sigma(\phi) \times BR(\gamma\gamma) \sim 10$ fb can be reached for $y_\psi = 1, y_U = 5$ as we can see from Fig. 7.2.15 (bottom right plot).

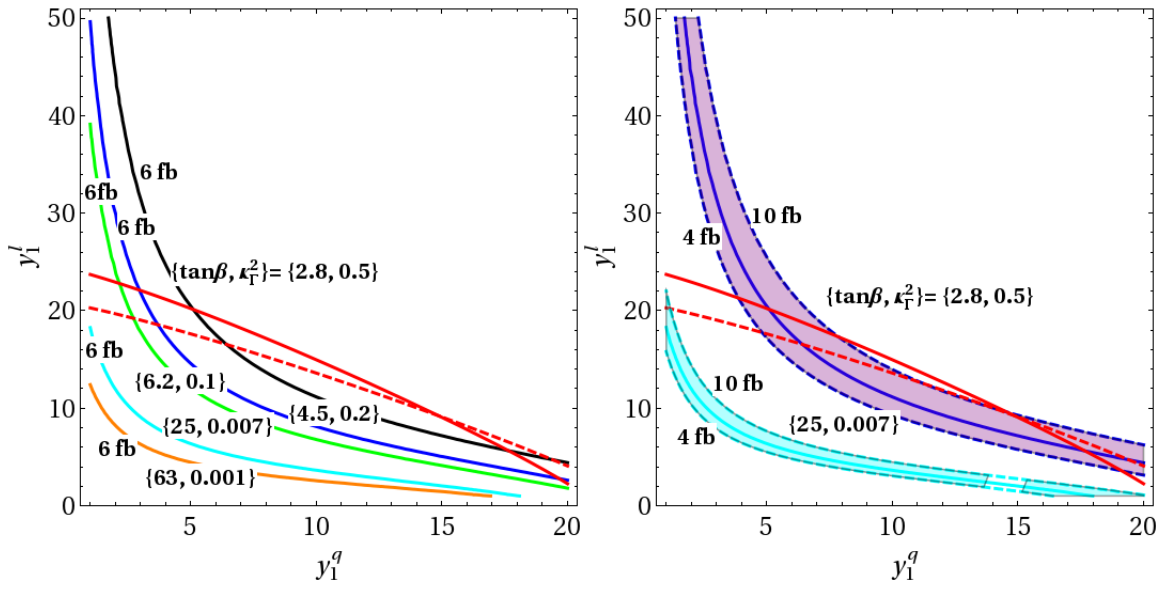


Figure 7.3.4: For 2HDM-I + VLL+VLQ model, contours of 13 TeV LHC $\sigma(gg \rightarrow \phi \rightarrow \gamma\gamma)$ (in fb) (left) and the region $4 < \sigma(gg \rightarrow \phi \rightarrow \gamma\gamma) < 10$ fb (right) for various κ_1^2 shown, for $M_H = 735$, $M_A = 750$ GeV, $M_{\zeta_2^q} = 1200$ GeV (top) and $M_{\zeta_2^q} = 1000$ GeV (bottom).

Chapter 8

WIMP dark Matter

Astrophysical and cosmological experiments in the last few decades have revealed a substantial abundance of dark matter. The most convincing evidence for the existence of dark matter comes from the study of the rotation curves of the galaxies and clusters of galaxies. The circular velocity v_r of any point located at a distance r from the center of a given galaxy is given by $v = \sqrt{GM(r)/r}$ where $M(r)$ is the total mass contained within the radius r . Study of the optical signals emitted from galaxies indicates that the visible matter is mostly concentrated near the center of the galaxy and therefore v_r should fall off as we move away from the center. However, the observed rotation curves reveal that v_r remains almost constant with r . This observation strongly suggests that there must be a halo of invisible matter surrounding every galaxy. Further evidence of the dark matter comes from the gravitational lensing studies of the bullet cluster. The most favoured candidate for dark matter are the so called “weakly interacting massive particles” (WIMP). As the name suggests the WIMPs have weak interactions with the SM particles and have masses in the 100 GeV to few TeV range.

8.1 Relic density

Here we consider a stable DM species in the thermal equilibrium in the early universe. The early universe was hot and dense and the dark matter particles (ψ) were in thermal equilib-

rium with the SM particles (X), since both the $\psi\psi \rightarrow XX$ and the reverse processes happened at the same rate. When the universe cooled down to a temperature (T) less than the dark matter mass (M_ψ), the $X_{SM}X_{SM} \rightarrow \psi\psi$ processes became energetically unfavorable and the equilibrium dark matter density was Boltzmann suppressed by $\sim e^{-M_\psi/T}$. However, since the universe is expanding and cooling, after a certain amount of time rate of the self annihilation processes $\psi\psi \rightarrow X_{SM}X_{SM}$ fell below the expansion rate and the dark matter particles “frozen out” when their density became almost constant. This process is governed by the Boltzmann equation

$$\frac{dn}{dt} = -3Hn - \langle\sigma_{XX}v_{rel}\rangle(n^2 - n_{eq}^2) \quad (8.1.1)$$

where n is the number density of the dark matter, n_{eq} is the equilibrium number density of the dark matter, H is the Hubble constant and $\langle\sigma_{XX}v_{rel}\rangle$ is the thermally averaged cross section for the process $\psi\psi \rightarrow XX$. In the radiation dominated era the Hubble’s constant is given by $H(T) = 1.66\sqrt{g_*}(T^2/M_{pl})$ where g_* is the effective degree of freedom at temperature T . The dark matter particles freezes out when the interaction rate becomes equal to the expansion rate of the universe

$$H(T_f) \sim n\langle\sigma_{XX}v_{rel}\rangle \quad (8.1.2)$$

$H(T_f) \sim n\langle\sigma_{XX}v_{rel}\rangle$. Introducing the variable $Y = n/s$, where s is the entropy density given by $s = 2\pi^2g_*T^3/45$, Eq. (8.1.1) can be written as

$$\frac{dY}{dt} = -\langle\sigma_{XX}v\rangle s(Y^2 - Y_{eq}^2) \quad (8.1.3)$$

where we have used the conservation of entropy per co moving volume a^3 (where a is the scale factor for the expansion of the universe)

$$\frac{d(sa^3)}{dt} = 0 \quad (8.1.4)$$

which implies $ds/dt + 3H = 0$. For $\langle\sigma_{XX}v\rangle$ small, Y is approximately conserved. After freeze out, the conserved value is given by $Y_f = n_f/s_f$. Using Eq. (8.1.2) we have

$$Y_f = \frac{3.78x_f}{\sqrt{g_{*f}}M_\psi M_{pl}\langle\sigma_{XX}v\rangle} \quad (8.1.5)$$

where $x_f = M_\psi/T_f$. The present entropy density is given by $s_0 = 2\pi^2g_{*0}T_0^3/45 = 22.1 \times 10^{-12} \text{ eV}^3$ where we have used present the temperature $T_0 = 2 \times 10^{-4} \text{ eV}$ and $g_{*0} = 6.3$ [143].

The present number density is then $n_o = s_0 Y_f$. The relic density of ψ is given by

$$\begin{aligned} \Omega_{dm} &= \frac{n_o M_\psi}{\rho_c} \\ &= \frac{10^{-10}x_f}{\sqrt{g_{*f}}M_{pl}\rho_c\langle\sigma_{XX}v_{rel}\rangle} \text{ eV}^3 \end{aligned} \quad (8.1.6)$$

where ρ_c is the critical density given by $\rho_c = (2.95 \times 10^{-3} \sqrt{h} \text{ eV})^4$ with $h = H/100 \text{ km s}^{-1} \text{ Mpc}^{-1}$. Using $g_{*f} \approx 100$ [143] we have

$$\Omega_{dm} = \frac{10^{-29}x_f}{\langle\sigma_{XX}v_{rel}\rangle} \text{ eV}^{-2}. \quad (8.1.7)$$

For $x_f \gg 1$, the dark matter particles are non relativistic and $\langle\sigma_{XX}v\rangle$ can be expanded as [144]

$$\begin{aligned} \langle\sigma_{XX}v_{rel}\rangle &= a + b\langle v^2\rangle + \mathcal{O}(v^4) \\ &= a + \frac{6b}{x_f} + \mathcal{O}(v^4) \end{aligned} \quad (8.1.8)$$

The second line in Eq. (8.1.8) follows from the fact that the dark matter particles obeys the Maxwell-Boltzmann velocity distribution and therefore $\langle v^2\rangle = 3g/x_f$ where $g = 2$ is the relativistic degree of freedom for Dirac fermions. The x_f can be determined iteratively from Eq. (8.1.2) as

$$x_f = \ln \frac{0.038gM_{pl}M_\psi\langle\sigma_{XX}v_{rel}\rangle}{\sqrt{x_f}\sqrt{g_{*f}}}. \quad (8.1.9)$$

The observed value of the relic density is given by $\Omega_{dm} \approx 0.26 \pm 0.015$ [145]. In order to obtain the correct relic density we need $\langle \sigma_{XX} v_{rel} \rangle \approx 2.3 \times 10^{-27} \text{ eV}^{-2}$ for $x_f \approx 25$. We will fix $x_f = 25$, since x_f depends only logarithmically on the parameters.

8.2 Dark matter direct detection

As we have discussed earlier, the WIMP dark matter must have interaction with the SM particles to get the correct relic density. This means that the WIMPs can be detected by earth based experiments as the WIMPs pass through the earth. The most promising method is direct detection in which one sets up a very sensitive detector on earth and measures the recoil energy of the detector nuclei as the WIMPs elastically scatters off them due to the $\psi X \rightarrow \psi X$ processes. In this work we are interested in the case when the interaction is mediated by a scalar in which case the scattering cross section is spin independent. For a WIMP (ψ) of mass M_ψ scattering off a target nucleon (N) of mass M_N , the spin independent cross section is given by [146]

$$\sigma_{DD}(\psi N \rightarrow \psi N) = \frac{M_\psi^2 M_N^2}{\pi(M_\psi + M_N)} |\mathcal{M}(\psi N \rightarrow \psi N)|^2. \quad (8.2.1)$$

For a nucleus with N neutrons and Z protons, this cross section has to be multiplied by a factor of $A^2 = (Z + N)^2$ to get the total direct detection cross section. Several experiments are now operating to detect the direct detection signals of dark matter. So far no signals have been observed which puts stringent limits on the WIMP direct detection cross sections. The most stringent limit comes from the LUX experiment, which sets a bound on the direct detection cross section of about $\sigma_{DD} \lesssim 10^{-45} \text{ cm}^2$ [147].

There are several BSM theories that have dark matter candidates. One very popular candidate is the neutralino in the R-parity symmetric supersymmetric theories. Some little-Higgs theories with T-parity also have scalar dark matter candidates. In Chapter 9, we will analyze a specific model namely the abelian hidden sector model with new vector-like fermions [59] that have a fermionic dark matter candidate.

Chapter 9

Singlet scalar model and dark matter

This chapter is based on the work done in Ref. [12]. In Sec. 7.2.2 of Chapter 7 we analyzed the $SVU\psi$ model defined by the Lagrangian in Eq. (7.2.3). This model has an SU(2) singlet neutral CP-even scalar ϕ , an SU(2) singlet vector-like quark U with hypercharge Y_U and an SU(2) singlet vector-like lepton ψ with hypercharge Y_ψ . When the mixing between the ψ and the SM fermions is zero then this model has a discrete Z_2 symmetry ($\psi \rightarrow -\psi$), as we have mentioned in Chapter 7. This Z_2 symmetry makes the ψ stable and therefore the ψ can be a good dark matter candidate. In this chapter we analyze the dark matter implications of this model. We obtain the allowed regions of the parameter space which gives the correct relic density while also satisfying the dark matter direct detection cross section.

9.1 Relic density

The relevant self annihilation channels are $\psi\psi \rightarrow ff, hh, ZZ, W^+W^-, gg$ through the ϕ and the h exchange. Here we present the cross sections for these processes. The Feynman diagrams contributing to these processes are shown in Fig. 9.1.1. The $\psi\psi \rightarrow hh$ process also has a t channel contribution which is not shown in Fig. 9.1.1. The t channel contribution is small because it involves the $h\psi\psi$ coupling which is suppressed by s_h . Therefore we do not include the t channel contribution to the $\psi\psi \rightarrow hh$ process.

In the CM frame, the 4-momenta of the initial ψ particles can be written as $p_1 = (E_\psi, 0, 0, p_\psi)$,

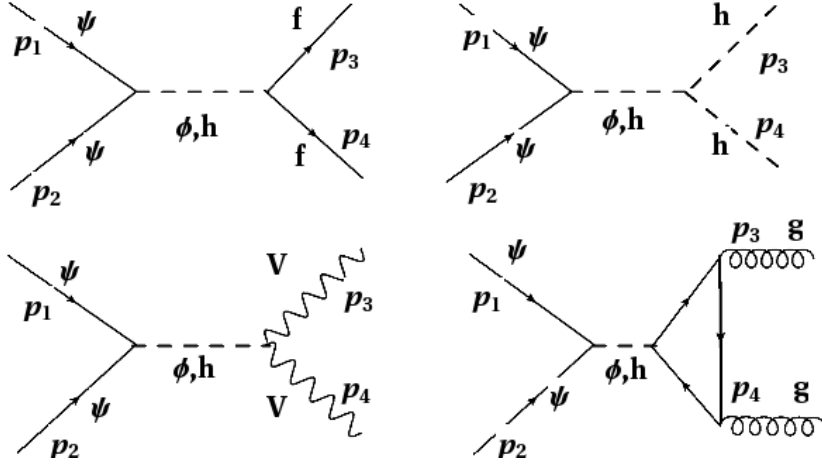


Figure 9.1.1: Feynman diagrams contributing to the $\psi\psi \rightarrow ff, hh, VV, gg$ processes.

$p_2 = (E_\psi, 0, 0, -p_\psi)$. In this frame the spin averaged cross sections for the process $\sigma(\psi\psi \rightarrow XX)$ can be written in terms of the amplitudes $\mathcal{M}(\psi\psi \rightarrow XX)$ (abbreviated as \mathcal{M}_{XX}) as

$$\sigma_{XX} = \frac{1}{8\pi s v_{rel}} \left(1 - \frac{4m_X^2}{s}\right)^{1/2} \left(\frac{1}{4} |\mathcal{M}_{XX}|^2\right) \quad (9.1.1)$$

where v_{rel} is the relative velocity of the ψ particles and s is the center of mass energy. Using Eq. (9.1.1) one can get the relic density Ω_{dm} from Eq. (8.1.7) in Chapter 8. The squared amplitude for the SM fermion final states are given by

$$\begin{aligned} \frac{1}{4} |\mathcal{M}_{ff}|^2 &= \frac{1}{4} \frac{y_f^2 y_\psi^2}{4} c_h^2 s_h^2 \text{Tr}(p_2 \cdot p_1 - m_\psi^2) \text{Tr}(p_3 \cdot p_4 - m_f^2) S_{BW} \\ &= \frac{1}{4} \frac{y_f^2 y_\psi^2}{4} c_h^2 s_h^2 \left[64 p_\psi^2 M_\psi^2 \left(1 - \frac{4m_f^2}{s}\right) \right] S_{BW} \end{aligned} \quad (9.1.2)$$

where

$$S_{BW} = \frac{(M_\phi^2 - M_h^2)^2}{[(s - M_\phi^2)^2 - M_\phi^2 \Gamma_\phi^2][(s - M_h^2)^2 - M_h^2 \Gamma_h^2]} \quad (9.1.3)$$

and we have used $p_3 \cdot p_4 = s/2 - m_f^2$. In the non-relativistic limit $s \approx 4M_\psi^2$ and $p_\psi \approx$

$M_\psi v_{rel}/2$, using which Eq. (9.1.2) can be written as

$$\sigma_{ff} = y_t^2 y_\psi^2 c_h^2 s_h^2 M_\psi^4 \left(1 - \frac{4m_f^2}{s}\right) v_{rel}^2 S_{BW}. \quad (9.1.4)$$

For the s channel $\psi\psi \rightarrow hh$ process, the squared amplitude is given by

$$\begin{aligned} \frac{1}{4} |\mathcal{M}_{hh}|^2 = \frac{y_\psi^2 M_\psi^2}{16} & \left[\frac{c_h^8 \kappa_{\phi hh}^2 M_\phi^2}{[(s - M_\phi^2)^2 - M_\phi^2 \Gamma_\phi^2]} + \frac{s_h^2 c_h^6 \kappa_{3h}^2 v^2}{[(s - M_h^2)^2 - M_h^2 \Gamma_h^2]} \right. \\ & \left. - \frac{2c_h^7 s_h \kappa_{\phi hh} \kappa_{3h} v M_\phi}{[(s - M_h^2)(s - M_\phi^2) - M_h M_\phi \Gamma_h \Gamma_\phi]} \right] v_{rel}^2 \end{aligned} \quad (9.1.5)$$

where κ_{3h} is the hhh coupling. The squared amplitude for the $\psi\psi \rightarrow W^+W^-$ channel is given by

$$\frac{1}{4} |\mathcal{M}_{WW}|^2 = \frac{1}{4} \frac{y_\psi^2}{2} s_h^2 c_h^2 \text{Tr}(p_2 \cdot p_1 - m_\psi^2) \frac{g^4 v^2}{4} g^{\mu\nu} g^{\rho\sigma} \sum_{\lambda_1 \lambda_2} \epsilon_{\lambda_1}^\mu(p_3) \epsilon_{\lambda_1}^{*\rho}(p_3) \epsilon_{\lambda_2}^\nu(p_4) \epsilon_{\lambda_2}^{*\sigma}(p_4) S_{BW}. \quad (9.1.6)$$

Summing over the polarizations and using $\sum \epsilon_{\lambda_1}^\mu(k) \epsilon_{\lambda_1}^{*\nu}(k) = (g^{\mu\nu} - k^\mu k^\nu / M_w^2)$ we get

$$\frac{1}{4} |\mathcal{M}_{WW}|^2 = \frac{1}{4} y_\psi^2 s_h^2 c_h^2 g^4 v^2 M_\psi^2 \left(\frac{1}{2} + \frac{(s/2 - M_W^2)}{4M_W^4} \right) v_{rel}^2 S_{BW}. \quad (9.1.7)$$

The $\psi\psi \rightarrow gg$ process proceeds via the ϕ and h exchange through the triangle loops as shown in Fig. 9.1.1. Both the SM fermions and the U contribute in the loop. In terms of the effective ϕgg coupling ($\kappa_{\phi gg}$) defined in Chapter 3, the $|\mathcal{M}_{gg}|^2$ is given by

$$\begin{aligned} \frac{1}{4} |\mathcal{M}_{gg}|^2 = \frac{1}{4} \frac{y_\psi^2}{2} & \text{Tr}(p_2 \cdot p_1 - m_\psi^2) (p_3^\beta p_4^\alpha - p_3 \cdot p_4 g^{\alpha\beta}) (p_3^\nu p_4^\mu - p_3 \cdot p_4 g^{\mu\nu}) \times 8 \times \\ & \left[\frac{c_h^2 \kappa_{\phi gg}^2}{[(s - M_\phi^2)^2 - M_\phi^2 \Gamma_\phi^2]} + \frac{s_h^2 \kappa_{hgg}^2}{[(s - M_h^2)^2 - M_h^2 \Gamma_h^2]} - \frac{2c_h s_h \kappa_{hgg} \kappa_{\phi gg}}{[(s - M_h^2)(s - M_\phi^2) - M_h M_\phi \Gamma_h \Gamma_\phi]} \right] \\ & \times \sum_{\lambda_1, \lambda_2} \epsilon_{\lambda_1}^{*\alpha} \epsilon_{\lambda_1}^{*\mu} \epsilon_{\lambda_2}^{*\beta} \epsilon_{\lambda_2}^{*\nu} \times v_{rel}^2 \end{aligned} \quad (9.1.8)$$

where $\epsilon_{\lambda_i}^\mu$ are the gluon polarization. The factor of 8 in Eq. (9.1.8) comes from the color

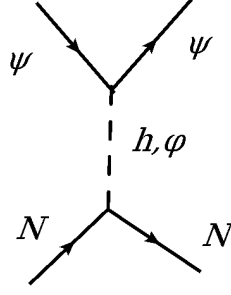


Figure 9.2.1: Feynman diagrams contributing to direct detection process $\psi N \rightarrow \psi N$.

sum. After summing over gluon polarizations we have

$$\frac{1}{4} |\mathcal{M}_{gg}|^2 = \frac{16y_\psi^2 M_\psi^6}{(16\pi^2 M)^2} \left[\frac{c_h^2 \kappa_{\phi gg}^2}{[(s - M_\phi^2)^2 - M_\phi^2 \Gamma_\phi^2]} + \frac{s_h^2 \kappa_{hgg}^2}{[(s - M_h^2)^2 - M_h^2 \Gamma_h^2]} - \frac{2c_h s_h \kappa_{hgg} \kappa_{\phi gg}}{[(s - M_h^2)(s - M_\phi^2) - M_h M_\phi \Gamma_h \Gamma_\phi]} \right] v_{rel}^2. \quad (9.1.9)$$

The $\kappa_{\phi gg}$ in this model can be obtained from the general expression given in Appendix A.

9.2 Dark matter direct detection cross section

The spins independent dark matter direct detection cross section (σ_{DD}) on the nucleon N is mediated by the h and ϕ exchange as shown in Fig. 9.2.1. The scalar coupling to the nucleon is generated through the quark content of the nucleon and also through the gluon content of the nucleon by the $\phi gg, hgg$ effective couplings. Since the h is lighter, the σ_{DD} is dominated by the h contribution for large s_h . But for small s_h ($\lesssim 0.05$) the $h\psi\psi$ coupling becomes small and the ϕ contribution becomes comparable to that of the h . We define an effective Lagrangian for the scalar nucleon coupling as

$$\begin{aligned} \mathcal{L} &= \lambda_{\phi NN} \hat{\phi} NN + \lambda_{\phi NN} \hat{h} NN \\ &= (c_h \lambda_{hNN} - s_h \lambda_{\phi NN}) h NN + (c_h \lambda_{\phi NN} + s_h \lambda_{hNN}) \phi NN. \end{aligned} \quad (9.2.1)$$

The σ_{DD} in the non-relativistic limit is given by

$$\begin{aligned}\sigma_{DD} &= \frac{y_\psi^2}{8\pi} \left(\frac{s_h(c_h\lambda_{hNN} - s_h\lambda_{\phi NN})}{M_h^2} - \frac{c_h(c_h\lambda_{\phi NN} + s_h\lambda_{hNN})}{M_\phi^2} \right) \\ &= \frac{y_\psi^2 c_h^2 s_h^2 \lambda_{hNN}^2 (|\mathbf{p}_\psi|^2 - m_N^2)}{8\pi M_h^4} \left[1 - \frac{\lambda_{\phi NN} c_h}{\lambda_{hNN} s_h} \frac{1 + \Delta_\phi M_h^2}{1 - \Delta_h M_\phi^2} \right]^2\end{aligned}\quad (9.2.2)$$

where $\Delta_h = (\lambda_{\phi NN}/\lambda_{hNN})(s_h/c_h)$ and $\Delta_\phi = (\lambda_{hNN}/\lambda_{\phi NN})(s_h/c_h)$, $p_\psi \approx M_\psi v_\psi$ with $v_\psi = 10^{-3}$ [148] and the nucleon mass $m_N = 1$ GeV. We take $\lambda_{hNN} = 2 \times 10^{-3}$ [148, 149].

The ϕNN coupling is generated by the effective ϕgg coupling induced by the U loop. Following Ref. [150] we obtain the ϕNN coupling as $\lambda_{\phi NN} = (2/27)f_{TG}^{(p,n)}(y_U m_N/M_U)$ where $f_{TG}^{(p,n)} = 1 - \sum_{q=u,d,s} f_{Tq}^{(p,n)}$ and the $f_{Tq}^{(p,n)}$ is defined by the relation $m_{p,n} f_{Tq}^{(p,n)} = \langle p, n | m_q \bar{q}q | p, n \rangle$.

The numerical values of $f_{Tq}^{(p,n)}$ are given in Ref. [150] using which we get $\lambda_{\phi NN} \approx 0.063 y_U m_N/M_U$.

In Fig. 9.2.2 we plot contours of $\Omega_{dm} = 0.1, 0.25, 0.3$ and for $\lambda_N = 2 \times 10^{-3}$, $m_N = 1$ GeV, show the regions with $\sigma_{DD} > 5 * 10^{-45} \text{cm}^2$, $10^{-45} \text{cm}^2 < \sigma_{DD} < 5 * 10^{-45} \text{cm}^2$, $10^{-46} \text{cm}^2 < \sigma_{DD} < 10^{-45} \text{cm}^2$, $10^{-47} \text{cm}^2 < \sigma_{DD} < 10^{-46} \text{cm}^2$, $10^{-48} \text{cm}^2 < \sigma_{DD} < 10^{-47} \text{cm}^2$, $10^{-49} \text{cm}^2 < \sigma_{DD} < 10^{-48} \text{cm}^2$, $\sigma_{DD} < 10^{-49} \text{cm}^2$ with parameters not varied along the axes fixed at $s_h = 0.01$, $M_\psi = 350$ GeV, $y_U = 5$ and $M_U = 1000$ GeV. We also show in Fig. 9.2.2 the unitarity constraint on y_ψ from $\phi\phi \rightarrow \phi\phi$ process for $y_U = 5$ and the constraint on s_h from the 8 TeV LHC $\phi \rightarrow hh$ results [11]. We see that for $s_h = 0.01$, $y_\psi \leq 3$ the direct detection cross section is close to or less than the current experimental limit $\sigma_{DD} \leq 10^{-45} \text{cm}^2$ [147]. We see that in order to get the correct relic density while also satisfying the dark matter direct detection cross section, we should be near the ϕ or the h pole $M_\psi = M_{\phi,h}/2$. We also see that in order to satisfy the 8 TeV LHC $\phi \rightarrow hh$ constraint, s_h has to be small ($\lesssim 0.05$). In Fig. 9.2.3 we plot contours of $\Omega_{dm} = 0.1, 0.25, 0.3$ and the regions $\sigma_{DD} < 10^{-48} \text{cm}^2$ (gray shaded), $10^{-48} < \sigma_{DD} < 10^{-47} \text{cm}^2$ (blue shaded), $10^{-47} < \sigma_{DD} < 10^{-46} \text{cm}^2$ (yellow shaded) and $\sigma_{DD} > 10^{-46} \text{cm}^2$ (orange shaded) in the $M_\phi - y_U$ plane with $M_\psi = M_\phi/2 - 25$ GeV, $s_h = 0$ and y_ψ chosen to saturate the unitarity constraint $y_U N_c^{1/4} + y_\psi < 10$ from the $\psi\psi \rightarrow \psi\psi$ channel. Since $s_h = 0$, the only relevant self annihilation channel is $\psi\psi \rightarrow gg$. For y_U large, y_ψ is small (because of saturating the unitarity constrain) and therefore the $\phi\psi\psi$ coupling and the

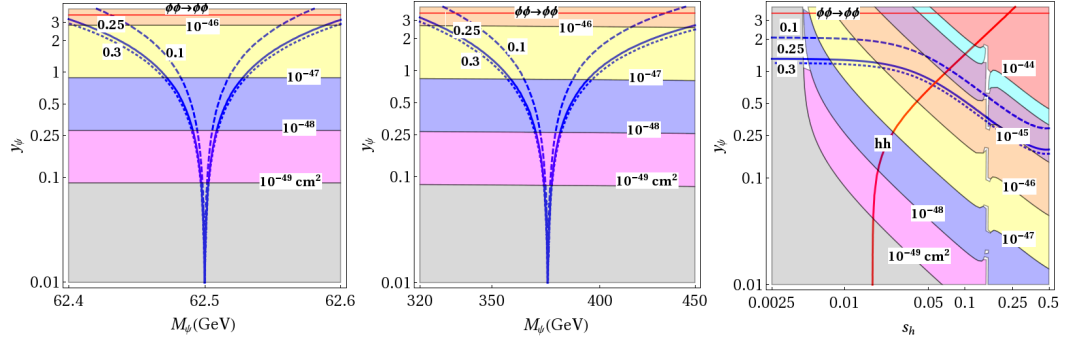


Figure 9.2.2: In the $SVU\psi$ model for $Y_\psi = 0$, $Y_U = 2/3$, contours of $\Omega_{dm} = 0.1$ (dashed blue), 0.25 (solid blue), 0.3 (dotted blue) with the colored bands showing σ_{DD} as marked, for $y_U = 5$, $M_U = 1000$ GeV, and with the parameters not varied along the axes fixed at $s_h = 0.01$ and $M_\psi = 350$ GeV. The red horizontal line shows the unitarity constraint for $y_U = 5$, and the thick red line shows the 8 TeV LHC hh channel constraint.

$\kappa_{\phi gg}$ is large. On the other hand for y_U small, y_ψ is large and therefore the $\phi\psi\psi$ coupling is large and $\kappa_{\phi gg}$ is small. As a result, for a given M_ϕ there are two values of y_U which gives the correct relic density. Similar result also hold for the σ_{DD} . In Chapter 7 we obtained the 13 TeV LHC $\sigma(\phi) \times BR(\phi \rightarrow \gamma\gamma)$ in the $M_\phi - y_U$ plane for the same choice of parameters. Using Fig. 9.2.3 and Fig. 7.2.14 one can obtain the 13 TeV LHC $\sigma(\phi) \times BR(\phi \rightarrow \gamma\gamma)$ for any M_ϕ, y_U which also gives the correct relic density and satisfies the experimental constraints on σ_{DD} . For example $M_\phi = 550$ GeV, $y_U \sim 7.5$ gives the correct relic density of 0.25 and $\sigma_{DD} < 10^{-46}$ cm². For the same value of M_ϕ and y_ψ , $\sigma(\phi) \times BR(\phi \rightarrow \gamma\gamma) \sim 0.25$ fb.

The direct-detection cross section bands we show in Fig. 9.2.2 is per nucleon, and without including a factor of $A = Z + N$ for coherent spin-independent scattering [146], where Z is the number of protons and N is the number of nucleons inside the nucleus. Thus our direct detection cross section is to be multiplied by a factor of A for the spin-independent case, before comparing with an experiment. For instance, for the LUX experiment [147] with a Xe target, our direct detection cross section numbers are to be multiplied by $A = 131$.

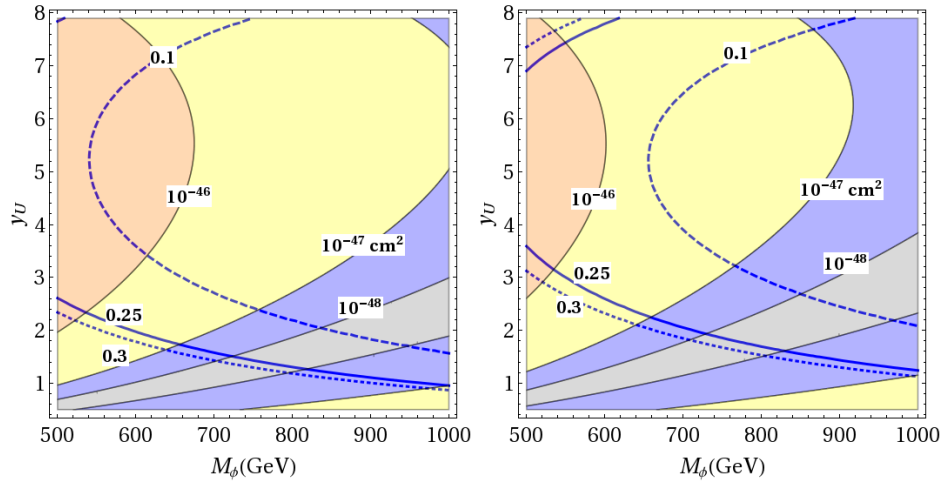


Figure 9.2.3: In the $SVU\psi$ model for $Y_\psi = 0$, $Y_U = 2/3$, $s_h = 0$, contours of $\Omega_{dm} = 0.1$ (dashed blue), 0.25 (solid blue) and 0.3 (dotted blue) with the colored bands showing σ_{DD} for $M_U = 1200$ GeV (left), 1500 GeV (right) with y_ψ chosen to saturate the unitarity bound $y_U N_c^{1/4} + y_\psi \leq 10$ and $M_\psi = M_\phi/2 - 25$ GeV.

Chapter 10

Summary and conclusions

Chapter 1 is an introductory chapter where we discuss some drawbacks of the SM on both theoretical and observational sides. Several BSM extensions have been proposed to overcome these issues. One important class of such theories are those, where the Higgs is realized as a pNGB of some spontaneously broken global symmetry. Examples of such theories are the little-Higgs models, technicolor models, composite Higgs models etc. In these theories, the Higgs is often accompanied by additional neutral scalars, either CP-odd or CP-even. Depending on the group structures and symmetry breaking patterns, these scalars can either be SU(2) singlets or can be embedded in an SU(2) doublet scalar. To complete the symmetry group representation these theories also contain new heavy VLFs. In this thesis we focus on the phenomenology of neutral BSM scalars with VLFs also present. In Chapter 1 we also briefly summarize some references that are relevant to our work. In Chapter 2 we briefly review some of the some of the BSM theories, namely theories with extended scalar sector, supersymmetric theories, extradimensional theories, little-Higgs theories and theories with strong dynamics. In Chapter 2 we also briefly discuss the phenomenology of vector-like fermions.

In Chapter 3 we perform a model independent analysis of BSM neutral scalars coupled to SM fermions and gauge bosons and also to new VLFs. We assume that these scalars are produced through the gluon fusion channel. We obtain the 8 TeV and 14 TeV LHC $\sigma(gg \rightarrow \phi)$ as a function of the effective ϕgg couplings ($\kappa_{\phi gg}$). We obtain the $\sigma(gg \rightarrow \phi)$ by relating

it to the corresponding cross section $\sigma(gg \rightarrow h_{SM})$ for the SM Higgs given in Ref. [32]. We obtain the constraints from the 8 TeV LHC $tt, \tau\tau, \gamma\gamma$ channel. We find that the most stringent constraint comes from the $\tau\tau$ channel. For $BR(\phi \rightarrow \tau\tau) \sim 1$, the upper limit on $\kappa_{\phi gg}$ is about ~ 3 . The $\phi \rightarrow tt$ channel results puts an upper limit $\kappa_{\phi gg} \lesssim 20$ for $BR(\phi \rightarrow tt) \sim 1$. In any given BSM model one can calculate the $\kappa_{\phi gg}$ and $BR(\phi \rightarrow tt, \tau\tau, \gamma\gamma)$ and use our results to obtain the LHC cross sections and the constraints on the parameter space of the model.

In Chapter 4 we present a simple model where a CP-odd SU(2) singlet scalar (A) is coupled to the VLFs, either SU(2) singlet or SU(2) doublet, and also to the SM Higgs. We obtain the effective A_{gg} couplings and $BR(A \rightarrow VV)$ for each of these models. For $m_A < m_h/2$, the h can decay to a pair of A thereby modifying the $h \rightarrow \gamma\gamma$ signal strength ($\mu_{\gamma\gamma}$) from its SM value. We also obtain the constraints on the parameter space from the 8 TeV LHC $\mu_{\gamma\gamma}$ results for $m_A < m_h/2$. There exists many BSM theories [122, 123, 124] with a similar structures to our effective model. For such models, one can use the results of this chapter to obtain the LHC cross sections and constraints on the parameter space.

In Chapter 5 we present a brief review of two-Higgs doublet models. We present the details of the mass spectrum of the physical scalars in the 2HDM and their couplings to the SM fermions in the 2HDM type-I, II and X. We discuss the so called 2HDM “alignment limit” and also the constraint on $\tan\beta$ from the perturbativity argument for the 2HDM with an exact Z_2 symmetry. In Chapter 6, we briefly discuss the phenomenology of the neutral scalars (collectively called ϕ) of 2HDM-II and X. We present the effective ϕ_{gg} couplings and the branching ratios of the ϕ to the SM fermions and gauge bosons. We also obtain the constraint on the parameter space of the 2HDM-II from the 8 TeV LHC $\phi \rightarrow \tau\tau$ results. We then add vector-like fermions to the 2HDM-II and X. We separately consider two cases, one in which the VLFs mix with the SM third generation fermions and one in which this mixing is shut off. We present the effective ϕ_{gg} couplings and the branching ratios of ϕ in each of these models. We find that the addition of vector-like fermions can significantly modify the $\kappa_{\phi gg}$ and $BR(\phi \rightarrow VV)$. The modification is even more prominent in the 2HDM-X. We also find that in one of these models, the constraint on the parameters space of the 2HDM-II is relaxed because of adding the VLFs. The results of this chapter can be used to obtain the

$\sigma(gg \rightarrow \phi)$ and BR_ϕ for realistic BSM theories which has the 2HDM structure with VLFs also present.

In Chapter 7, we specialize to the di-photon channel. We first perform a model independent analysis for a scalar coupled to the SM fermions and the new VLFs (ψ). We obtain the 13 TeV LHC $\sigma(gg \rightarrow \phi \rightarrow \gamma\gamma)$ as a function of the $\kappa_{\phi gg}$ for various ϕ widths. We discuss the constraints on the parameter space from the 8 TeV LHC $\phi \rightarrow tt, \tau\tau, hh$ results. We compute the constraints on the $\phi\psi\psi$ couplings from the perturbative unitarity of $\psi\psi \rightarrow \psi\psi$ and $\phi\phi \rightarrow \phi\phi$ processes. We obtain the 13 TeV LHC $\sigma(gg \rightarrow \phi \rightarrow \gamma\gamma)$ in few specific models, namely the 2HDM-I,II,X and a singlet scalar model with VLFs also added. Whenever relevant, we present the constraints on the parameter space of these models from the 8 TeV LHC $\phi \rightarrow tt, \tau\tau, hh$ channel results and the perturbative unitarity constraints. In the 2HDM we consider two scenarios, one in which only the H contributes to $\sigma(gg \rightarrow \phi \rightarrow \gamma\gamma)$ and one in which both the H and A contribute. In our analysis, we choose a benchmark point $M_\phi = 750$ GeV and obtain the 13 TeV LHC $\sigma(gg \rightarrow \phi \rightarrow \gamma\gamma)$ as a function of the VLF couplings for VLL and VLQ masses fixed. Subsequently, we obtain the 13 TeV LHC $\sigma(gg \rightarrow \phi \rightarrow \gamma\gamma)$ as a function of the VLQ coupling and M_ϕ with VLQ mass fixed, $M_{VL} \sim M_\phi/2$ and the VLL Yukawa couplings chosen to saturate the unitarity constraint. Such plots give an estimate of how large $\sigma(gg \rightarrow \phi \rightarrow \gamma\gamma)$ can be within the unitarity constraint. For example, in the 2HDM-II, $\sigma(gg \rightarrow \phi \rightarrow \gamma\gamma) \sim 70$ fb can be reached (see Fig. (7.2.5)) within the unitarity bound. Earlier both ATLAS and CMS had reported an excess in the di-photon channel at an invariant mass of 750 GeV [1, 2]. But recent results from ATLAS and CMS [141, 142] suggest that the observed signal was merely a statistical fluctuation. Here we also show the regions of parameter space compatible with the earlier excess.

In Chapter 8 we briefly review the WIMP dark matter, where we discuss the dark matter relic density and the direct detection cross section. In Chapter 9 we analyze the dark matter implications of the singlet scalar model ($SVU\psi$ model) presented in Chapter 7. The $SVU\psi$ model has a discrete Z_2 symmetry under which the ψ is odd, while the SM particles are even. Therefore the ψ cannot decay to any SM particle and can be a dark matter candidate. In Chapter 9 we find the regions of the parameter space which gives the correct relic den-

sity while also satisfying the constraints from the dark matter direct detection experiments. The relevant self annihilation channels are $\psi\psi \rightarrow tt, hh, WW, ZZ, gg$ through the ϕ and h exchange. The $\psi\psi \rightarrow tt, WW, ZZ$ channels are possible if the SM Higgs mix with ϕ . The $\psi\psi \rightarrow gg$ process can be nonzero even for $s_h = 0$ (where s_h is the mixing angle for the $h - \phi$ mixing) because the ϕ can couple to gg through the VLQ loops and can give the correct relic density as can be seen from Fig. 9.2.3. In general we find that in order to get the correct relic density while also satisfying the direct detection limits, the ψ mass (M_ψ) should be close to the ϕ pole ($M_\psi \sim M_\phi/2$).

Typically, BSM theories add a set of new heavy particles along with the SM particles. Therefore to test these theories we must study the phenomenology of these new particles in detail. We saw in Chapter 2 that there exist several BSM theories which have additional scalars and also new VLFs. In this thesis we study the phenomenology of the BSM neutral scalars (ϕ) in the presence of VLFs in a model independent way, without focusing on a specific model. To this end, we consider several effective models of BSM scalars with VLFs also present. We provide predictions for LHC cross sections, branching ratios and possible constraints on the parameter space for each of these models. Predictions of LHC cross sections and branching ratios are crucial for testing any BSM model. Using our results one can obtain the LHC cross sections and branching ratios of the BSM neutral scalars for a large class of models. One of the models namely the singlet scalar model also has a dark matter candidate in the form of a vector-like lepton (VLL). Here we highlight the role of the VLQ to the relic density and dark matter direct detection cross section. Both of these processes receive significant contributions from the ϕgg effective coupling induced via the VLQ. Interestingly, we find that even if the $\phi - h$ mixing is small, the VLQ contribution is sufficient to give the correct relic density while also satisfying the constraints from the dark matter direct detection cross section.

Here we discuss some of the possible directions that can be pursued in the future. We saw in Chapter 6 that in cases where VLQs mix with the SM third generation quarks (t, b), the decays $\phi \rightarrow t_2 t, b_2 b$ can be large for $M_\phi \gtrsim M_{t_2, b_2} + M_{t, b}$ as can be seen from Fig. 6.2.3. It will be interesting to study in detail, the $\phi \rightarrow t_2 t, b_2 b \rightarrow btW$ decay channels as signatures

of both ϕ and t_2, b_2 . Due to mixing with the SM quarks (SMQ), the VLQs will also make additional contributions to the flavor changing processes such as $B \rightarrow Kl^+l^-$, $B \rightarrow K^*l^+l^-$ decays and $B^0 - \bar{B}^0$, $K^0 - \bar{K}^0$, $D^0 - \bar{D}^0$ mixings. It will be worthwhile to find out the amount of allowed SMQ \leftrightarrow VLQ mixing consistent with the flavor observables in the context of the 2HDM. Studies of such flavor changing processes in certain vector-like extensions of the SM is done for example in Refs. [137, 151, 152, 153, 154, 155, 156, 157], to list a few. The other issue that should also be investigated is the stability of the electroweak vacuum. In general, fermions through their Yukawa couplings with the Higgs, contribute negatively to the beta function (β_λ) of the Higgs quartic coupling (λ). The VLFs therefore may drive λ negative, rendering the electroweak vacuum unstable at some finite energy scale (Λ). It will be important to find out the constraints on the VLF Yukawa couplings and masses requiring the vacuum to be stable up to a certain Λ .

Appendix A

The effective ϕgg and $\phi\gamma\gamma$ couplings

In this appendix we present the decay widths $\Gamma(\phi \rightarrow \gamma\gamma, gg)$ and the effective $\kappa_{\phi gg}, \kappa_{\phi\gamma\gamma}$ couplings for a general scalar ϕ coupled to a set of fermions f with charge Q_f . We define the Yukawa couplings from the Lagrangian

$$\mathcal{L} \supset -m_f \bar{f}f - y_{\phi ff} \phi \bar{f}f. \quad (\text{A.0.1})$$

The Feynman diagrams contributing to these processes are shown in Fig. A.0.1.

The amplitude for the $\phi \rightarrow \gamma\gamma$ process is given by

$$i\mathcal{M}(\phi \rightarrow \gamma\gamma) = \sum_f \frac{N_c^f}{8\pi^2} \left(\frac{y_{\phi ff}}{m_f} \right) (eQ_f)^2 D_{\mu\nu}^\phi \epsilon_1^\mu(p_1)^* \epsilon_2^\nu(p_2)^* F_{1/2}^\phi(r_f, m_f), \quad (\text{A.0.2})$$

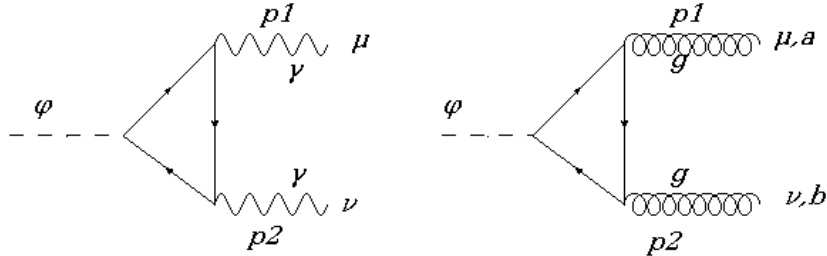


Figure A.0.1: Feynman diagrams contributing to $\phi \rightarrow \gamma\gamma$ (left) and $\phi \rightarrow gg$ (right).

where

$$\begin{aligned}
D_{\mu\nu}^A &= \epsilon_{\mu\nu\alpha\beta} p_1^\alpha p_2^\beta, \\
D_{\mu\nu}^H &= (p_{2\mu} p_{1\nu} - p_1 \cdot p_2 g_{\mu\nu}), \\
F^A(r_f, m_f) &= 4r_f \int_0^1 dx \int_0^1 dy \left(\frac{1}{r_f - xy} \right), \\
F^H(r_f, m_f) &= 4r_f \int_0^1 dx \int_0^1 dy \left(\frac{1 - 4xy}{r_f - xy} \right), \\
r_f &= \frac{m_f^2}{M_\phi^2}.
\end{aligned}$$

Squaring \mathcal{M} , summing over the photon polarizations and including the appropriate phase space factors, the decay width is given by

$$\Gamma(\phi \rightarrow \gamma\gamma) = \frac{1}{256\pi^3} \left[\sum_f \left(\frac{y_{\phi ff}}{m_f} \right) \left(\frac{e^2 Q_f^2}{4\pi} \right) (N_c F_{1/2}^\phi(r_f, m_f)) \right]^2. \quad (\text{A.0.3})$$

From the expression of $\Gamma(\phi \rightarrow \gamma\gamma)$ in Eq. (3.0.2) we infer

$$\kappa_{\phi\gamma\gamma} = 2e^2 \sum_f N_c^f Q_f^2 y_{\phi ff} \frac{M}{m_f} F_{1/2}^\phi(r_f). \quad (\text{A.0.4})$$

The amplitude for $\phi \rightarrow gg$ is given by,

$$i\mathcal{M}(\phi \rightarrow gg) = \frac{1}{8\pi^2} \sum_f \left(\frac{y}{m_f} \right) (g_s)^2 D_{\mu\nu}^\phi \epsilon_1^\mu(p_1)^* \epsilon_2^\nu(p_2)^* F_{1/2}^\phi(r_f, m_f) \left(\frac{1}{2} \delta_{ab} \right). \quad (\text{A.0.5})$$

Squaring \mathcal{M} , summing over the gluon polarizations and the color indices and including the appropriate phase space factors, the decay width $\Gamma(\phi \rightarrow gg)$ is given by

$$\Gamma(\phi \rightarrow gg) = \frac{1}{128\pi^3} \sum_f \left[\left(\frac{y_{\phi ff}}{m_f} \right) \left(\frac{g_s^2}{4\pi} \right) (N_c F_{1/2}^\phi(r_f, m_f)) \right]^2. \quad (\text{A.0.6})$$

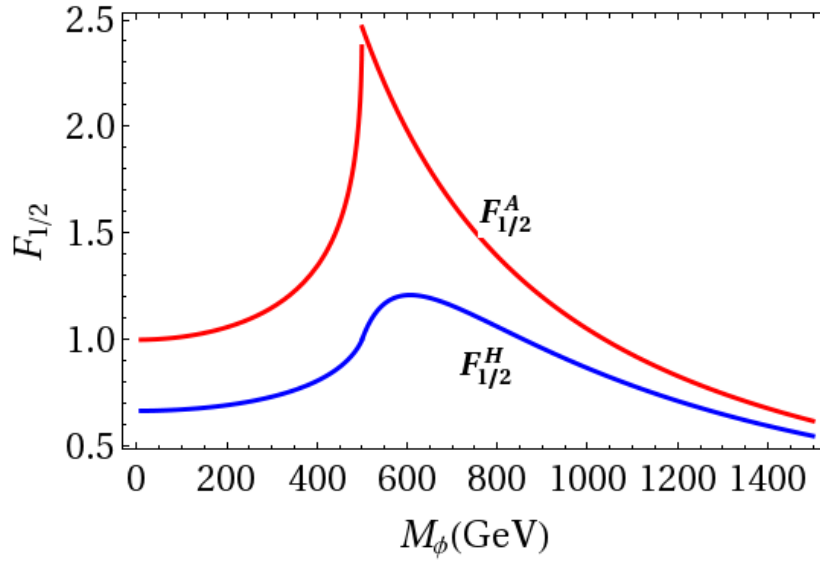


Figure A.0.2: $F_{1/2}^A$ and $F_{1/2}^H$ vs. M_ϕ for $m_f = 250$ GeV.

From the expression of $\Gamma(\phi \rightarrow gg)$ in Eq. (3.0.2) we again infer

$$\kappa_{\phi gg} = g_s^2 \sum_f y_{\phi ff} \frac{M}{m_f} F_{1/2}^{(1)}(r_f). \quad (\text{A.0.7})$$

To demonstrate the dependence of $\kappa_{\phi gg}$ on M_ϕ and m_f , we plot in Fig. A.0.2 the functions $F_{1/2}^A$ and $F_{1/2}^H$ as a function of M_ϕ for an example value of $m_f = 250$ GeV. We see that when $M_\phi \approx 2m_f$, the $F_{1/2}^A$ becomes very large because of f going onshell. We also see that at $M_\phi \approx 2m_f$, $F_{1/2}^A$ becomes $\approx 2.5F_{1/2}^H$.

Appendix B

Effective couplings in SVU and MVU models

Here we present the effective AVV couplings (κ_{AVV}) in the SVU and MVU models. The $\kappa_{\phi gg}$ and $\kappa_{\phi\gamma\gamma}$ in these models can be obtained from the general expressions given in App.

A. The $\kappa_{AZ\gamma}$ is given by

$$\kappa_{AZ\gamma} = 2e \frac{g}{c_W} \sum_i N_c^i Q_i (T_3^i - Q_i s_W^2) y_A \frac{M}{m_i} F_{1/2}^{(2)}(r_i, r_Z) \quad (\text{B.0.1})$$

with $r_Z = m_Z^2/m_A^2$ and

$$F_{1/2}^{(2)}(r_i, r_Z) = 4r_i \int_0^1 dy \int_0^{1-y} dx \frac{1}{r_i + (r_Z - 1)xy + r_Z(x^2 - x)}. \quad (\text{B.0.2})$$

The κ_{AZZ} for SVU and SVQ model is given by

$$\kappa_{AZZ} = 2 \left(\frac{g}{c_W} \right)^2 \sum_i N_c^i (T_3^i - Q_i s_W^2)^2 y_A \frac{M}{m_i} F_{1/2}^{(3)}(r_i, r_Z) \quad (\text{B.0.3})$$

with

$$F_{1/2}^{(3)}(r_i, r_Z) = 4 \int_0^1 dy \int_0^{1-y} dx \frac{r_i}{r_i - xy + r_Z[(x+y)^2 - (x+y)]}. \quad (\text{B.0.4})$$

The κ_{AWW} for SVQ model is given by

$$\kappa_{AWW} = 2 \left(\frac{g}{\sqrt{2}} \right)^2 \sum_i N_c^i y_A \frac{M}{m_i} F_{1/2}^{(3)}(r_i, r_W) \quad (\text{B.0.5})$$

with $r_W = m_W^2/m_A^2$.

References

- [1] The ATLAS collaboration. Search for resonances decaying to photon pairs in 3.2 fb^{-1} of pp collisions at $\sqrt{s} = 13 \text{ TeV}$ with the ATLAS detector. ATLAS-CONF-2015-081. 2015.
- [2] CMS Collaboration. Search for new physics in high mass diphoton events in proton-proton collisions at 13TeV . CMS-PAS-EXO-15-004. 2015.
- [3] Hsin-Chia Cheng and Ian Low. TeV symmetry and the little hierarchy problem. *JHEP*, 09:051, 2003.
- [4] Ian Low. T parity and the littlest Higgs. *JHEP*, 10:067, 2004.
- [5] Ian Low, Witold Skiba, and David Tucker-Smith. Little Higgses from an antisymmetric condensate. *Phys. Rev.*, D66:072001, 2002.
- [6] Georges Aad et al. A search for $t\bar{t}$ resonances using lepton-plus-jets events in proton-proton collisions at $\sqrt{s} = 8 \text{ TeV}$ with the ATLAS detector. *JHEP*, 08:148, 2015.
- [7] Georges Aad et al. Search for neutral Higgs bosons of the minimal supersymmetric standard model in pp collisions at $\sqrt{s} = 8 \text{ TeV}$ with the ATLAS detector. *JHEP*, 11:056, 2014.
- [8] CMS Collaboration. Search for an Higgs Like resonance in the diphoton mass spectra above 150 GeV with 8 TeV data. CMS-PAS-HIG-14-006. 2014.
- [9] Shrihari Gopalakrishna, Tuhin Subhra Mukherjee, and Soumya Sadhukhan. Extra neutral scalars with vectorlike fermions at the LHC. *Phys. Rev.*, D93(5):055004, 2016.

- [10] Shrihari Gopalakrishna, Tuhin Subhra Mukherjee, and Soumya Sadhukhan. Status and Prospects of the Two-Higgs-Doublet SU(6)/Sp(6) little-Higgs Model and the Alignment Limit. *Phys. Rev.*, D94(1):015034, 2016.
- [11] Georges Aad et al. Searches for Higgs boson pair production in the $hh \rightarrow bb\tau\tau, \gamma\gamma WW^*, \gamma\gamma bb, bbbb$ channels with the ATLAS detector. *Phys. Rev.*, D92:092004, 2015.
- [12] Shrihari Gopalakrishna and Tuhin Subhra Mukherjee. The 750 GeV diphoton excess in a two Higgs doublet model and a singlet scalar model, with vector-like fermions, unitarity constraints, and dark matter implications. arXiv:1604.05774. 2016.
- [13] Georges Aad et al. Observation of a new particle in the search for the Standard Model Higgs boson with the ATLAS detector at the LHC. *Phys. Lett.*, B716:1–29, 2012.
- [14] Serguei Chatrchyan et al. Observation of a new boson at a mass of 125 GeV with the CMS experiment at the LHC. *Phys. Lett.*, B716:30–61, 2012.
- [15] Murray Gell-Mann. A Schematic Model of Baryons and Mesons. *Phys. Lett.*, 8:214–215, 1964.
- [16] David J. Gross and Frank Wilczek. Ultraviolet Behavior of Nonabelian Gauge Theories. *Phys. Rev. Lett.*, 30:1343–1346, 1973.
- [17] H. David Politzer. Reliable Perturbative Results for Strong Interactions? *Phys. Rev. Lett.*, 30:1346–1349, 1973.
- [18] S. L. Glashow. Partial Symmetries of Weak Interactions. *Nucl. Phys.*, 22:579–588, 1961.
- [19] Steven Weinberg. A Model of Leptons. *Phys. Rev. Lett.*, 19:1264–1266, 1967.
- [20] Abdus Salam. Weak and Electromagnetic Interactions. *Conf. Proc.*, C680519:367–377, 1968.

- [21] J. S. Bell and R. Jackiw. A PCAC puzzle: $\pi^0 \rightarrow \gamma \gamma$ in the sigma model. *Nuovo Cim.*, A60:47–61, 1969.
- [22] Stephen L. Adler. Axial vector vertex in spinor electrodynamics. *Phys. Rev.*, 177:2426–2438, 1969.
- [23] Peter W. Higgs. Broken Symmetries and the Masses of Gauge Bosons. *Phys. Rev. Lett.*, 13:508–509, 1964.
- [24] C. Patrignani et al. Review of Particle Physics. *Chin. Phys.*, C40(10):100001, 2016.
- [25] P. Sikivie, Leonard Susskind, Mikhail B. Voloshin, and Valentin I. Zakharov. Isospin Breaking in Technicolor Models. *Nucl. Phys.*, B173:189–207, 1980.
- [26] Nicola Cabibbo. Unitary Symmetry and Leptonic Decays. *Phys. Rev. Lett.*, 10:531–533, 1963. [,648(1963)].
- [27] Makoto Kobayashi and Toshihide Maskawa. CP Violation in the Renormalizable Theory of Weak Interaction. *Prog. Theor. Phys.*, 49:652–657, 1973.
- [28] C. H. Llewellyn Smith. High-Energy Behavior and Gauge Symmetry. *Phys. Lett.*, B46:233–236, 1973.
- [29] John M. Cornwall, David N. Levin, and George Tiktopoulos. Derivation of Gauge Invariance from High-Energy Unitarity Bounds on the s Matrix. *Phys. Rev.*, D10:1145, 1974. [Erratum: *Phys. Rev.*D11,972(1975)].
- [30] Abdelhak Djouadi. The Anatomy of electro-weak symmetry breaking. I: The Higgs boson in the standard model. *Phys. Rept.*, 457:1–216, 2008.
- [31] H. M. Georgi, S. L. Glashow, M. E. Machacek, and Dimitri V. Nanopoulos. Higgs Bosons from Two Gluon Annihilation in Proton Proton Collisions. *Phys. Rev. Lett.*, 40:692, 1978.
- [32] Julien Baglio and Abdelhak Djouadi. Higgs production at the LHC. *JHEP*, 03:055, 2011.

- [33] S. L. Glashow, Dimitri V. Nanopoulos, and A. Yildiz. Associated Production of Higgs Bosons and Z Particles. *Phys. Rev.*, D18:1724–1727, 1978.
- [34] E. Eichten, I. Hinchliffe, Kenneth D. Lane, and C. Quigg. Super Collider Physics. *Rev. Mod. Phys.*, 56:579–707, 1984. [Addendum: *Rev. Mod. Phys.* 58,1065(1986)].
- [35] D. R. T. Jones and S. T. Petcov. Heavy Higgs Bosons at LEP. *Phys. Lett.*, 84B:440–444, 1979.
- [36] R. N. Cahn and Sally Dawson. Production of Very Massive Higgs Bosons. *Phys. Lett.*, B136:196, 1984. [Erratum: *Phys. Lett.* B138,464(1984)].
- [37] Duane A. Dicus and Scott S. D. Willenbrock. Higgs Bosons From Vector Boson Fusion in e^+e^- , ep and pp Collisions. *Phys. Rev.*, D32:1642, 1985.
- [38] Georges Aad et al. Measurements of the Total and Differential Higgs Boson Production Cross Sections Combining the $H \rightarrow \gamma\gamma$ and $H \rightarrow ZZ^* \rightarrow 4l$ Decay Channels at $\sqrt{s}=8$ TeV with the ATLAS Detector. *Phys. Rev. Lett.*, 115(9):091801, 2015.
- [39] Vardan Khachatryan et al. Observation of the diphoton decay of the Higgs boson and measurement of its properties. *Eur. Phys. J.*, C74(10):3076, 2014.
- [40] Georges Aad et al. Search for the Standard Model Higgs boson in the decay channel $H \rightarrow ZZ^* \rightarrow 4l$ with the ATLAS detector. *Phys. Lett.*, B705:435–451, 2011.
- [41] Serguei Chatrchyan et al. Search for the standard model Higgs boson in the decay channel H to ZZ to 4 leptons in pp collisions at $\sqrt{s} = 7$ TeV. *Phys. Rev. Lett.*, 108:111804, 2012.
- [42] Georges Aad et al. Observation and measurement of Higgs boson decays to WW^* with the ATLAS detector. *Phys. Rev.*, D92(1):012006, 2015.
- [43] Serguei Chatrchyan et al. Search for the standard model Higgs boson decaying to W^+W^- in the fully leptonic final state in pp collisions at $\sqrt{s} = 7$ TeV. *Phys. Lett.*, B710:91–113, 2012.

- [44] Georges Aad et al. Search for the Standard Model Higgs boson in the H to $\tau^+\tau^-$ decay mode in $\sqrt{s} = 7$ TeV pp collisions with ATLAS. *JHEP*, 09:070, 2012.
- [45] Serguei Chatrchyan et al. Evidence for the direct decay of the 125 GeV Higgs boson to fermions. *Nature Phys.*, 10:557–560, 2014.
- [46] Serguei Chatrchyan et al. Evidence for the 125 GeV Higgs boson decaying to a pair of τ leptons. *JHEP*, 05:104, 2014.
- [47] Serguei Chatrchyan et al. Search for Neutral MSSM Higgs Bosons Decaying to Tau Pairs in pp Collisions at $\sqrt{s} = 7$ TeV. *Phys. Rev. Lett.*, 106:231801, 2011.
- [48] Serguei Chatrchyan et al. Search for the standard model Higgs boson decaying to bottom quarks in pp collisions at $\sqrt{s} = 7$ TeV. *Phys. Lett.*, B710:284–306, 2012.
- [49] Georges Aad et al. Search for the $b\bar{b}$ decay of the Standard Model Higgs boson in associated $(W/Z)H$ production with the ATLAS detector. *JHEP*, 01:069, 2015.
- [50] Georges Aad et al. Measurements of the Higgs boson production and decay rates and constraints on its couplings from a combined ATLAS and CMS analysis of the LHC pp collision data at $\sqrt{s} = 7$ and 8 TeV. *JHEP*, 08:045, 2016.
- [51] Gerard 't Hooft. Naturalness, chiral symmetry, and spontaneous chiral symmetry breaking. *NATO Sci. Ser. B*, 59:135–157, 1980.
- [52] Michael E. Peskin and Daniel V. Schroeder. *An Introduction to quantum field theory*. 1995.
- [53] Romesh K. Kaul. Naturalness and Electro-weak Symmetry Breaking. arXiv:0803.0381. 2008.
- [54] Jorge de Blas, Mikael Chala, Manuel Perez-Victoria, and Jose Santiago. Observable Effects of General New Scalar Particles. *JHEP*, 04:078, 2015.
- [55] Stefano Profumo, Michael J. Ramsey-Musolf, and Gabe Shaughnessy. Singlet Higgs phenomenology and the electroweak phase transition. *JHEP*, 08:010, 2007.

- [56] Vernon Barger, Paul Langacker, Mathew McCaskey, Michael J. Ramsey-Musolf, and Gabe Shaughnessy. LHC Phenomenology of an Extended Standard Model with a Real Scalar Singlet. *Phys. Rev.*, D77:035005, 2008.
- [57] Robert Schabinger and James D. Wells. A Minimal spontaneously broken hidden sector and its impact on Higgs boson physics at the large hadron collider. *Phys. Rev.*, D72:093007, 2005.
- [58] Shrihari Gopalakrishna, Sunghoon Jung, and James D. Wells. Higgs boson decays to four fermions through an abelian hidden sector. *Phys. Rev.*, D78:055002, 2008.
- [59] Shrihari Gopalakrishna, Seung J. Lee, and James D. Wells. Dark matter and Higgs boson collider implications of fermions in an abelian-gauged hidden sector. *Phys. Lett.*, B680:88–93, 2009.
- [60] Baradhvaj Coleppa, Kunal Kumar, and Heather E. Logan. Can the 126 GeV boson be a pseudoscalar? *Phys. Rev.*, D86:075022, 2012.
- [61] Gustavo Burdman, Carlos E. F. Haluch, and Ricardo D. Matheus. Is the LHC Observing the Pseudo-scalar State of a Two-Higgs Doublet Model ? *Phys. Rev.*, D85:095016, 2012.
- [62] Beranger Dumont, John F. Gunion, Yun Jiang, and Sabine Kraml. Constraints on and future prospects for Two-Higgs-Doublet Models in light of the LHC Higgs signal. *Phys. Rev.*, D90:035021, 2014.
- [63] Beranger Dumont, John F. Gunion, Yun Jiang, and Sabine Kraml. Addendum to "Constraints on and future prospects for Two-Higgs-Doublet Models in light of the LHC Higgs signal. arXiv:1409.4088, 2014.
- [64] Kingman Cheung, Jae Sik Lee, and Po-Yan Tseng. Higgscision in the Two-Higgs Doublet Models. *JHEP*, 01:085, 2014.
- [65] Baradhvaj Coleppa, Felix Kling, and Shufang Su. Constraining Type II 2HDM in Light of LHC Higgs Searches. *JHEP*, 01:161, 2014.

- [66] Dipankar Das. New limits on $\tan \beta$ for 2HDMs with Z_2 symmetry. *Int. J. Mod. Phys.*, A30(26):1550158, 2015.
- [67] Gautam Bhattacharyya, Dipankar Das, Palash B. Pal, and M. N. Rebelo. Scalar sector properties of two-Higgs-doublet models with a global U(1) symmetry. *JHEP*, 10:081, 2013.
- [68] Kingman Cheung, Jae Sik Lee, Eibun Senaha, and Po-Yan Tseng. Confronting Higgsification with Electric Dipole Moments. *JHEP*, 06:149, 2014.
- [69] Alessandro Broggio, Eung Jin Chun, Massimo Passera, Ketan M. Patel, and Sudhir K. Vempati. Limiting two-Higgs-doublet models. *JHEP*, 11:058, 2014.
- [70] Chien-Yi Chen, S. Dawson, and Marc Sher. Heavy Higgs Searches and Constraints on Two Higgs Doublet Models. *Phys. Rev.*, D88:015018, 2013. [Erratum: *Phys. Rev.*D88,039901(2013)].
- [71] Aleksandra Drozd, Bohdan Grzadkowski, John F. Gunion, and Yun Jiang. Two-Higgs-Doublet Models and Enhanced Rates for a 125 GeV Higgs. *JHEP*, 05:072, 2013.
- [72] Benjamin Grinstein and Patipan Uttayarat. Carving Out Parameter Space in Type-II Two Higgs Doublets Model. *JHEP*, 06:094, 2013. [Erratum: *JHEP*09,110(2013)].
- [73] Alejandro Celis, Victor Ilisie, and Antonio Pich. LHC constraints on two-Higgs doublet models. *JHEP*, 07:053, 2013.
- [74] Sanghyeon Chang, Sin Kyu Kang, Jong-Phil Lee, Kang Young Lee, Seong Chan Park, and Jeonghyeon Song. Comprehensive study of two Higgs doublet model in light of the new boson with mass around 125 GeV. *JHEP*, 05:075, 2013.
- [75] Otto Eberhardt, Ulrich Nierste, and Martin Wiebusch. Status of the two-Higgs-doublet model of type II. *JHEP*, 07:118, 2013.
- [76] Baradhwaj Coleppa, Felix Kling, and Shufang Su. Exotic Decays Of A Heavy Neutral Higgs Through HZ/AZ Channel. *JHEP*, 09:161, 2014.

- [77] P. S. Bhupal Dev and Apostolos Pilaftsis. Maximally Symmetric Two Higgs Doublet Model with Natural Standard Model Alignment. *JHEP*, 12:024, 2014. [Erratum: *JHEP*11,147(2015)].
- [78] Julien Baglio, Otto Eberhardt, Ulrich Nierste, and Martin Wiebusch. Benchmarks for Higgs Pair Production and Heavy Higgs boson Searches in the Two-Higgs-Doublet Model of Type II. *Phys. Rev.*, D90(1):015008, 2014.
- [79] Werner Bernreuther, Patrick Gonzalez, and Martin Wiebusch. Pseudoscalar Higgs Bosons at the LHC: Production and Decays into Electroweak Gauge Bosons Revisited. *Eur. Phys. J.*, C69:31–43, 2010.
- [80] Werner Bernreuther, Patrick Gonzalez, and Martin Wiebusch. Pseudoscalar Higgs Boson Decays into W and Z Bosons Revisited. *arXiv:0909.3772*. 2009.
- [81] Georges Aad et al. Measurements of Higgs boson production and couplings in diboson final states with the ATLAS detector at the LHC. *Phys. Lett.*, B726:88–119, 2013. [Erratum: *Phys. Lett.*B734,406(2014)].
- [82] Combination of standard model Higgs boson searches and measurements of the properties of the new boson with a mass near 125 GeV. (CMS-PAS-HIG-13-005), 2013.
- [83] Pierre Ramond. Dual Theory for Free Fermions. *Phys. Rev.*, D3:2415–2418, 1971.
- [84] A. Neveu and J. H. Schwarz. Factorizable dual model of pions. *Nucl. Phys.*, B31:86–112, 1971.
- [85] Jean-Loup Gervais and B. Sakita. Field Theory Interpretation of Supergauges in Dual Models. *Nucl. Phys.*, B34:632–639, 1971.
- [86] Yu. A. Gol’fand and E. P. Likhtman. Extension of the Algebra of Poincare Group Generators and Violation of p Invariance. *JETP Lett.*, 13:323–326, 1971. [*Pisma Zh. Eksp. Teor. Fiz.*13,452(1971)].

- [87] D. V. Volkov and V. P. Akulov. Is the Neutrino a Goldstone Particle? *Phys. Lett.*, 46B:109–110, 1973.
- [88] Rudolf Haag, Jan T. Lopuszanski, and Martin Sohnius. All Possible Generators of Supersymmetries of the s Matrix. *Nucl. Phys.*, B88:257, 1975.
- [89] J. Wess and B. Zumino. Supergauge Transformations in Four-Dimensions. *Nucl. Phys.*, B70:39–50, 1974.
- [90] Romesh K. Kaul and Parthasarathi Majumdar. Cancellation of Quadratically Divergent Mass Corrections in Globally Supersymmetric Spontaneously Broken Gauge Theories. *Nucl. Phys.*, B199:36, 1982.
- [91] Edward Witten. Mass Hierarchies in Supersymmetric Theories. *Phys. Lett.*, B105:267, 1981.
- [92] S. Dimopoulos, S. Raby, and Frank Wilczek. Supersymmetry and the Scale of Unification. *Phys. Rev.*, D24:1681–1683, 1981.
- [93] Luis E. Ibanez and Graham G. Ross. SU(2)-L x U(1) Symmetry Breaking as a Radiative Effect of Supersymmetry Breaking in Guts. *Phys. Lett.*, B110:215–220, 1982.
- [94] William J. Marciano and Goran Senjanovic. Predictions of Supersymmetric Grand Unified Theories. *Phys. Rev.*, D25:3092, 1982.
- [95] Nima Arkani-Hamed, Savas Dimopoulos, and G. R. Dvali. The Hierarchy problem and new dimensions at a millimeter. *Phys. Lett.*, B429:263–272, 1998.
- [96] Lisa Randall and Raman Sundrum. A Large mass hierarchy from a small extra dimension. *Phys. Rev. Lett.*, 83:3370–3373, 1999.
- [97] Sanghyeon Chang, Junji Hisano, Hiroaki Nakano, Nobuchika Okada, and Masahiro Yamaguchi. Bulk standard model in the Randall-Sundrum background. *Phys. Rev.*, D62:084025, 2000.

- [98] Tony Gherghetta and Alex Pomarol. Bulk fields and supersymmetry in a slice of AdS. *Nucl. Phys.*, B586:141–162, 2000.
- [99] Kaustubh Agashe, Antonio Delgado, Michael J. May, and Raman Sundrum. RS1, custodial isospin and precision tests. *JHEP*, 08:050, 2003.
- [100] David E. Kaplan and Martin Schmaltz. The Little Higgs from a simple group. *JHEP*, 10:039, 2003.
- [101] Martin Schmaltz. The Simplest little Higgs. *JHEP*, 08:056, 2004.
- [102] N. Arkani-Hamed, A. G. Cohen, E. Katz, A. E. Nelson, T. Gregoire, and Jay G. Wacker. The Minimal moose for a little Higgs. *JHEP*, 08:021, 2002.
- [103] Spencer Chang. A 'Littlest Higgs' model with custodial SU(2) symmetry. *JHEP*, 12:057, 2003.
- [104] Spencer Chang and Jay G. Wacker. Little Higgs and custodial SU(2). *Phys. Rev.*, D69:035002, 2004.
- [105] Hsin-Chia Cheng and Ian Low. Little hierarchy, little Higgses, and a little symmetry. *JHEP*, 08:061, 2004.
- [106] David B. Kaplan, Howard Georgi, and Savas Dimopoulos. Composite Higgs Scalars. *Phys. Lett.*, B136:187–190, 1984.
- [107] Michael J. Dugan, Howard Georgi, and David B. Kaplan. Anatomy of a Composite Higgs Model. *Nucl. Phys.*, B254:299–326, 1985.
- [108] Ben Gripaios, Alex Pomarol, Francesco Riva, and Javi Serra. Beyond the Minimal Composite Higgs Model. *JHEP*, 04:070, 2009.
- [109] David Marzocca, Marco Serone, and Jing Shu. General Composite Higgs Models. *JHEP*, 08:013, 2012.

- [110] Kaustubh Agashe, Roberto Contino, and Alex Pomarol. The Minimal composite Higgs model. *Nucl. Phys.*, B719:165–187, 2005.
- [111] Vardan Khachatryan et al. Search for vector-like charge $2/3$ T quarks in proton-proton collisions at $\sqrt{s} = 8$ TeV. *Phys. Rev.*, D93(1):012003, 2016.
- [112] Sebastian A. R. Ellis, Rohini M. Godbole, Shrihari Gopalakrishna, and James D. Wells. Survey of vector-like fermion extensions of the Standard Model and their phenomenological implications. *JHEP*, 09:130, 2014.
- [113] J. A. Aguilar-Saavedra. New signals in pair production of heavy $Q=2/3$ singlets at LHC. *PoS*, TOP2006:003, 2006.
- [114] Roberto Contino and Geraldine Servant. Discovering the top partners at the LHC using same-sign dilepton final states. *JHEP*, 06:026, 2008.
- [115] J. A. Aguilar-Saavedra. Identifying top partners at LHC. *JHEP*, 11:030, 2009.
- [116] Shrihari Gopalakrishna, Tanumoy Mandal, Subhadip Mitra, and Rakesh Tibrewala. LHC Signatures of a Vector-like b' . *Phys. Rev.*, D84:055001, 2011.
- [117] Yasuhiro Okada and Luca Panizzi. LHC signatures of vector-like quarks. *Adv. High Energy Phys.*, 2013:364936, 2013.
- [118] Shrihari Gopalakrishna, Tanumoy Mandal, Subhadip Mitra, and Gregory Moreau. LHC Signatures of Warped-space Vectorlike Quarks. *JHEP*, 08:079, 2014.
- [119] F. Maltoni, Z. Sullivan, and S. Willenbrock. Higgs-boson production via bottom-quark fusion. *Phys. Rev.*, D67:093005, 2003.
- [120] Jonathan Kozaczuk and Travis A. W. Martin. Extending LHC Coverage to Light Pseudoscalar Mediators and Coy Dark Sectors. *JHEP*, 04:046, 2015.
- [121] W. Kilian, D. Rainwater, and J. Reuter. Pseudo-axions in little higgs models. *Phys. Rev. D*, 71:015008, Jan 2005.

- [122] Leonard Susskind. Dynamics of spontaneous symmetry breaking in the weinberg-salam theory. *Phys. Rev. D*, 20:2619–2625, Nov 1979.
- [123] E. Eichten, I. Hinchliffe, K. D. Lane, and C. Quigg. Signatures for technicolor. *Phys. Rev. D*, 34:1547–1566, Sep 1986.
- [124] Vernon Barger, Paul Langacker, Mathew McCaskey, Michael Ramsey-Musolf, and Gabe Shaughnessy. Complex singlet extension of the standard model. *Phys. Rev. D*, 79:015018, Jan 2009.
- [125] Serguei Chatrchyan et al. Search for a standard-model-like Higgs boson with a mass in the range 145 to 1000 GeV at the LHC. *Eur. Phys. J.*, C73:2469, 2013.
- [126] Observation and study of the Higgs boson candidate in the two photon decay channel with the ATLAS detector at the LHC. ATLAS-CONF-2012-168. 2012.
- [127] G. C. Branco, P. A. Parada, and M. N. Rebelo. A Common origin for all CP violations. CERN-TH-2003-153. 2003.
- [128] Sheldon L. Glashow and Steven Weinberg. Natural Conservation Laws for Neutral Currents. *Phys. Rev.*, D15:1958, 1977.
- [129] Measurements of the Higgs boson production and decay rates and constraints on its couplings from a combined ATLAS and CMS analysis of the LHC pp collision data at $\sqrt{s} = 7$ and 8 TeV. (ATLAS-CONF-2015-044), Sep 2015.
- [130] Jeremy Bernon, John F. Gunion, Howard E. Haber, Yun Jiang, and Sabine Kraml. Scrutinizing the alignment limit in two-Higgs-doublet models: $m_h = 125$ GeV. *Phys. Rev.*, D92(7):075004, 2015.
- [131] Stefan Liebler. Neutral Higgs production at proton colliders in the CP-conserving NMSSM. *Eur. Phys. J.*, C75(5):210, 2015.

- [132] E. Bagnaschi, R. V. Harlander, S. Liebler, H. Mantler, P. Slavich, and A. Vicini. Towards precise predictions for Higgs-boson production in the MSSM. *JHEP*, 06:167, 2014.
- [133] Abdelhak Djouadi. The Anatomy of electro-weak symmetry breaking. II. The Higgs bosons in the minimal supersymmetric model. *Phys. Rept.*, 459:1–241, 2008.
- [134] Search for heavy top-like quarks decaying to a Higgs boson and a top quark in the lepton plus jets final state in pp collisions at $\sqrt{s} = 8$ TeV with the ATLAS detector. (ATLAS-CONF-2013-018), Mar 2013.
- [135] Serguei Chatrchyan et al. Inclusive search for a vector-like T quark with charge $\frac{2}{3}$ in pp collisions at $\sqrt{s} = 8$ TeV. *Phys. Lett.*, B729:149–171, 2014.
- [136] The ATLAS collaboration. Search for production of vector-like top quark pairs and of four top quarks in the lepton-plus-jets final state in pp collisions at $\sqrt{s} = 13$ TeV with the ATLAS detector. ATLAS-CONF-2016-013. 2016.
- [137] Giacomo Cacciapaglia, Aldo Deandrea, Luca Panizzi, Naveen Gaur, Daisuke Harada, and Yasuhiro Okada. Heavy Vector-like Top Partners at the LHC and flavour constraints. *JHEP*, 03:070, 2012.
- [138] S. Dawson and E. Furlan. A Higgs Conundrum with Vector Fermions. *Phys. Rev.*, D86:015021, 2012.
- [139] S. Alekhin, A. Djouadi, and S. Moch. The top quark and Higgs boson masses and the stability of the electroweak vacuum. *Phys. Lett.*, B716:214–219, 2012.
- [140] K. A. Olive et al. Review of Particle Physics. *Chin. Phys.*, C38:090001, 2014.
- [141] The ATLAS collaboration. Search for scalar diphoton resonances with 15.4 fb^{-1} of data collected at $\sqrt{s}=13$ TeV in 2015 and 2016 with the ATLAS detector. ATLAS-CONF-2016-059. 2016.

- [142] Search for resonant production of high mass photon pairs using 12.9fb^{-1} of proton-proton collisions at $\sqrt{s} = 13\text{ TeV}$ and combined interpretation of searches at 8 and 13 TeV. (CMS-PAS-EXO-16-027), 2016.
- [143] Gerard Jungman, Marc Kamionkowski, and Kim Griest. Supersymmetric dark matter. *Phys. Rept.*, 267:195–373, 1996.
- [144] Mark Srednicki, Richard Watkins, and Keith A. Olive. Calculations of Relic Densities in the Early Universe. *Nucl. Phys.*, B310:693, 1988.
- [145] R. Adam et al. Planck 2015 results. I. Overview of products and scientific results. *Astron. Astrophys.*, 594:A1, 2016.
- [146] Mark W. Goodman and Edward Witten. Detectability of Certain Dark Matter Candidates. *Phys. Rev.*, D31:3059, 1985.
- [147] D. S. Akerib et al. Improved Limits on Scattering of Weakly Interacting Massive Particles from Reanalysis of 2013 LUX Data. *Phys. Rev. Lett.*, 116(16):161301, 2016.
- [148] Gianfranco Bertone, Dan Hooper, and Joseph Silk. Particle dark matter: Evidence, candidates and constraints. *Phys. Rept.*, 405:279–390, 2005.
- [149] Mikhail A. Shifman, A. I. Vainshtein, and Valentin I. Zakharov. Remarks on Higgs Boson Interactions with Nucleons. *Phys. Lett.*, B78:443–446, 1978.
- [150] John R. Ellis, Andrew Ferstl, and Keith A. Olive. Reevaluation of the elastic scattering of supersymmetric dark matter. *Phys. Lett.*, B481:304–314, 2000.
- [151] Yosef Nir and Dennis J. Silverman. Z Mediated Flavor Changing Neutral Currents and Their Implications for CP Asymmetries in B^0 Decays. *Phys. Rev.*, D42:1477–1484, 1990.
- [152] F. del Aguila, M. Perez-Victoria, and Jose Santiago. Observable contributions of new exotic quarks to quark mixing. *JHEP*, 09:011, 2000.

- [153] G. Barenboim, F. J. Botella, and O. Vives. Constraining models with vector - like fermions from FCNC in K and B physics. *Nucl. Phys.*, B613:285–305, 2001.
- [154] F. J. Botella, G. C. Branco, and M. Nebot. The Hunt for New Physics in the Flavour Sector with up vector-like quarks. *JHEP*, 12:040, 2012.
- [155] Francisco J. Botella, Miguel Nebot, and Gustavo C. Branco. Vector-like quarks and New Physics in the flavour sector. *J. Phys. Conf. Ser.*, 447:012061, 2013.
- [156] Ashutosh Kumar Alok, Subhashish Banerjee, Dinesh Kumar, and S. Uma Sankar. Flavor signatures of isosinglet vector-like down quark model. *Nucl. Phys.*, B906:321–341, 2016.
- [157] Koji Ishiwata, Zoltan Ligeti, and Mark B. Wise. New Vector-Like Fermions and Flavor Physics. *JHEP*, 10:027, 2015.